

In presenting the dissertation as a partial fulfillment of the requirements for an advanced degree from the Georgia Institute of Technology, I agree that the Library of the Institute shall make it available for inspection and circulation in accordance with its regulations governing materials of this type. I agree that permission to copy from, or to publish from, this dissertation may be granted by the professor under whose direction it was written, or, in his absence, by the Dean of the Graduate Division when such copying or publication is solely for scholarly purposes and does not involve potential financial gain. It is understood that any copying from, or publication of, this dissertation which involves potential financial gain will not be allowed without written permission.

3/17/65

b

THE EFFECT OF BOUNDARY-LAYER SEPARATIONS
ON LAMINAR HEAT TRANSFER

A THESIS

Presented to
The Faculty of the Graduate Division
by
Jerry Allen Sills

In Partial Fulfillment
of the Requirements for the Degree
Doctor of Philosophy in the School of Aerospace Engineering

Georgia Institute of Technology

February, 1967

THE EFFECT OF BOUNDARY-LAYER SEPARATIONS
ON LAMINAR HEAT TRANSFER

Approved:

Chairman

Date approved by Chairman 2/27/67

ACKNOWLEDGMENTS

The author wishes to express his gratitude to his thesis advisor, Mr. James E. Hubbartt, who suggested this problem. Mr. Hubbartt's interest, assistance, and encouragement are deeply appreciated. The author is also indebted to the members of his thesis reading committee, Dr. Arnold L. Ducoffe and Dr. Howard M. McMahon, for their many suggestions and their careful review of the work. Appreciation is also expressed to Dr. James C. Wu for his comments and suggestions during the research.

The author also acknowledges the many fruitful discussions with his friends. In particular, the assistance of Richard G. Bradley, Joseph D. Stewart, and Kenton D. Whitehead is gratefully appreciated. The author expresses his thanks to Mrs. Sue Bailey for her patience during the typing of the final draft of this thesis.

The financial assistance of the National Aeronautics and Space Administration during the author's graduate study is gratefully acknowledged.

The author owes a special debt of gratitude to his parents for their inspiration and encouragement throughout his academic endeavor.

Finally, the author expresses his gratitude to his wife for her patience, support, and encouragement during the research. Her many hours spent typing the rough draft of this thesis is deeply appreciated.

TABLE OF CONTENTS

	Page
ACKNOWLEDGMENTS	ii
LIST OF ILLUSTRATIONS	v
NOMENCLATURE	ix
SUMMARY	xiv
Chapter	
I. INTRODUCTION	1
II. THEORETICAL FORMULATION	11
The Physical Model	
Derivation of the Governing Equations	
Physical Coordinates	
Transformation to Incompressible Plane	
Transformation to Finite Interval	
The Solution in Physical Coordinates	
III. METHOD OF SOLUTION	33
The Finite-Difference Solution	
Derivation of the Difference Equations	
Solution for the Velocity Profiles	
Solution of the Energy Equation	
Stability of the Finite-Difference Solution	
Evaluation of the Heat Transfer	
Attached-Flow Regions	
Separated-Flow Regions	
Check of the Solution Method	
Application to the Present Study	
IV. RESULTS AND DISCUSSION	56
Heat Transfer Results from the Numerical Solution	
Heat Transfer Results Using the Correlation Technique	
Effects of Initial Attached-Flow Length	
Effect of Blunted-Cusp Reattachment Geometry	
V. CONCLUSIONS AND RECOMMENDATIONS	89

TABLE OF CONTENTS (Continued)

APPENDICES

A.	STABILITY ANALYSIS OF THE MOMENTUM EQUATION	93
B.	THE FINITE-DIFFERENCE SOLUTION OF THE LAMINAR, FLAT-PLATE BOUNDARY LAYER	98
C.	THE FINITE-DIFFERENCE SOLUTION OF THE LAMINAR, FREE SHEAR LAYER	109
	The Laminar Free Shear Layer with Finite Initial Thickness Numerical Study of the Similar Profiles of the Free Shear Layer	
D.	INVESTIGATION OF THE EFFECTS OF BLUNTNESS ON THE HEAT TRANSFER RATE	119
	The Range of Values for the Dividing Streamline Mach Number Application of Lees' Blunt Body Theory Effect of Degree of Bluntness	
	LITERATURE CITED	133
	VITA	135

LIST OF ILLUSTRATIONS

Figure	Page
1. The Physical Model Employed by Chapman	3
2. Illustration of Four Possible Reattachment Configurations	7
3. The Physical Model for the Present Study	12
4. Illustration of Coordinate Locations for the Equations of Motion	16
5. The Coordinate Transformation $\zeta = \tanh(\alpha Y)$ for Various Values of α	26
6. The Finite-Difference Lattice	35
7. Illustration of Alteration of Finite-Difference Mesh . .	52
8. The Physical Model for the Heat Transfer Study	53
9. Typical Local Heat Transfer Results from the Numerical Solution and Comparison with Equivalent Completely-Attached Flow ($L^* = 1$, $Pr = 0.72$)	57
10. Typical Local Heat Transfer Ratio Results from the Numerical Solution ($Pr = 0.72$)	58
11. Ratio of Local Heat Transfer Rates Downstream of Reattachment for $L^* = 0.1$	59
12. Ratio of Local Heat Transfer Rates Downstream of Reattachment for $L^* = 0.25$	60
13. Ratio of Local Heat Transfer Rates Downstream of Reattachment for $L^* = 0.5$	61
14. Ratio of Local Heat Transfer Rates Downstream of Reattachment for $L^* = 1$	62
15. Ratio of Local Heat Transfer Rates Downstream of Reattachment for $L^* = 2$	63
16. Comparison of the Correlation Curves for Different Values of L^*	65

LIST OF ILLUSTRATIONS (Continued)

Figure		Page
17.	Dividing Streamline Velocity Distribution for Three Multiple-Cavity Configurations	66
18.	Illustration of Comparison of Local Heat Transfer Rates for Free Shear Layers and Attached Boundary Layers ($L^* = 1$)	68
19.	Comparison of Local Heat Transfer Rates for Free Shear Layers and Attached Boundary Layers with the Same Initial Conditions from the Numerical Solution ($Pr = 0.72$)	69
20.	Comparison of Overall Heat Transfer Results from the Correlation Technique with Results from the Numerical Solution for $L^* = 1$ ($Pr = 0.72$)	74
21.	Ratio of Overall Heat Transfer Rates from the Correlation Technique for $L^* = 0.1$ ($Pr = 0.72$)	76
22.	Ratio of Overall Heat Transfer Rates from the Correlation Technique for $L^* = 0.25$ ($Pr = 0.72$)	77
23.	Ratio of Overall Heat Transfer Rates from the Correlation Technique for $L^* = 0.5$ ($Pr = 0.72$)	78
24.	Ratio of Overall Heat Transfer Rates from the Correlation Technique for $L^* = 1$ ($Pr = 0.72$)	79
25.	The Effect of Number of Cavities and Cavity Spacing on the Overall Heat Transfer Using the Correlation Technique ($Pr = 0.72$)	81
26.	Illustration of the Two Cases Considered for the Initial Attached-Flow Length	83
27.	Comparison of Overall Heat Transfer Rates for Two Initial Attached-Flow Lengths ($Pr = 0.72$)	85
28.	Comparison of Experimental Local Heat Transfer Rates from Reference (9) with the Correlation Curve of the Present Analysis ($L^* = 2$)	88
29.	Illustration of the Effect of the Transformation Constant α on the Values of Y Corresponding to the Grid Points in the Finite-Difference Mesh	101

LIST OF ILLUSTRATIONS (Continued)

Figure	Page
30. Comparison of the Flat-Plate Velocity Profile from the Numerical Solution with the Blasius Similar Profile	102
31. Comparison of the Wall Shear Computed Using Linear and Parabolic Curve Fits with Blasius Value	104
32. Comparison of the Enthalpy Function Profiles for the Flat Plate from the Finite-Difference Solution with the Similar Profiles of Reference (25)	105
33. Comparison of Local Heat Transfer Rates Computed Using Linear and Parabolic Curve Fits with Similarity Solution	106
34. Overall Heat Transfer Rate to a Flat Plate from the Finite-Difference Solution and Comparison with the Asymptotic Solution ($Pr = 0.72$)	108
35. Dividing Streamline Velocity Distribution from the Finite-Difference Solution with Initial Blasius Profile and Comparison with Reference (6).	111
36. Development of Velocity Profile for the Free Shear Layer from the Finite-Difference Solution with Flat-Plate Profile at Separation	112
37. Development of Enthalpy Function Profile H_1 for the Free Shear Layer from the Finite-Difference Solution with Flat-Plate Profile at Separation, $Pr = 0.72$. . .	113
38. Development of Enthalpy Function Profile H_2 for the Free Shear Layer from the Finite-Difference Solution with Flat-Plate Profile at Separation, $Pr = 0.72$. . .	114
39. Velocity Profile from the Finite-Difference Solution with Chapman Profile Used as Initial Profile, $Pr = 0.72$	116
40. Enthalpy Function Profile H_1 from the Finite-Difference Solution with Chapman Profile Used as Initial Profile, $Pr = 0.72$	117
41. Enthalpy Function Profile H_2 from the Finite-Difference Solution with Chapman Profile Used as Initial Profile, $Pr = 0.72$	118

LIST OF ILLUSTRATIONS (Continued)

Figure	Page
42. Variation of the Mach Number Along the Dividing Streamline with the Freestream Mach Number ($Pr = 1$) . .	122
43. Geometry for the Blunted Leading Edge	123
44. Illustration of Geometries Employed to Investigate Effect of Degree of Bluntness on the Overall Heat Transfer Rate	128
45. Effect of Thickness ratio d/L on the Heat Transfer Rate for Several Values of \bar{q}_{nose}	132

NOMENCLATURE

Roman Symbols

- A - coefficient in stability analysis of momentum equation.
- $\left. \begin{matrix} A_1(i,j) \\ A_2(i,j) \\ A_3(i,j) \end{matrix} \right\}$ - coefficients in the momentum difference equation.
- B - coefficient in stability analysis of momentum equation.
- $B(i,j)$ - inhomogeneous term in the momentum difference equation.
- C - constant in Chapman-Rubesin viscosity-temperature relation.
- $\left. \begin{matrix} C_1(i,j) \\ C_2(i,j) \\ C_3(i,j) \end{matrix} \right\}$ - coefficients in the energy difference equations.
- C_p - specific heat at constant pressure.
- D - cavity depth.
- d - thickness of blunt flat plate.
- $\left. \begin{matrix} D_1(i,j) \\ D_2(i,j) \end{matrix} \right\}$ - inhomogeneous terms in the energy difference equations.
- g - any of the dependent variables whose derivatives appear in the momentum or energy equations.
- H - new dependent variable defined by equation (15).
- h - static enthalpy.
- H_1, H_2 - enthalpy functions which are combined to yield the static enthalpy.
- \hat{i} - the imaginary unit, $(\hat{i})^2 = -1$.
- k - coefficient of thermal conductivity.
- L - cavity length and reference length.

NOMENCLATURE (Continued)

L_a	- length of attached-flow regions between cavities.
L_b	- surface length of blunt flat plate.
L_{eq}	- length of equivalent flat plate with the same overall heat transfer rate as a blunt flat plate.
L_s	- length of initial attached-flow region.
L^*	- ratio of cavity spacing to cavity length, L_a/L .
M	- Mach number.
N	- the number of lattice points in the normal coordinate is $N + 1$.
p	- static pressure.
p_o'	- stagnation pressure behind the bow shock wave at the stagnation point.
Pr	- the Prandtl number, $C_p \mu / k$.
q	- local heat transfer rate.
\bar{q}	- overall heat transfer rate.
q^*	- ratio of local heat transfer rate to that for a completely-attached flow.
\bar{q}^*	- ratio of overall heat transfer rate to that for a completely-attached flow.
\bar{q}_{nose}	- ratio of overall heat transfer rate to the nose of a blunt flat plate to that for a sharp-edged flat plate of the same surface length.
Q	- total heat transfer.
r	- radius of curvature for nose of blunt flat plate.
R	- gas constant.
Re	- Reynolds number based on L and freestream properties, $Re = \rho_e u_e L / \mu_e$.
S	- nondimensional streamwise coordinate, $S = x/L$.

NOMENCLATURE (Continued)

\bar{S}	- nondimensional distance downstream of the initial attached-flow region.
\tilde{S}	- nondimensional distance downstream of reattachment.
S^*	- nondimensional distance parameter for the non-similar free shear layer.
T	- static temperature.
T_o	- stagnation temperature.
u	- streamwise velocity component.
v	- normal velocity component.
\tilde{v}	- velocity parameter given by $\tilde{v} = \frac{\rho}{\rho_e} \sqrt{\frac{Re}{C}} v + \frac{\partial Y}{\partial x} Lu$.
x	- distance along the surface or the dividing streamline.
X_{eq}	- length of sharp-edged flat plate with the same overall heat transfer rate as the nose of the blunt flat plate.
y	- normal distance from the surface or the dividing streamline.
Y	- transformed normal coordinate defined by equation (8).

Greek Symbols

α	- constant in coordinate transformation defined by equation (24).
β	- constant employed in correlation technique.
γ	- ratio of specific heats.
$\Delta\zeta, \Delta S$	- increment in the normal and streamwise coordinate, respectively.
ϵ	- the truncation error in the numerical solution.
ζ	- the transformed normal coordinate defined by equation (24).
η	- the Blasius similarity parameter.
θ	- constant in viscosity relation dependent on the gas.

NOMENCLATURE (Continued)

- λ - function of wall and freestream conditions used in the combination of enthalpy functions H_1 and H_2 .
- μ - coefficient of viscosity.
- ξ - exponent used in Fourier decomposition of error.
- ρ - density.
- ϕ - error growth in the stability analysis.
- ψ - the stream function.
- ω - defined by $\omega = \frac{\mu}{RT}$
- Ω - closed surface for the energy balance.

Superscripts

- *
 - '
 -
- refers to dimensionless variables.
 - indicates value for new finite-difference grid.
 - denotes mean value.

Subscripts

- a
 - att
 - av
 - aw
 - b
 - bl
 - cor
 - d
- indicates active degrees of freedom of molecule (translation and rotation).
 - denotes value for an attached-flow region.
 - refers to average value.
 - indicates adiabatic wall conditions.
 - refers to blunt flat plate.
 - refers to completely-attached flow.
 - denotes value from correlation curve.
 - denotes value at the dividing streamline.

NOMENCLATURE (Continued)

- e - refers to conditions at the outer edge of the viscous layer.
- fp - denotes value for a sharp-edged flat plate.
- i - step index in the streamwise coordinate.
- int - refers to contribution due to vibration and electronic excitation.
- j - step index in the normal coordinate.
- sep - denotes value for a separated-flow region.
- w - indicates wall conditions.
- δ - indicates conditions at the edge of the boundary layer.
- o - indicates stagnation conditions or initial conditions.

SUMMARY

The possibility of reducing the overall heat transfer rate to a surface by exploiting the reduction in heat transfer rates in regions of separated laminar flow is studied. A flat plate with a series of cavities located in the surface is considered.

An implicit finite-difference method for solving the boundary-layer equations for laminar, compressible flow is developed. This method describes the non-similar development of an arbitrary initial profile for either an attached boundary layer or a free shear layer. The compressible boundary-layer equations for a constant-pressure flow field are written in an equivalent incompressible form by introducing a coordinate transformation similar to that of Howarth and employing the Chapman-Rubesin viscosity-temperature relation. The implicit finite-difference method employed in this study requires a finite range for the normal coordinate. This condition is satisfied by a new transformation of the normal coordinate. This method yields results which compare well for problems whose solutions are available in the literature.

The finite-difference method is applied to the evaluation of the local heat transfer rate to a flat plate with a series of cavities located in the surface. A sharp-cusp reattachment geometry is assumed, and various cavity spacings are considered. Local heat transfer rates for the separated-flow regions are calculated along the dividing streamline. The local heat transfer rates exhibit the following two characteristics:

1. For a multiple-cavity configuration with a given ratio of cavity length to attached-flow length between cavities, the local heat transfer rates for the attached-flow regions downstream of each cavity correlate with those for a completely-attached flow. The correlation curves vary with cavity spacing, with the smaller cavity spacings resulting in higher local heat transfer rates.

2. For a Prandtl number of 0.72, the local heat transfer rate for a free shear layer is essentially 56 per cent of that for an attached boundary layer for the same initial profiles. Thus the average heat transfer rate across a free shear layer is 56 per cent of that to an equivalent attached flow not only for the case of zero initial thickness (as determined by Chapman) but for the case of a finite initial thickness as well.

These two characteristics of the local heat transfer rates are used to develop an approximate method for evaluating the heat transfer to a multiple-cavity configuration. This approximate method provides overall heat transfer rates for multiple-cavity configurations in good agreement with the results from the finite-difference method while requiring much less computational effort. The results from the approximate method are slightly conservative, and the agreement improves as the number of cavities increases.

Based on results obtained using the approximate method, the effect of multiple cavities is to reduce the overall heat transfer rate in comparison with a configuration with fewer cavities. For example, a two-cavity configuration can reduce the overall heat transfer rate by as much as 19 per cent more than a one-cavity configuration of the same

length. The reduction due to multiple cavities increases as the cavity spacing decreases. For a multiple-cavity configuration, the maximum reduction in overall heat transfer rate occurs when the cavities are as long as practicable and the cavity spacing is as small as possible consistent with the condition that the length of the attached-flow region following the final cavity be as short as possible.

The effect of a blunt-cusp reattachment geometry on the heat transfer rate is explored using blunt body theory and assuming that the flow approaching reattachment may be considered uniform. Sample calculations demonstrate that, for values of the Mach number of interest for reattaching free shear layers, blunting increases the overall heat transfer rate in comparison with a sharp-edged geometry. This increase is small, however, for moderate bluntness ratios.

CHAPTER I

INTRODUCTION

Boundary-layer separation is a viscous-flow phenomenon which occurs in a number of supersonic flow problems including base and wake flows, shock-boundary layer interactions, flow over cavities and steps, flow over deflected control surfaces, and flow past spiked bodies. The importance of separation effects on the various aerodynamic parameters has resulted in many theoretical and experimental investigations of separated flows. In particular, much interest has been focused on the comparison of heating rates in separated-flow regions to those of attached flows for the laminar flow regime.

Reviews of separated-flow phenomena have been presented by Kaufman, et al. (1), Nash (2), and Lykoudis (3). Only the previous research related to the laminar, cavity-induced separations of concern for the present investigation will be considered herein.

For a number of years the very low transition Reynolds number for laminar free shear layers in subsonic flow resulted in the treatment of such flows as laboratory phenomena of little practical interest. Chapman, Kuehn, and Larson (4) determined experimentally that the transition Reynolds number for the laminar free shear layer increases greatly with increasing supersonic Mach number, and that in hypersonic flow the laminar free shear layer can be almost as stable as an attached laminar boundary layer. This result stimulated interest in laminar separation problems for

hypersonic flow. Unfortunately, even for the laminar regime the complex nature of the recirculating flow in the separated region and the flow in the neighborhood of reattachment makes complete analysis of separated flows extremely difficult.

In a theoretical analysis of heat transfer in separated-flow regions Chapman (5) introduced the concept of the dividing streamline which allowed the evaluation of the heat transfer to a region of separated flow without considering in detail the recirculating flow. The physical model employed by Chapman is illustrated in Figure 1. The separated region, or cavity, is treated as an isothermal, dead-air sink to which energy is transferred through the shear layer or mixing zone between the external stream and the essentially stagnant fluid in the cavity. Chapman's analysis of the free shear layer involved the following assumptions:

1. The thickness of the boundary layer is zero at separation.
2. The length of the reattachment zone is small compared with the length of the separated region.
3. The pressure is constant along the free shear layer.
4. The wall (i.e., the cavity floor) is isothermal.
5. The low-speed air in the reverse-flow region is at wall temperature when drawn into the free shear layer.

Assuming a uniform velocity profile at separation, Chapman obtained a similar solution to the equations of motion for the laminar, compressible, free shear layer. An energy balance for the system bounded by the cavity walls and the dividing streamline provides an expression for the total energy transfer to the separated region in terms of the conditions in the free shear layer along the dividing streamline. The analysis indicated that

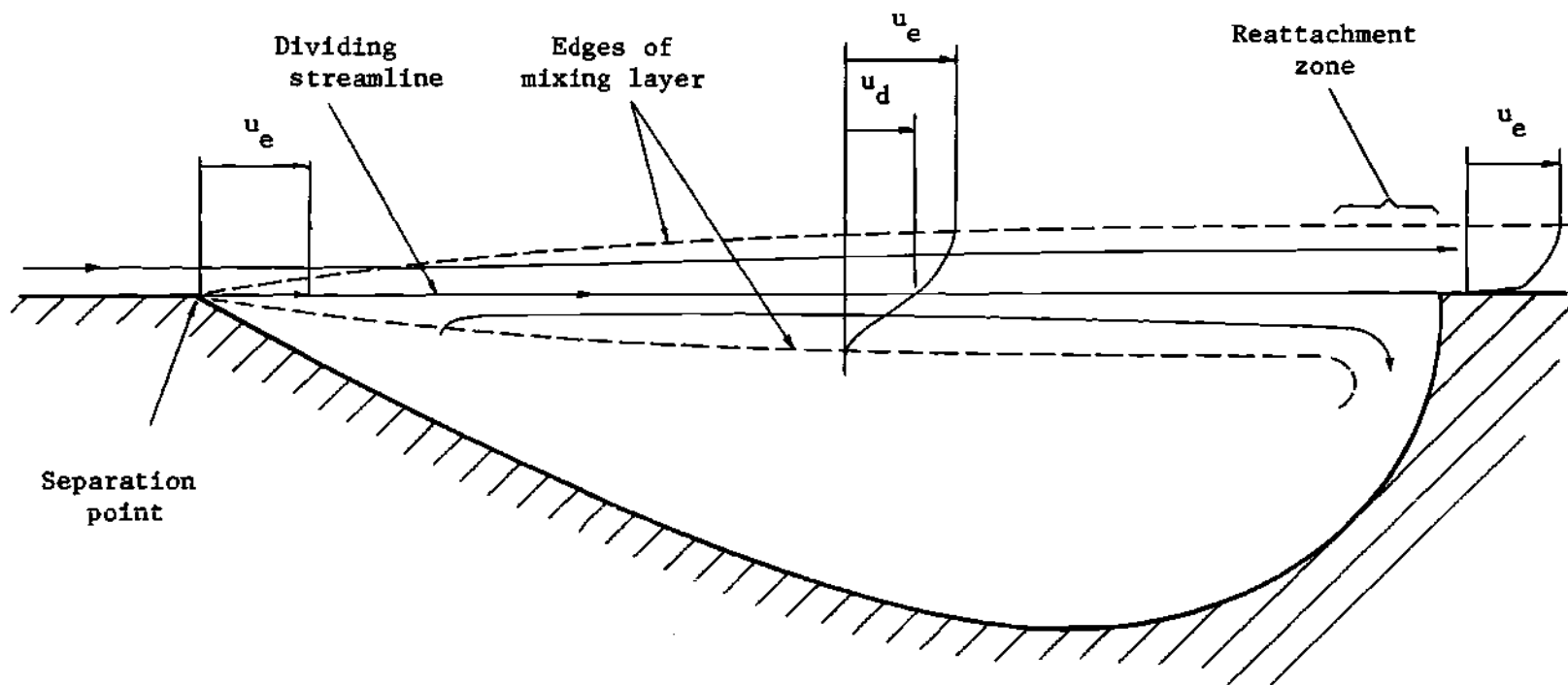


Figure 1. The Physical Model Employed by Chapman.

for air ($Pr = 0.72$) the average heat transfer rate in a region of laminar separated flow was approximately 56 per cent of that which would occur with a corresponding attached laminar boundary layer.

In studying the laminar base-flow region, Denison and Baum (6) extended the Chapman solution of the compressible, laminar free shear layer to include the effects of a finite boundary-layer profile at separation. Their finite-difference solution using the Crocco coordinate system demonstrated the conversion of the initial profile to the asymptotic similar shear-layer profile of Chapman. Denison and Baum concluded that Chapman's similar profile could not be justified, in general, since for practical separated flows with initial boundary layers the free shear layer is far too short for Chapman's similar solution to be valid.

The first experimental investigation based on the Chapman model was that of Larson (7). He measured the heat transfer to rectangular cavities in both two- and three-dimensional bodies and compared the results with measurements on equivalent attached-flow bodies. From his measurements he concluded that for laminar flow Chapman's theory yielded accurate values for the average heat transfer rate to the separated region. Larson did not investigate the heat transfer rates downstream of reattachment, although he noted that the maximum local heat transfer rates along the cavity floor occurred in this region.

Another experimental investigation which was concerned, in part, with the heat transfer characteristics of cavity-separated regions on the surface of cones was reported by Bogdonoff and Vas (8). Local heat transfer rates and pressure distributions were measured along the cavity floor and the region downstream of reattachment. The cavity depth was chosen to

guarantee that the free shear layer did not reattach to the cavity floor, but bridged the cavity. The pressures in the cavity were found to be essentially constant for thin boundary layers at separation. The heat transfer rate in the cavity region was found to give a reasonable check of the Chapman prediction. However, the authors concluded that the overall heat transfer to the cone-cavity model would not differ significantly from that of the basic cone with no cavity due to the increased heat transfer rates over the surface downstream of the cavity.

A third experimental investigation of laminar separated flows is that of Nicoll (9). His investigation dealt exclusively with cavity-induced separated flows and was a detailed extension of the work of Bogdonoff and Vas. The separated regions studied were annular cavities on 20° cones. Pressure distributions and local heat transfer rates over the floor of the cavity and over the region downstream of the cavity were measured for the following Mach numbers and Reynolds numbers based on conditions at the edge of the boundary layer:

Mach number	Reynolds number per inch
6.46	5.9×10^5
6.54	9.73×10^5
6.61	13.38×10^5

The cavity flows were found to be divided into three types: deep "open" flows, shallow "open" flows, and "closed" flows. "Open" flows are those in which the dividing streamline bridges the cavity, while for "closed" flows the free shear layer reattaches to the cavity floor. For deep open flows the pressure is constant over most of the cavity floor, while for shallow open flows a pressure gradient exists along the floor of

the cavity. Nicoll concluded that the deep open cavity flows with constant floor pressure over 90 per cent of the cavity span (which closely approximate the Chapman model) existed for cavity length-to-depth ratios (L/D) less than about seven. For L/D ratios between seven and twenty the flows were of the shallow open type, and for an L/D ratio somewhere between twenty and forty the transition from open to closed type cavity flows occurred.

Nicoll's heat transfer rate measurements for the deep open cavities showed that the lowest local heat transfer rates occurred on the upstream portion of the cavity floor, reaching a minimum of 10 to 20 per cent of the attached-flow value, while the highest local heating rates occurred in the vicinity of reattachment. Integration of the heat transfer rates over the floor of the cavity yielded average heat transfer rates in agreement with Chapman's theory. An integration of the heat transfer rates over the cavity floor and for one cavity-length downstream of reattachment indicated that the overall heat transfer rate was reduced about 10 per cent. Thus most of the reduction in heat transfer rate afforded by the separated-flow region was effectively countered by the increased heat transfer rates over the surface downstream of reattachment.

The reattachment geometry may be the most important single factor affecting the heating rates using cavity-separated flows. Some of the reattachment configurations which may be envisioned are depicted in Figure 2. The difficulty of analyzing the reattachment region is evidenced by the fact that only one method has been published to date for calculating heating rates at reattachment. Chung and Viegas (10) analyzed the inviscid, incompressible, rotational flow in a cavity with a shoulder reattachment



(a) Shoulder Reattachment Geometry.



(b) Ramp Reattachment Geometry.



(c) Sharp-Cusp Reattachment Geometry.



(d) Blunted-Cusp Reattachment Geometry.

Figure 2. Illustration of Four Possible Reattachment Configurations.

geometry (Figure 2(a)). Nicoll's experiments, which employed a shoulder reattachment geometry, indicated that the theory of Chung and Viegas overestimated the average heat transfer rate at reattachment by a factor of two.

Holden (11) recently investigated two-dimensional separated flows with a ramp reattachment geometry similar to that illustrated in Figure 2(b). His experiments showed that the maximum heat transfer rate near reattachment is strongly dependent on the reattachment angle. This indicates that a properly designed "glancing" reattachment may offer reduced heating rates as compared with a shoulder reattachment.

The two additional reattachment geometries illustrated in Figures 2(c) and 2(d) utilize a cusp reattachment geometry. With the sharp-cusp reattachment of Figure 2(c), the flow below the dividing streamline is smoothly scooped off at reattachment. The shear flow above the dividing streamline can then be analyzed downstream of reattachment using constant-pressure boundary-layer theory. For the more practical blunted-cusp geometry of Figure 2(d) the influence of the reattachment geometry extends over a small but finite portion of the free shear layer profile. In this case, the flow approaching reattachment may be considered uniform and the reattachment flow may be approximated using blunt body theory. These two types of reattachment are considered in the present investigation.

In summary, the reduction in heat transfer in regions of separated flow offers a method of reducing the local heat transfer rates to hypersonic vehicles. However, the open-type cavity flows which correspond to the Chapman model and which result in large reductions in the heat transfer rates occur for only a restricted range in the cavity length-to-depth

ratio (L/D). Furthermore, an attendant increase in the local heat transfer rates occurs in the region following reattachment. However, it appears that the overall heat transfer rate to a surface with a cavity may be reduced. The total reduction depends upon the magnitudes of the heat transfer rates at reattachment and the length of the surface following reattachment. If cavity depth were of no concern, the optimum heat transfer rate reduction would occur for the configuration of a single cavity spanning the region of interest. Unfortunately, the maximum cavity depth may be dictated by some physical restriction on the geometry. For example, skin thickness or structural integrity might dictate a certain maximum cavity depth. Coupled with the restriction on L/D , this determines a maximum cavity length which may be shorter than the region of interest. With this restriction in mind, one approach might be to place a series of cavities in the surface. The advantage of this approach depends upon the magnitude of the elevated heat transfer rates over the attached-flow regions between the cavities as well as the effectiveness of succeeding cavities in reducing the local heat transfer rates.

The purpose of this study is to investigate analytically the possibility of reducing the overall heat transfer rate to a surface by exploiting the reduction in heat transfer rates in regions of cavity-induced separated flow. The effect of the elevated heating rates over the surface following reattachment is studied for the cusp reattachment geometry. A numerical method for evaluating the heat transfer rates in both separated and attached flows with non-similar velocity and temperature profiles is first developed. This method is then used to investigate the possibility of reducing the overall heat transfer rate to a surface by

employing a series of cavities. The effects of the number of cavities and the spacing between cavities are both considered.

CHAPTER II

THEORETICAL FORMULATION

The complex nature of the recirculating flow in cavity-type separated flows makes the analysis of these flow fields extremely difficult. The formidable problems associated with analyzing the entire separated flow field have led to the introduction of a number of simplifying assumptions. In the following paragraphs the physical model employed in the present analysis is presented, the assumptions inherent in the model are described, and the resulting limitations discussed. The governing equations are then derived in a form convenient for the numerical solution described in Chapter III.

The Physical Model

The physical model for this study consists of a number of cavities located on the surface of a flat plate and is depicted schematically in Figure 3. The cavities are assumed to be sufficiently deep to lie in the deep, open range described by Nicoll. The assumptions made here concerning the separated-flow regions closely parallel those used by Chapman in that the cavity is treated as an essentially stagnant region to which energy is transferred through the thin viscous layer separating the external flow and the fluid in the separated region. Specifically, the assumptions of the present analysis are as follows:

1. The pressure is constant along both the attached boundary layers and free shear layers.

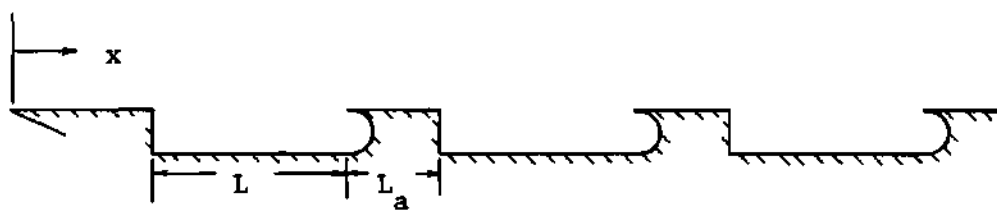


Figure 3. The Physical Model for the Present Study.

2. The surface of the attached-flow regions and the floor of the cavities are at the same constant temperature.
3. The low-speed flow in the cavity separation regions is at wall temperature when drawn into the free shear layer.
4. The dividing streamline reattaches tangent to the cusped rear lip of each cavity with no rise in pressure.
5. The Prandtl number Pr is constant (but not necessarily 1.0).
6. The variation of viscosity with temperature may be described by

$$\frac{\mu}{\mu_e} = C \frac{T}{T_e}$$

7. The gas obeys the equation of state for a thermally perfect gas, i.e.,

$$p = \rho RT$$

Assumption 1 is the same as made by Chapman and verified by the experiments of Nicoll for cavities in the deep, open regime. As a consequence of this assumption, the dividing streamline is a straight line from separation to reattachment. Assumption 2 is commonly used in attached boundary-layer flows, and its use for the cavity floors is equally applicable. Assumption 3 implies that the high-energy fluid from the shear layer which is turned into the cavity is accommodated to the wall temperature before being entrained into the shear layer. Assumption 4 eliminates the influence of reattachment geometry on the flow ahead of reattachment. This simplification permits the flow downstream of reattachment to be

analyzed by the system of parabolic equations used for constant-pressure boundary layers. Assumption 5 is commonly used for gases since the variation of Prandtl number is very small over a wide range of temperatures. The viscosity-temperature relation of assumption 6 is a good approximation over moderate ranges of temperatures and leads to an important simplification of the solution of the equations of motion (2). Assumption 7 is commonly used and is very accurate for gases over a wide range of temperatures.

The present investigation is concerned with a comparison of the heat transfer rates to surfaces with and without cavities and not with absolute heat transfer rates. In making these comparisons, the effects of the assumptions concerning the gas properties tend to compensate.

Derivation of the Governing Equations

For laminar flow over a constant-pressure, attached-flow region and for the constant-pressure, laminar free shear layer, assuming that the layer affected by viscosity is thin, an estimation of the order of magnitude of the various terms in the complete Navier-Stokes equations for viscous, compressible flow leads to the familiar Prandtl boundary-layer equations. The equations of continuity, momentum, and energy are first written in terms of physical coordinates. Next a transformation similar to that of Howarth is employed to express the equations in an equivalent incompressible form. The normal coordinate, which has an infinite range, is then transformed to a finite range to permit the use of the implicit finite-difference solution method described in a later chapter. Finally, the transformation back to physical coordinates is discussed.

Physical Coordinates

For the steady, compressible, laminar flow of a thermally perfect gas, using x as the distance along the surface or the dividing streamline and y as the normal distance from the surface or the dividing streamline as depicted in Figure 4, the boundary-layer equations may be written as follows:

Momentum equation:

$$\rho u \frac{\partial u}{\partial x} + \rho v \frac{\partial u}{\partial y} = \frac{\partial}{\partial y} \left(\mu \frac{\partial u}{\partial y} \right) \quad (1)$$

Energy equation:

$$\rho u \frac{\partial h}{\partial x} + \rho v \frac{\partial h}{\partial y} = \frac{1}{Pr} \frac{\partial}{\partial y} \left(\mu \frac{\partial h}{\partial y} \right) + \mu \left(\frac{\partial u}{\partial y} \right)^2 \quad (2)$$

Continuity equation:

$$\frac{\partial(\rho u)}{\partial x} + \frac{\partial(\rho v)}{\partial y} = 0 \quad (3)$$

For a thermally perfect gas the equation of state for a region of constant pressure is

$$\frac{T}{T_r} = \frac{\rho_r}{\rho} \quad (4)$$

where the subscript r indicates some reference value.

Within the assumptions of this analysis equations (1) through (4) apply to both the attached boundary layer and the free shear layer. The mathematical description of the two types of flow differs only in the

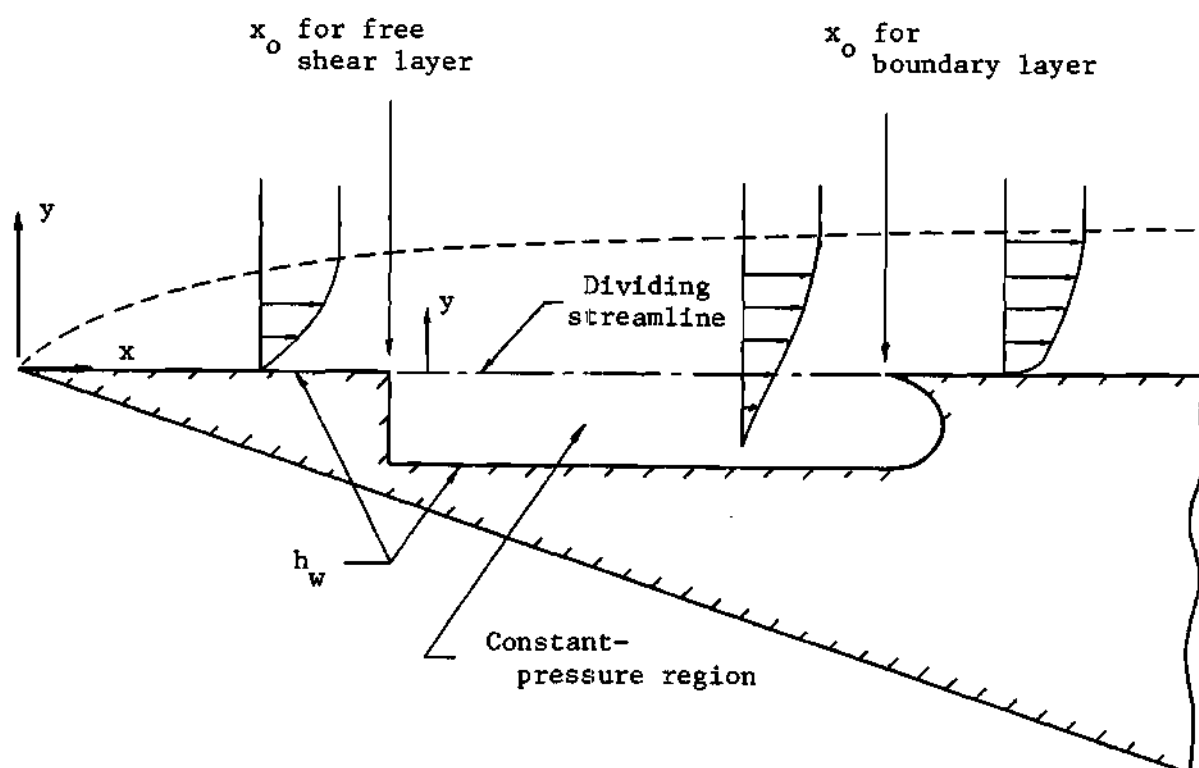


Figure 4. Illustration of Coordinate Locations for the Equations of Motion.

specification of the boundary conditions.

For the attached boundary layers the boundary conditions are

$$\left. \begin{aligned} u = v = 0 \quad , \quad h = h_w \quad \text{at} \quad y = 0 \\ \\ u = u_e \quad , \quad h = h_e \quad \text{at} \quad y = \infty \end{aligned} \right\} \quad (5)$$

where the wall enthalpy h_w is assumed constant and the subscript e indicates the value at the outer edge of the viscous layer.

The boundary conditions for the free shear layer are

$$\left. \begin{aligned} u = 0 \quad , \quad h = h_w \quad \text{at} \quad y = -\infty \\ \\ v = 0 \quad \quad \quad \text{at} \quad y = 0 \\ \\ u = u_e \quad , \quad h = h_e \quad \text{at} \quad y = \infty \end{aligned} \right\} \quad (6)$$

In addition to these boundary conditions, the velocity and enthalpy profiles must be known at some initial station $x = x_0$ due to the parabolic nature of the boundary-layer equations. Thus

$$\left. \begin{aligned} u(x,y) = u_0(y) \\ \\ v(x,y) = v_0(y) \\ \\ h(x,y) = h_0(y) \end{aligned} \right\} \quad \text{at} \quad x = x_0 \quad (7)$$

Transformation to Incompressible Plane

Since the viscosity μ and the density ρ are functions of temperature, the continuity, momentum, and energy equations are coupled and must

be solved simultaneously in this form. This difficulty may be circumvented by introducing a transformation of the coordinates similar to that of Howarth. The transformation used here is from (x,y) coordinates to (S,Y) coordinates where S and Y are defined by

$$\left. \begin{aligned} Y &= \frac{\sqrt{\text{Re}/C}}{L} \int_0^y \frac{\rho}{\rho_e} dy \\ S &= \frac{x}{L} \end{aligned} \right\} \quad (8)$$

where L is some reference length, Re is the Reynolds number based on L and freestream properties

$$\text{Re} = \frac{\rho_e u_e L}{\mu_e}$$

and C is the constant in the Chapman-Rubesin viscosity-temperature relation

$$\frac{\mu}{\mu_e} = C \frac{T}{T_e}$$

The constant C is computed by matching the Chapman-Rubesin relation above and the more accurate Sutherland relation given by

$$\frac{\mu}{\mu_e} = \sqrt{\frac{T}{T_e}} \frac{1 + \theta}{1 + \theta T_e/T}$$

at some reference temperature T_r . This results in the relation

$$C = \frac{\mu_r}{\mu_e} \frac{T_e}{T_r} = \sqrt{\frac{T_e}{T_r}} \frac{1 + \theta}{1 + \theta T_e/T_r} \quad (9)$$

where θ is an empirical constant equal to 0.505 for air.

The transformation from (x,y) coordinates to (S,Y) coordinates is accomplished by employing the transformation relations

$$\frac{\partial}{\partial x} = \frac{1}{L} \frac{\partial}{\partial S} + \frac{\partial Y}{\partial x} \frac{\partial}{\partial Y}$$

$$\frac{\partial}{\partial y} = \frac{\rho}{L\rho_e} \sqrt{\frac{Re}{C}} \frac{\partial}{\partial Y}$$

and defining a stream function ψ by

$$\left. \begin{aligned} \rho u &= \rho_e \frac{\partial \psi}{\partial y} \\ \rho v &= -\rho_e \frac{\partial \psi}{\partial x} \end{aligned} \right\} \quad (10)$$

Applying the transformation relations to the definition of the stream function yields

$$\frac{\partial \psi}{\partial Y} = L \sqrt{\frac{C}{Re}} u \quad ; \quad -\frac{\partial \psi}{\partial S} = L \sqrt{\frac{C}{Re}} \hat{v} \quad (11)$$

where

$$\hat{v} = \frac{\rho}{\rho_e} \sqrt{\frac{Re}{C}} v + L \frac{\partial Y}{\partial x} u$$

Upon application of the transformation relations and using equation (10) the momentum equation in (S,Y) coordinates becomes

$$u^* \frac{\partial u^*}{\partial S} + v^* \frac{\partial u^*}{\partial Y} = \frac{\partial^2 u^*}{\partial Y^2} \quad (12)$$

where

$$u^* = \frac{u}{u_e}, \quad v^* = \frac{\tilde{v}}{u_e}$$

Similarly the energy equation in (S,Y) coordinates becomes

$$u^* \frac{\partial h^*}{\partial S} + v^* \frac{\partial h^*}{\partial Y} = \frac{1}{Pr} \frac{\partial^2 h^*}{\partial Y^2} + \frac{u_e^2}{h_e} \left(\frac{\partial u^*}{\partial Y} \right)^2 \quad (13)$$

where

$$h^* = \frac{h}{h_e}$$

The continuity equation becomes

$$\frac{\partial u^*}{\partial S} + \frac{\partial v^*}{\partial Y} = 0 \quad (14)$$

Equations (12), (13), and (14) are in incompressible form in that the energy equation has been uncoupled from the continuity and momentum equations, thus permitting solution for the velocity profiles in (S,Y) coordinates independent of the energy equation.

With velocity profiles provided by the solution of the momentum and continuity equations, the energy equation is a linear, second-order, partial differential equation. To reduce the number of computations required later, the energy equation (13) may be separated into two equations

whose solutions may be obtained independent of u_e , h_e , and h_w . These solutions may then be superimposed to obtain the enthalpy profile for a number of values of u_e , h_e , and h_w . Introduce a new dependent variable H defined by

$$H = \frac{h^* - 1}{u_e^2/h_e} \quad (15)$$

Introduction of H into equation (13) yields

$$u^* \frac{\partial H}{\partial S} + v^* \frac{\partial H}{\partial Y} = \frac{1}{Pr} \frac{\partial^2 H}{\partial Y^2} + \left(\frac{\partial u^*}{\partial Y} \right)^2 \quad (16)$$

The boundary conditions for equations (12), (14), and (16) corresponding to equations (5) and (6) are as follows:

Attached boundary layers:

$$\left. \begin{aligned} u^* = v^* = 0, \quad H = \frac{h_w^* - 1}{u_e^2/h_e} \quad \text{at } Y = 0 \\ u^* = 1, \quad H = 0 \quad \text{at } Y = \infty \end{aligned} \right\} \quad (17)$$

Free shear layers:

$$\left. \begin{aligned} u^* = 0, \quad H = \frac{h_w^* - 1}{u_e^2/h_e} \quad \text{at } Y = -\infty \\ v^* = 0 \quad \text{at } Y = 0 \\ u^* = 1, \quad H = 0 \quad \text{at } Y = \infty \end{aligned} \right\} \quad (18)$$

The initial conditions corresponding to equation (7) may be expressed as

$$\left. \begin{aligned} u^*(S,Y) &= u_o^*(Y) \\ v^*(S,Y) &= v_o^*(Y) \\ H(S,Y) &= H_o(Y) \end{aligned} \right\} \quad \text{at } S = S_o \quad (19)$$

As formulated in terms of H , the energy equation (16) is explicitly independent of u_e , h_e , and h_w , which appear only in the boundary conditions equations (17) and (18). It is now convenient to decompose equation (16) into two equations, each satisfying boundary conditions independent of u_e , h_e , and h_w . Since equation (16) is linear in H , the solutions of these two equations may be superimposed to satisfy the boundary conditions given by equations (17) and (18).

Let H_1 be the solution of the equation

$$u^* \frac{\partial H_1}{\partial S} + v^* \frac{\partial H_1}{\partial Y} = \frac{1}{Pr} \frac{\partial^2 H_1}{\partial Y^2} + \left(\frac{\partial u^*}{\partial Y} \right)^2 \quad (20)$$

with the following boundary conditions.

Attached boundary layers:

$$H_1 = 0 \quad \text{at } Y = 0$$

$$H_1 = 0 \quad \text{at } Y = \infty$$

Free shear layers:

$$H_1 = 0 \quad \text{at} \quad Y = -\infty$$

$$H_1 = 0 \quad \text{at} \quad Y = \infty$$

Let H_2 be the solution of the equation

$$u^* \frac{\partial H_2}{\partial S} + v^* \frac{\partial H_2}{\partial Y} = \frac{1}{Pr} \frac{\partial^2 H_2}{\partial Y^2} \quad (21)$$

with boundary conditions given by

Attached boundary layers:

$$H_2 = 1 \quad \text{at} \quad Y = 0$$

$$H_2 = 0 \quad \text{at} \quad Y = \infty$$

Free shear layers:

$$H_2 = 1 \quad \text{at} \quad Y = -\infty$$

$$H_2 = 0 \quad \text{at} \quad Y = \infty$$

A solution of the energy equation may be constructed from a linear combination of H_1 and H_2 ,

$$H = H_1 + \lambda H_2 \quad (22)$$

where λ is a function of u_e , h_e , and h_w such that the boundary condi-

tions are satisfied. By requiring that the expression given by equation (22) be a solution of equation (16) satisfying the boundary conditions equations (17) and (18) the constant λ may be evaluated to give

$$\lambda = \frac{h_w^* - 1}{u_e^2/h_e}$$

and thus

$$H = H_1 + \frac{h_w^* - 1}{u_e^2/h_e} H_2$$

Then from equation (15) the enthalpy h^* is given by

$$h^* = 1 + \frac{u_e^2}{h_e} H_1 + (h_w^* - 1) H_2 \quad (23)$$

Equations (20) and (21) may be solved for H_1 and H_2 independent of u_e , h_e , and h_w^* . Then profiles of h^* for various values of u_e , h_e , and h_w^* may be computed from equation (23).

Transformation to Finite Interval

To permit application of the implicit finite-difference scheme discussed later, the interval of the normal coordinate must be finite. Previous solutions of the boundary-layer equations using the implicit technique have employed the Crocco transformation wherein the velocity u^* , which has a finite range, is used as an independent variable. (For example see Denison and Baum (6) and Kramer and Lieberstein (12).) For the present study another type of transformation was sought which would map the intervals $0 \leq Y < \infty$ and $-\infty < Y < \infty$ into finite intervals.

The transformation used here is from (S,Y) coordinates to (S,ζ) coordinates where ζ is a new normal coordinate defined by

$$\zeta = \tanh (\alpha Y) \quad (24)$$

and α is a dimensionless constant. The transformation defined by equation (24) maps the intervals $0 \leq Y < \infty$ and $-\infty < Y < \infty$ into the intervals $0 \leq \zeta < 1$ and $-1 < \zeta < 1$, respectively, as illustrated in Figure 5 for several values of α .

The transformation to (S,ζ) coordinates is preferred in the present analysis for the following reasons:

1. The transformation defined by equation (24) provides an explicit inverse relation between ζ and Y whereas the inversion of the Crocco transformation (i.e., from (S,u^*) to (S,Y) coordinates) requires an integration.
2. For the finite-difference solution using a mesh of equally-spaced grid points in the ζ -direction, the corresponding points along the Y -axis are more closely spaced near $Y = 0$ where more accuracy is desired to calculate velocity and enthalpy gradients. Thus the transformation magnifies that portion of the normal interval which is of most interest, as does the Crocco transformation.
3. For the shear layer calculations use of the Crocco transformation necessitates a separate solution to determine the velocity along the dividing streamline. As noted by Denison and Baum this solution also involves a starting problem at the separation point. In the (S,ζ) coordinate system employed

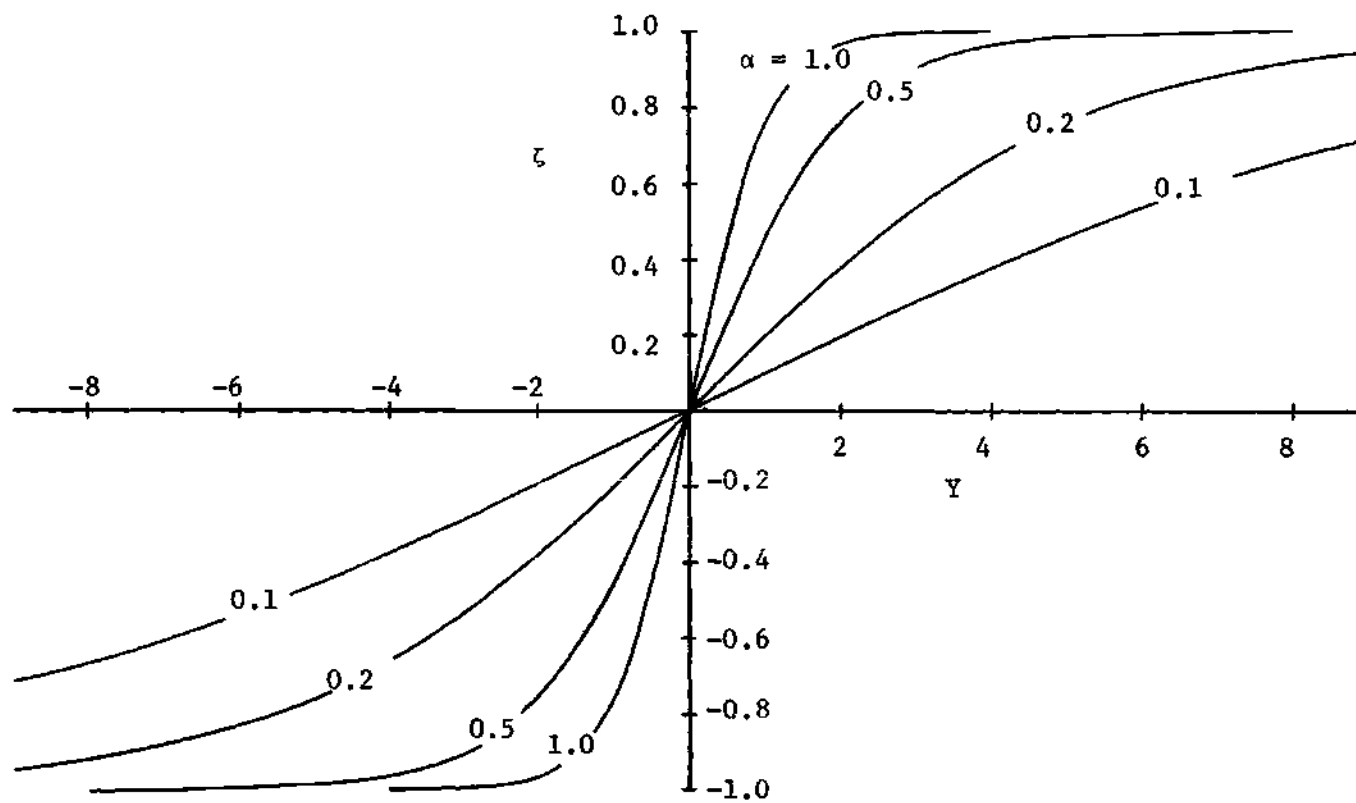


Figure 5. The Coordinate Transformation $\zeta = \tanh(\alpha Y)$ for Various Values of α .

here, the dividing streamline is located at $\zeta = 0$, which is one of the grid points in the finite-difference mesh, and thus no separate solution is required.

Since ζ is independent of S , the transformation from (S, Y) to (S, ζ) coordinates is accomplished by using the relations

$$\frac{\partial}{\partial Y} = \alpha(1 - \zeta^2) \frac{\partial}{\partial \zeta}$$

$$\frac{\partial^2}{\partial Y^2} = \alpha^2(1 - \zeta^2) \left[-2\zeta \frac{\partial}{\partial \zeta} + (1 - \zeta^2) \frac{\partial^2}{\partial \zeta^2} \right]$$

Introduction of these relations into equations (12), (14), (20), and (21) yields the following set of equations:

Continuity equation:

$$\frac{\partial u^*}{\partial S} + \alpha(1 - \zeta^2) \frac{\partial v^*}{\partial \zeta} = 0 \quad (25)$$

Momentum equation:

$$u^* \frac{\partial u^*}{\partial S} = -\alpha(1 - \zeta^2) \left[v^* + 2\alpha\zeta \right] \frac{\partial u^*}{\partial \zeta} \quad (26)$$

$$+ \alpha^2(1 - \zeta^2)^2 \frac{\partial^2 u^*}{\partial \zeta^2}$$

Energy equation:

$$u^* \frac{\partial H_1}{\partial S} = -\alpha(1 - \zeta^2) \left[v^* + \frac{2\alpha\zeta}{Pr} \right] \frac{\partial H_1}{\partial \zeta} \quad (27)$$

$$+ \frac{\alpha^2(1 - \zeta^2)^2}{Pr} \frac{\partial^2 H_1}{\partial \zeta^2} + \alpha^2(1 - \zeta^2)^2 \left(\frac{\partial u^*}{\partial \zeta} \right)^2$$

$$u^* \frac{\partial H_2}{\partial S} = -\alpha(1 - \zeta^2) \left[v^* + \frac{2\alpha\zeta}{Pr} \right] \frac{\partial H_2}{\partial \zeta} \quad (28)$$

$$+ \frac{\alpha^2(1 - \zeta^2)^2}{Pr} \frac{\partial^2 H_2}{\partial \zeta^2}$$

The transformation does not alter the fact that the energy equations (27) and (28) are uncoupled from the momentum and continuity equations. The boundary conditions are expressed in (S, ζ) coordinates as follows:

Attached boundary layers:

$$\left. \begin{aligned} u^* = v^* = 0 \quad , \quad H_1 = 0 \quad , \quad H_2 = 1 \quad \text{at} \quad \zeta = 0 \\ u^* = 1 \quad , \quad H_1 = H_2 = 0 \quad \quad \quad \text{at} \quad \zeta = 1 \end{aligned} \right\} \quad (29)$$

Free shear layers:

$$\left. \begin{aligned} u^* = 0 \quad , \quad H_1 = 0 \quad , \quad H_2 = 1 \quad \text{at} \quad \zeta = -1 \\ v^* = 0 \quad \quad \quad \quad \quad \quad \quad \quad \quad \quad \text{at} \quad \zeta = 0 \\ u^* = 1 \quad , \quad H_1 = H_2 = 0 \quad \quad \quad \quad \text{at} \quad \zeta = 1 \end{aligned} \right\} \quad (30)$$

In addition, the initial profiles in (S, ζ) coordinates must be specified. These are

$$\left. \begin{aligned} u^*(S, \zeta) &= u_o^*(\zeta) \\ v^*(S, \zeta) &= v_o^*(\zeta) \\ H_1(S, \zeta) &= H_{1o}(\zeta) \\ H_2(S, \zeta) &= H_{2o}(\zeta) \end{aligned} \right\} \quad \text{at } S = S_o \quad (31)$$

The Solution in Physical Coordinates

The solution of equations (25), (26), (27), and (28) yields velocity and enthalpy profiles in (S, ζ) coordinates. To obtain the profiles in the physical (x, y) coordinate system requires the inversion of the two transformations employed.

From equation (24), the inverse of the transformation to (S, ζ) coordinates is simply

$$\left. \begin{aligned} Y &= \frac{1}{2\alpha} \ln \left[\frac{1 + \zeta}{1 - \zeta} \right] \\ S &= S \end{aligned} \right\} \quad (32)$$

The transformation from (S, Y) coordinates to (x, y) coordinates is accomplished with the inverse of equation (8), namely

$$\left. \begin{aligned} y = \frac{L}{\sqrt{Re/C}} \int_0^Y \frac{\rho_e}{\rho} dY = \frac{L}{\sqrt{Re/C}} \int_0^Y T^* dY \\ x = LS \end{aligned} \right\} \quad (33)$$

where, from equation (4)

$$T^* = \frac{T}{T_e} = \frac{\rho_e}{\rho}$$

The constant C is evaluated from equation (9) using a reference temperature ratio T_r^* which corresponds to some mean temperature in the flow.

One such temperature ratio which includes the effects of freestream and wall conditions and yields satisfactory results is the reference temperature suggested by Eckert (13), namely

$$T_r^* = \frac{1}{2} + \frac{T_w^*}{2} + 0.22 \sqrt{Pr} \frac{u_e^2}{h_e} \quad (34)$$

The relation between y and Y (equation (33)) involves the temperature ratio T^* whereas the solution of the energy equation is in terms of the enthalpy ratio h^* . For a thermally perfect, diatomic gas the relation between h and T is given by

$$h = C_{p_a} T + h_{int} \quad (35)$$

where

$$C_{p_a} = \frac{\gamma_a R}{\gamma_a - 1}$$

is the specific heat at constant pressure for the active degrees of freedom of the molecules (i.e., translation and rotation), $\gamma_a = 7/5$, and h_{int} is the temperature-dependent enthalpy contribution due to vibration and electronic excitation. Using

$$h_{int}^* = \frac{h_{int}}{h_e}$$

the temperature ratio may be expressed as

$$T^* = \frac{h_e}{C_{p_a} T_e} (h^* - h_{int}^*) \quad (36)$$

and therefore the transformation relations (33) become

$$\left. \begin{aligned} y &= \frac{L}{\sqrt{Re/C}} \frac{h_e}{C_{p_a} T_e} \int_0^Y (h^* - h_{int}^*) dY \\ x &= LS \end{aligned} \right\} \quad (37)$$

For the special case of a gas with no vibration or electronic excitation or a gas with the vibrational energy fully excited (i.e., a calorically perfect gas),

$$T^* = h^*$$

and (33) becomes

$$\left. \begin{aligned} y &= \frac{L}{\sqrt{Re/C}} \int_0^Y h^* dY \\ x &= LS \end{aligned} \right\} \quad (38)$$

Substituting equation (23) into equation (38) yields the following relations for transforming from (S,Y) coordinates to (x,y) coordinates

$$\left. \begin{aligned} y &= \frac{L}{\sqrt{Re/C}} \left[Y + \frac{u_e^2}{h_e} \int_0^Y H_1 dY + (h_w^* - 1) \int_0^Y H_2 dY \right] \\ x &= LS \end{aligned} \right\} \quad (39)$$

Thus, velocity and enthalpy profiles in (S,ζ) coordinates may be transformed to physical coordinates by using equation (32) and either equation (37) for a thermally perfect gas or equation (39) for a thermally and calorically perfect gas.

CHAPTER III

METHOD OF SOLUTION

The finite-difference solution of the equations derived in the preceeding chapter is treated in this chapter. First, the finite-difference analog of the system of differential equations is derived, the solution procedure is described, and the stability of the numerical solution is explored. Second, the method of evaluation of the heat transfer in attached and separated flows is discussed.

The Finite-Difference Solution

The solution method employed in the present study is an implicit, finite-difference technique, wherein the governing partial differential equations are replaced by an equivalent set of partial difference equations. The numerical solution of these difference equations will then approximate the solution of the differential equations provided certain stability and convergence criteria are satisfied.

The method of finite differences is well developed for systems of linear partial differential equations. (For example see references (14) and (15).) More recently, the method of finite differences has been employed in the solution of systems of non-linear partial differential equations using both explicit and implicit techniques. In particular, finite-difference solutions of the Prandtl boundary-layer equations for steady, laminar, compressible flow have been reported in references (12), (16), (17), (18), (19), and (20).

In the present study the implicit technique is favored over the explicit technique because the implicit technique offers the advantage of much less stringent stability requirements, although the numerical computations using the explicit technique are somewhat less involved. The stability characteristics of explicit and implicit finite-difference formulations have been discussed in reference (21), and the stability advantages of implicit schemes have been exploited, for example, in references (6) and (22).

Derivation of the Difference Equations

The lattice shown in Figure 6 is used in the finite-difference approximations. The mesh points are equally-spaced in the ζ -direction. The finite-difference approximations for the partial derivatives appearing in the momentum and energy equations are similar to those used in reference (6). An average central difference approximation is used in the ζ -direction in order to enhance the stability of the solution (6), while a forward difference approximation is used in the S -direction. These finite-difference approximations are

$$\left. \begin{aligned} \frac{\partial g}{\partial S} &= \frac{g_{i+1,j} - g_{i,j}}{\Delta S} \\ \frac{\partial g}{\partial \zeta} &= \frac{g_{i+1,j+1} - g_{i+1,j-1} + g_{i,j+1} - g_{i,j-1}}{4\Delta\zeta} \\ \frac{\partial^2 g}{\partial \zeta^2} &= \frac{1}{2(\Delta\zeta)^2} (g_{i+1,j+1} - 2g_{i+1,j} + g_{i+1,j-1} + g_{i,j+1} \\ &\quad - 2g_{i,j} + g_{i,j-1}) \end{aligned} \right\} \quad (40)$$

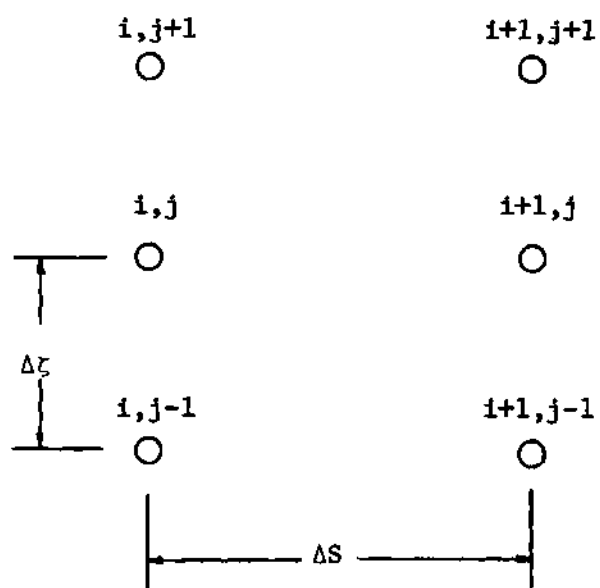


Figure 6. The Finite-Difference Lattice.

where g is any of the dependent variables whose derivative appears in the momentum or energy equations, i is the S -index, j is the ζ -index, ΔS is the increment between stations i and $i + 1$, and $\Delta \zeta$ is the increment in the normal coordinate.

Introduction of equations (40) into the momentum equation (26) leads to the following expression relating the unknown streamwise velocities at station $i + 1$:

$$A_1(i,j)u_{i+1,j-1}^* + A_2(i,j)u_{i+1,j}^* + A_3(i,j)u_{i+1,j+1}^* = B(i,j) \quad (41)$$

where

$$A_1(i,j) = \alpha(1 - \zeta^2) \left[\frac{v_{av}^* + 2\alpha\zeta}{4\Delta\zeta} + \frac{\alpha(1 - \zeta^2)}{2(\Delta\zeta)^2} \right]$$

$$A_2(i,j) = - \left[\frac{\alpha(1 - \zeta^2)}{\Delta\zeta} \right]^2 - \frac{u_{av}^*}{\Delta S}$$

$$A_3(i,j) = \alpha(1 - \zeta^2) \left[- \frac{v_{av}^* + 2\alpha\zeta}{4\Delta\zeta} + \frac{\alpha(1 - \zeta^2)}{2(\Delta\zeta)^2} \right]$$

$$B(i,j) = -A_1(i,j)u_{i,j-1}^* - \left[A_2(i,j) + \frac{2u_{av}^*}{\Delta S} \right] u_{i,j}^*$$

$$-A_3(i,j)u_{i,j+1}^*$$

and

$$u_{av}^* = \frac{u_{i+1,j}^* + u_{i,j}^*}{2}, \quad v_{av}^* = \frac{v_{i+1,j}^* + v_{i,j}^*}{2} \quad (42)$$

The energy equations (27) and (28) assume a form similar to equation (41) above in difference form, namely

$$C_1(i,j)H_{1_{i+1,j-1}} + C_2(i,j)H_{1_{i+1,j}} + C_3(i,j)H_{1_{i+1,j+1}} = D_1(i,j) \quad (43)$$

$$C_1(i,j)H_{2_{i+1,j-1}} + C_2(i,j)H_{2_{i+1,j}} + C_3(i,j)H_{2_{i+1,j+1}} = D_2(i,j) \quad (44)$$

where

$$C_1(i,j) = \alpha(1 - \zeta^2) \left[\frac{1}{4\Delta\zeta} \left[v_{av}^* + \frac{2\alpha\zeta}{Pr} \right] + \frac{\alpha(1 - \zeta^2)}{2Pr(\Delta\zeta)^2} \right]$$

$$C_2(i,j) = -\frac{1}{Pr} \left[\frac{\alpha(1 - \zeta^2)}{\Delta\zeta} \right]^2 - \frac{u_{av}^*}{\Delta S}$$

$$C_3(i,j) = \alpha(1 - \zeta^2) \left[-\frac{1}{4\Delta\zeta} \left[v_{av}^* + \frac{2\alpha\zeta}{Pr} \right] + \frac{\alpha(1 - \zeta^2)}{2Pr(\Delta\zeta)^2} \right]$$

$$D_1(i,j) = -C_1(i,j)H_{1_{i,j-1}} - \left[C_2(i,j) + \frac{2u_{av}^*}{\Delta S} \right] H_{1_{i,j}} - C_3(i,j)H_{1_{i,j+1}} \\ - \left[\frac{\alpha(1 - \zeta^2)(u_{i+1,j+1}^* - u_{i+1,j-1}^* + u_{i,j+1}^* - u_{i,j}^*)}{4\Delta\zeta} \right]^2$$

and

$$D_2(i,j) = -C_1(i,j)H_{2_{i,j-1}} - \left[C_2(i,j) + \frac{2u_{av}^*}{\Delta S} \right] H_{2_{i,j}} - C_3(i,j)H_{2_{i,j+1}}$$

The finite-difference approximations employed for the continuity equation are slightly different from those used in the momentum and energy equations. Following the suggestion of Wu (17), the continuity equation

is evaluated at a point midway between the grid points $i+1,j$ and $i+1,j-1$. The derivative $\frac{\partial u^*}{\partial S}$ at this point is taken as the average of the values at $i+1,j$ and $i+1,j-1$. Using a backward difference form, this becomes

$$\frac{\partial u^*}{\partial S} = \frac{u_{i+1,j}^* - u_{i,j}^* + u_{i+1,j-1}^* - u_{i,j-1}^*}{2\Delta S}$$

Using a central difference approximation for $\frac{\partial v^*}{\partial \zeta}$ gives

$$\frac{\partial v^*}{\partial \zeta} = \frac{v_{i+1,j}^* - v_{i+1,j-1}^*}{\Delta \zeta}$$

The resulting finite-difference form of the continuity equation is

$$v_{i+1,j}^* = v_{i+1,j-1}^* - \frac{\Delta \zeta}{2\alpha\Delta S} \frac{(u_{i+1,j}^* - u_{i,j}^* + u_{i+1,j-1}^* - u_{i,j-1}^*)}{\left[1 - \frac{(\zeta_j + \zeta_{j-1})^2}{4}\right]} \quad (45)$$

As pointed out in references (17) and (23), the advantage of this form is that it employs a central difference approximation for $\frac{\partial v^*}{\partial \zeta}$ which is a better approximation than a forward or backward difference approximation and, in addition, permits the direct calculation of v^* at each grid point provided that the value of v^* is known at one grid point and that u^* is known for all grid points at stations i and $i+1$.

A slightly altered form of equation (45) is used for that portion of the shear layer below the dividing streamline, where the value of v^* is computed using the known value at the grid point just above. Increasing the j -index in equation (45) by one and solving for $v_{i+1,j}^*$ results in the relation

$$v_{i+1,j}^* = v_{i+1,j+1}^* + \frac{\Delta \zeta}{2\alpha \Delta S} \frac{(u_{i+1,j}^* - u_{1,j}^* + u_{i+1,j+1}^* - u_{1,j+1}^*)}{\left[1 - \frac{(\zeta_j + \zeta_{j+1})^2}{4}\right]} \quad (46)$$

Equations (41), (43), (44), (45), and (46) form a set of partial difference equations whose solution yields velocity and enthalpy profiles in (S, ζ) coordinates.

Solution for the Velocity Profiles

At each streamwise station S a lattice of $N + 1$ equally-spaced grid points $j = 0, 1, 2, \dots, N$ is placed in the ζ -direction. With specified values of u_{av}^* and v_{av}^* and known profiles of u^* and v^* at some station i , equation (41) is written for the interior mesh points $j = 1, 2, 3, \dots, N-1$ at the next station $i+1$ resulting in a system of equations in the unknown $u_{i+1,j}^*$ at the interior grid points. This system is completed by specifying the boundary values $u_{i+1,0}^*$ and $u_{i+1,N}^*$ from the boundary conditions. Since this system is tridiagonal (i.e., the only non-zero elements in the coefficient matrix are those along the main diagonal and the elements to either side of the diagonal elements), it may be solved rapidly using the equivalent of Gaussian elimination as described in reference (22).

With values of $u_{i+1,j}^*$ given by the solution of the system described above, the continuity equation (either equation (45) or (46)) is employed as an auxiliary equation to compute values of $v_{i+1,j}^*$ using $v_{i+1,0}^* = 0$ (i.e., $v^* = 0$ at $\zeta = 0$).

Since the expressions for u_{av}^* and v_{av}^* involve the unknowns $u_{i+1,j}^*$ and $v_{i+1,j}^*$ the system described is nonlinear, necessitating an iterative solution. In the present study the velocity profiles were ob-

tained using the computational algorithm outlined below.

- a. With values of $u_{i,j}^*$ and $v_{i,j}^*$ known either from initial profiles or the solution at a previous station, set

$$u_{av}^* = u_{i,j}^* \quad , \quad v_{av}^* = v_{i,j}^*$$

- b. Using these values of u_{av}^* and v_{av}^* evaluate the coefficients in equation (41) and solve the resulting system for approximate values of $u_{i+1,j}^*$.
- c. With these approximate values of $u_{i+1,j}^*$ compute the corresponding values of $v_{i+1,j}^*$ from equation (45) or (46).
- d. Compute new values of u_{av}^* and v_{av}^* using

$$u_{av}^* = \frac{u_{i+1,j}^* + u_{i,j}^*}{2} \quad , \quad v_{av}^* = \frac{v_{i+1,j}^* + v_{i,j}^*}{2}$$

- e. Repeat steps b, c, and d until successive values of u_{av}^* and v_{av}^* agree within some specified tolerance. All of the results presented in this study were obtained by requiring that successive values of u_{av}^* and v_{av}^* agree to within one tenth of one per cent.
- f. When the condition of step e is satisfied proceed to the calculation of the next step.

With the velocity profiles provided by the above procedure, the solution of equations (43) and (44) for the two enthalpy functions H_1 and H_2 may be accomplished.

Solution of the Energy Equation

Writing the two difference equations (43) and (44) for the interior grid points $j = 1, 2, 3, \dots, N-1$ yields two tridiagonal systems which are completed by specifying the boundary values $H_{1+1,0}$, $H_{1+1,N}$, $H_{2+1,0}$, and $H_{2+1,N}$. Note that the coefficient matrix is the same for both systems, reducing the number of calculations somewhat. Since the coefficient matrix is constructed using u_{av}^* and v_{av}^* furnished by the solution of the momentum and continuity equations, no iteration is required to compute $H_{1+1,j}$ and $H_{2+1,j}$. The Gaussian elimination procedure is also utilized in the solution of the system of equations for $H_{1+1,j}$ and $H_{2+1,j}$.

With profiles of H_1 and H_2 provided by the solution method described above, the enthalpy ratio h^* may be computed from equation (23) for given values of u_e , h_e , and h_w . Then with h^* known, the transformation back to physical coordinates as described in Chapter II may be accomplished.

Stability of the Finite-Difference Solution

When the numerical solution of the finite-difference analog of a differential equation is used as an approximation to the solution of the differential equation, two questions arise concerning the accuracy of the solution.

- (1) Is the numerical solution of the difference equation stable with respect to roundoff errors, and
- (2) does the exact solution of the finite-difference equation converge to the solution of the differential equation as the

distance between grid points in the difference mesh is decreased?

With the aid of certain assumptions, the stability of the momentum difference equation (41) used here may be analyzed. Such an analysis is presented in Appendix A. The analysis considers the linearized form of the momentum difference equation. The linearized form is obtained by assuming that the non-linear coefficients may be replaced by suitable average values which are constant over each interval ΔS . This assumption leads to the conclusion that the momentum difference equation is stable for any step size ΔS , provided that the condition $u_{av}^* \geq 0$ is satisfied. In the present case this condition is always satisfied.

The continuity difference equation is linear, and, with the derivative $\frac{\partial u}{\partial S}^*$ specified from the stable solution of equation (41), roundoff errors in the calculation of $v_{i+1,j}^*$ are simply added at each step. Since roundoff errors occur randomly, their sum is bounded, and the continuity difference equation is stable.

The conditions for stability of the finite-difference equations for the enthalpy functions H_1 and H_2 are revealed by a comparison of these equations with the momentum difference equation (41). The form of equation (44) for H_2 differs from that of the momentum equation (41) only in the appearance of the Prandtl number in the coefficients. The results of the stability analysis presented in Appendix A applies directly to the solution for H_2 since the Prandtl number is always positive. The form of equation (43) for H_1 differs from that of equation (44) only in the additional term involving the velocity derivative. Since the velocity field is specified from the solution of the momentum and continuity equations and

since a specified term does not affect the growth of error in the numerical procedure, the stability analysis of Appendix A also applies to equation (43). Thus the conditions for a stable solution for the enthalpy functions are the same as those for the solution for the velocity profiles.

While the question of convergence is not treated here, Hildebrand (23) asserts that existing evidence indicates that a finite-difference formulation which is stable is also convergent.

Evaluation of the Heat Transfer

Attached-Flow Regions

The local heat transfer rate q_{att} for an attached boundary layer at station x is given by

$$q_{att}(x) = \left[k \frac{\partial T}{\partial y} \right]_{y=0} \quad (47)$$

where q_{att} is the heat addition rate to the surface and k is the coefficient of thermal conductivity

$$k = \frac{C_p \mu}{Pr}$$

Substituting for k and transforming x and y to S and Y , equation (47) becomes

$$q_{att}(S) = \frac{C_p h_e}{LPr} \sqrt{\frac{Re}{C}} \left[\frac{\partial h^*}{\partial Y} \right]_{Y=0}$$

Equation (23) gives

$$\left(\frac{\partial h^*}{\partial Y} \right)_{Y=0} = \frac{u_e^2}{h_e} \left(\frac{\partial H_1}{\partial Y} \right)_{Y=0} + (h_w^* - 1) \left(\frac{\partial H_2}{\partial Y} \right)_{Y=0}$$

so that

$$q_{att}(S) = \frac{C\mu_e h_e}{LPr} \sqrt{\frac{Re}{C}} \left[\frac{u_e^2}{h_e} \left(\frac{\partial H_1}{\partial Y} \right)_{Y=0} + (h_w^* - 1) \left(\frac{\partial H_2}{\partial Y} \right)_{Y=0} \right] \quad (48)$$

The numerical solution of the energy equation described previously is carried out without considering specific freestream and wall conditions. In like manner, the heat transfer rate may be written in a form which is valid for a number of freestream and wall conditions. For adiabatic conditions, $q_{att}(S) = 0$ and $h_w^* = h_{aw}^*$ so from equation (48)

$$\frac{u_e^2}{h_e} \left(\frac{\partial H_1}{\partial Y} \right)_{Y=0} = -(h_{aw}^* - 1) \left(\frac{\partial H_2}{\partial Y} \right)_{Y=0}$$

Therefore

$$\frac{q_{att}(S)}{\rho_e u_e (h_w^* - h_{aw}^*)} \sqrt{\frac{Re}{C}} = \frac{1}{Pr} \left(\frac{\partial H_2}{\partial Y} \right)_{Y=0} \quad (49)$$

Define an average heat transfer rate to an attached-flow region by

$$\bar{q}_{att} = \frac{1}{L} \int_0^S q_{att}(S) \, dS$$

Introducing equation (49) results in the expression

$$\frac{\bar{q}_{att}}{\rho_e u_e (h_w - h_{aw})} \sqrt{\frac{Re}{C}} = \frac{1}{Pr} \int_0^S \left(\frac{\partial H_2}{\partial Y} \right)_{Y=0} dS \quad (50)$$

For comparison, expressions similar to equations (49) and (50) for the local heat transfer rate q_{bl} and the average heat transfer rate \bar{q}_{bl} to a flat plate may be expressed from reference 2 as

$$\frac{q_{bl}(S)}{\rho_e u_e (h_w - h_{aw})} \sqrt{\frac{Re}{C}} = \frac{0.29575}{Pr \sqrt{S}} \quad (51)$$

and

$$\frac{\bar{q}_{bl}}{\rho_e u_e (h_w - h_{aw})} \sqrt{\frac{Re}{C}} = \frac{0.5915}{Pr} \sqrt{S} \quad (52)$$

Separated-Flow Regions

The evaluation of the heat transfer to regions of separated flow is not as straightforward as for attached flow. As a consequence of assuming that the influence of the cavity floor on the shear layer is negligible, the temperature gradient, and thus the local heat transfer rate, cannot be evaluated at the cavity floor. Thus, as noted by Chapman, an energy balance for the separated-flow region is required to evaluate the total heat transfer rate.

For a closed surface Ω , the conservation of energy for steady flow requires that

$$\left[\begin{array}{c} \text{Rate of heat} \\ \text{input across} \\ \Omega \end{array} \right] = \left[\begin{array}{c} \text{Rate of work done} \\ \text{by gas through} \\ \text{normal pressures} \\ \text{on } \Omega \end{array} \right] + \left[\begin{array}{c} \text{Rate of work done} \\ \text{by gas through} \\ \text{tangential stresses} \\ \text{on } \Omega \end{array} \right]$$

For a cavity of length x , the energy balance above for the closed surface consisting of the dividing streamline and the cavity walls yields the expression

$$\frac{1}{L} \int_0^x \left(k \frac{\partial T}{\partial y} \right)_{y=0} dx - \bar{q}_{\text{sep}} = \frac{1}{L} \int_0^x \left(\mu \frac{\partial u}{\partial y} \right)_{y=0} (-u)_{y=0} dx \quad (53)$$

where \bar{q}_{sep} is the average heat transfer rate to the cavity walls.

Transforming to S and Y results in the relation

$$\frac{\bar{q}_{\text{sep}}}{\rho_e u_e} = \sqrt{\frac{C}{\text{Re}}} \left[\frac{h_e}{\text{Pr}} \int_0^S \left(\frac{\partial h^*}{\partial Y} \right)_{Y=0} dS + u_e^2 \int_0^S \left(u^* \frac{\partial u^*}{\partial Y} \right)_{Y=0} dS \right]$$

Substituting for $\left(\frac{\partial h^*}{\partial Y} \right)_{Y=0}$ yields

$$\begin{aligned} \frac{\bar{q}_{\text{sep}}}{\rho_e u_e} = \sqrt{\frac{C}{\text{Re}}} & \left[\frac{h_e}{\text{Pr}} (h_w^* - 1) \int_0^S \left(\frac{\partial H_2}{\partial Y} \right)_{Y=0} dS \right. \\ & \left. + u_e^2 \int_0^S \left(u^* \frac{\partial u^*}{\partial Y} + \frac{1}{\text{Pr}} \frac{\partial H_1}{\partial Y} \right)_{Y=0} dS \right] \end{aligned} \quad (54)$$

The average heat transfer is expressed in the form of equation (50) in the following manner. Under adiabatic conditions $\bar{q}_{sep} = 0$ and $h_w^* = h_{aw}^*$, thus

$$\frac{u_e^2}{h_e} \int_0^S \left(u^* \frac{\partial u^*}{\partial Y} + \frac{1}{Pr} \frac{\partial H_1}{\partial Y} \right)_{Y=0} dS = - \frac{(h_{aw}^* - 1)}{Pr} \int_0^S \left(\frac{\partial H_2}{\partial Y} \right)_{Y=0} dS$$

Inserting this relation into equation (54) gives

$$\frac{\bar{q}_{sep}}{\rho_e u_e (h_w - h_{aw})} \sqrt{\frac{Re}{C}} = \frac{1}{Pr} \int_0^S \left(\frac{\partial H_2}{\partial Y} \right)_{Y=0} dS \quad (55)$$

Note that equations (55) and (50) are identical in form. This permits the calculation of the overall heat transfer to a combination of separated and attached flows by simply integrating $\left(\frac{\partial H_2}{\partial Y} \right)_{Y=0}$ over the entire region, provided the wall and freestream conditions are the same and that h_{aw} is the same for both attached and separated flows. Chapman's theory predicts that the average recovery factor, and hence h_{aw} , is essentially the same for both separated and attached flows. For $Pr = 0.72$, the theory predicts a recovery factor $r = 0.850$. The recovery factor for an attached flow with $Pr = 0.72$ is $r = \sqrt{Pr} = 0.849$. This difference is negligible and therefore h_{aw} is assumed to be the same for both separated- and attached-flow regions in the present study. Thus the average heat transfer rate \bar{q} to a surface consisting of both separated- and attached-flow regions may be written as

$$\frac{\bar{q}}{\rho_e u_e (h_w - h_{aw})} \sqrt{\frac{Re}{C}} = \frac{1}{Pr} \int_0^S \left(\frac{\partial H_2}{\partial Y} \right)_{Y=0} dS \quad (56)$$

While the local heat transfer rates along the cavity floor corresponding to equation (49) cannot be determined from this analysis, it is still possible to consider "local" rates in the sense that local gradients along the dividing streamline may be evaluated and a "local" heat transfer rate for shear layers q_{sep} may be defined by

$$\frac{q_{sep}(S)}{\rho_e u_e (h_w - h_{aw})} \sqrt{\frac{Re}{C}} = \frac{1}{Pr} \left(\frac{\partial H_2}{\partial Y} \right)_{Y=0} \quad (57)$$

It should be emphasized that equation (57) does not provide the local heat transfer rate along the cavity floor, since this is dependent upon the recirculating flow in the cavity. Nevertheless, equation (57) is a convenient expression.

The desired result of this analysis is the comparison of the overall heat transfer rate to a surface with cavity-separated regions with that to an equivalent completely-attached flow. The advantage (or disadvantage) of employing the cavity-separated flow model is reflected in the ratio of overall heat transfer rates \bar{q}^* defined by

$$\bar{q}^* = \frac{\bar{q}}{\bar{q}_{b1}} \quad (58)$$

where \bar{q} is given by equation (56) and \bar{q}_{b1} is given by equation (52).

Equation (52) is used for this comparison rather than results from the

finite-difference solution since results presented in Appendix B show that the finite-difference results agree with equation (52) for values of S of interest here.

In addition a ratio of local heat transfer rates q^* may be defined by

$$q^* = \frac{q}{q_{b1}} \quad (59)$$

where $q = q_{att}$ for the attached-flow regions, $q = q_{sep}$ for the separated-flow regions, and q_{b1} is computed from equation (51).

Check of the Solution Method

To investigate the accuracy of the numerical method and to establish a satisfactory grid size, the numerical solution was applied to problems whose solutions are available in the literature. Both the flat plate (Blasius) and the free shear layer problems were selected for this investigation since they possess velocity and enthalpy profiles which are similar to those of the present study. These investigations are discussed in detail in Appendices B and C, and the results are summarized here.

The numerical solutions for both the flat-plate boundary layer and the non-similar free shear layers with finite initial thickness converged to the solutions given in the literature. Furthermore, the similar free shear layer profiles of Chapman are accurately preserved by the numerical solution. In a small region near where the boundary layer or free shear layer initiates, the numerical solutions differ

substantially from the exact solutions because of the large velocity and enthalpy gradients. The streamwise distance S required for the numerical solution to converge to an accurate solution is, of course, dependent upon the step sizes selected for the S and ζ coordinates. Comparisons in Appendix B show that the numerical results for the integrated heat transfer rates to a flat plate converge to within one per cent of the predictions of reference (2) at $S = 10^{-1}$ if

- (1) the interval from $S = 0$ to $S = 1$ is subdivided into 100 steps varying such that the step size is proportional to the square root of S ,
- (2) the interval from $\zeta = 0$ to $\zeta = 1$ (i.e., $Y = 0$ to $Y = \infty$) is initially subdivided into 25 equal steps and the transformation constant α and the number of grid points adjusted to assure that at least two grid points at any streamwise station are outside the boundary layer, and
- (3) the enthalpy gradient at $\zeta = Y = 0$ is evaluated using a parabolic curve fit.

Also, as shown in Appendix C, the velocities along the dividing streamline agree within one per cent of the values of reference (6) at $S = 10^{-2}$ if these step sizes are employed. Since the present study will consider geometries for which $S \geq 10^{-1}$ these step sizes are used for computing the velocity and enthalpy profiles for the results presented herein and the gradients at $Y = 0$ are evaluated using a parabolic curve fit.

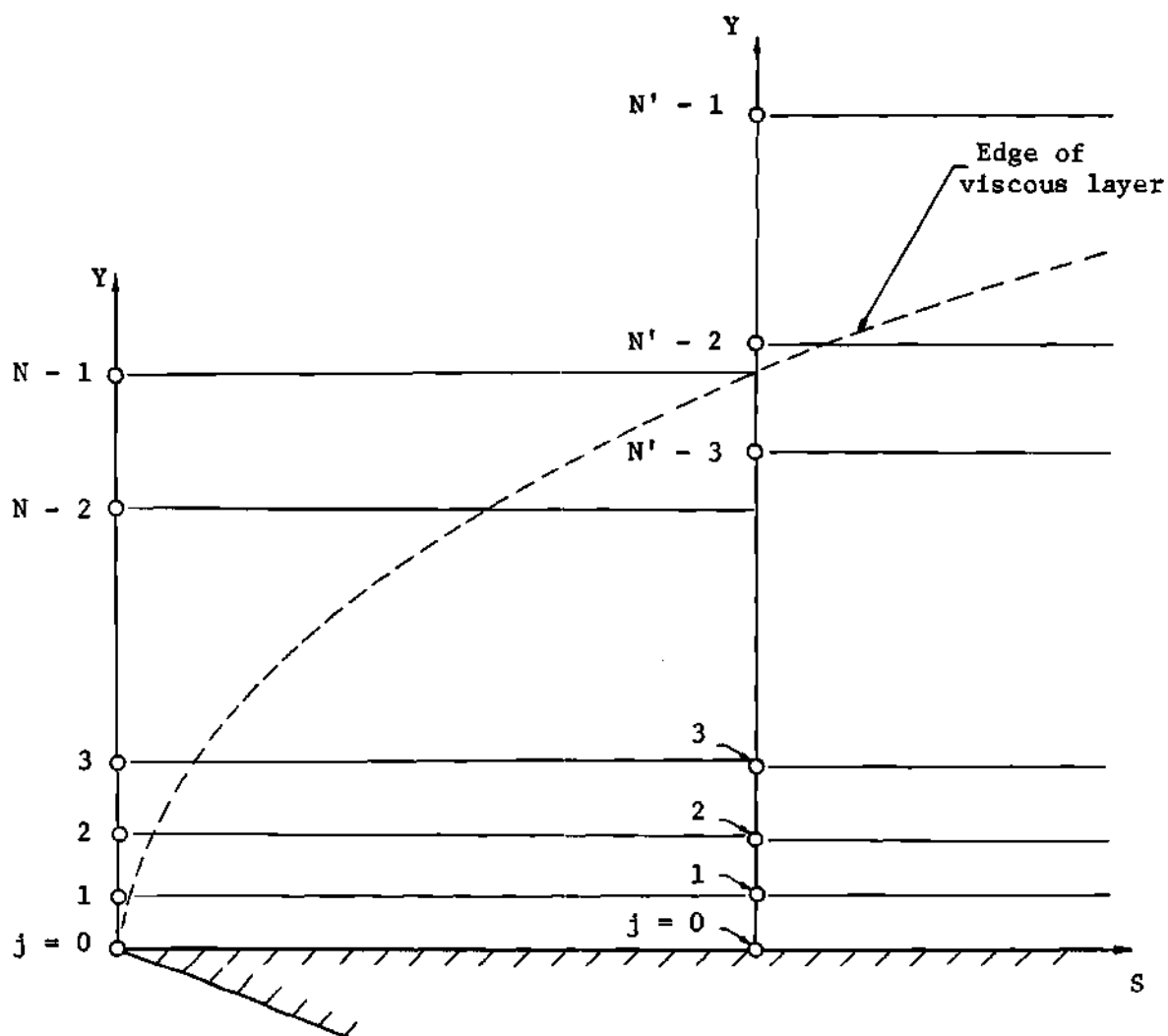
The use of a streamwise step interval ΔS which varies as the square root of S allows the use of small steps for small values of S

where gradients are large while permitting relatively large steps in S for large S where the gradients are smaller. This is an advantage over the use of a constant value of ΔS , since a value ΔS small enough to provide accurate results for small S would require an excessive amount of computation for large values of S .

When the edge of the viscous layer reaches the next-to-last grid point (corresponding to the last finite value of Y) as depicted in Figure 7, N is increased by 20 per cent to N' and the transformation constant α is adjusted so that the Y -spacing for the first grid point (i.e., between $j = 0$ and $j = 1$) is unchanged. Thus, at least one additional grid point is located outside the viscous layer and the Y -spacing for all the grid points other than the first is slightly reduced. This assures that the numerical accuracy is at least maintained without excessively reducing the computing efficiency.

Application to the Present Study

The particular geometry chosen for the numerical study of the heat transfer rates to multiple-cavity configurations with sharp-cusp reattachment geometries is illustrated in Figure 8. Each cavity is the same length L , and each attached-flow region between cavities is of length L_a . Various values of $L^* = L_a/L$ are considered, and two cases are considered for the initial attached-flow length L_s , namely, $L_s = L_a$ and $L_s = L$. The streamwise distance from the initial point of the surface is termed S . The distance downstream of the initial attached-flow region divided by the cavity length is denoted \tilde{S} , and the distance downstream of each reattachment point divided by the cavity



Note: The points in the Y-direction depicted here correspond to the equally-spaced grid points in the ζ -direction.

Figure 7. Illustration of Alteration of Finite-Difference Mesh.

$$L^* = \frac{L_a}{L}$$

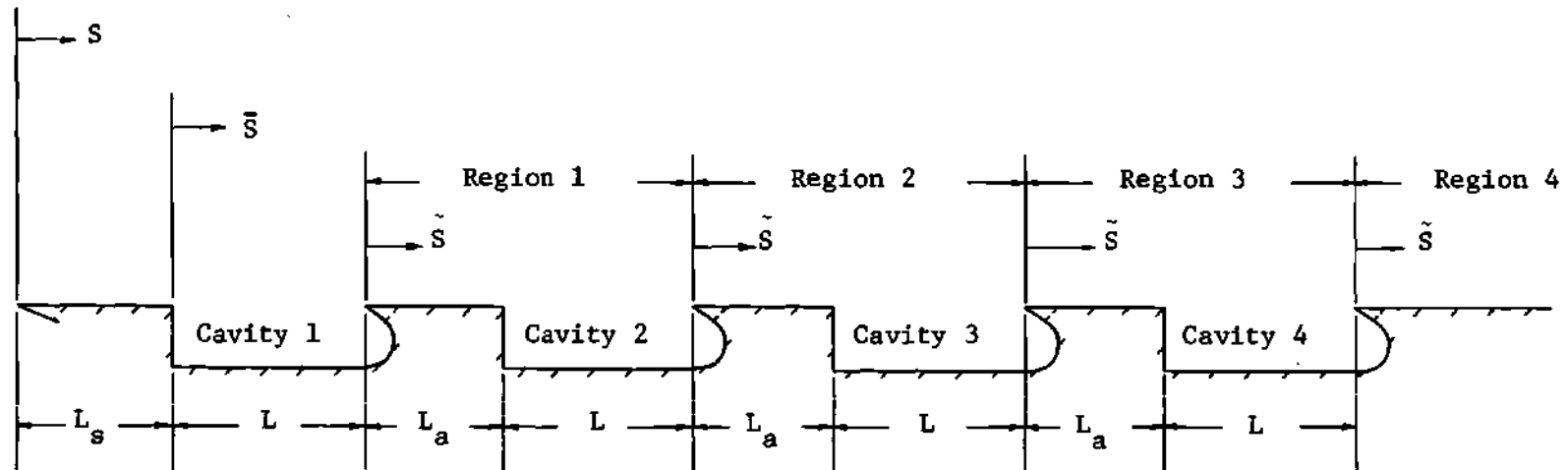


Figure 8. The Physical Model for the Heat Transfer Study.

length is called \tilde{S} . These quantities are depicted in Figure 8.

Based on the results of the check of the solution method, the following grid sizes are employed for this geometry:

1. The finite-difference lattice starts with $N = 25$ at $S = 0$, and N is increased by 20 per cent whenever the edge of the viscous layer reaches the next-to-last grid point.
2. The streamwise step interval ΔS is varied as the square root of the distance downstream of the reattachment point for attached boundary layers or the distance downstream of the separation point for free shear layers.

Application of the numerical solution method used here to this geometry requires the specification of the initial profiles for the attached boundary layers and free shear layers originating from each of the separation and reattachment points. Uniform velocity and enthalpy profiles are used for $S = 0$ with a discontinuity at $\zeta = 0$, where the velocity and enthalpy are given by the boundary conditions for attached boundary layers. At each separation point, the initial conditions for the free shear layer solution are determined in the following manner. The difference mesh for the interval $-1 \leq \zeta \leq 0$ employs the same number of grid points as for the interval $0 \leq \zeta \leq 1$. The values of the dependent variables at each of the grid points above $\zeta = 0$ are taken from the solution for the attached boundary layer at the separation point, while the values at the grid points for $\zeta \leq 0$ are given by the free shear layer boundary conditions at $\zeta = -1$. At each reattachment point, the initial conditions for the attached boundary layer solution are determined by using the values from the free shear

layer solution at that point for $\zeta > 0$. Thus the initial profile for each attached-flow region following a cavity is a discontinuous profile corresponding to the upper half of a free shear layer profile with the boundary conditions for attached boundary layers at $\zeta = 0$.

CHAPTER IV

RESULTS AND DISCUSSION

Heat Transfer Results from the Numerical Solution

The finite-difference solution method was applied to a four-cavity configuration with sharp-cusp reattachment geometries like that depicted in Figure 8. Typical results for the local heat transfer rates are presented in Figure 9. For comparison, the local heat transfer rates to an equivalent completely-attached flow given by equation (51) are also shown. The reduced "local" heat transfer rates over each of the cavities are accompanied by elevated heat transfer rates over the attached-flow regions between the cavities.

The results of Figure 9 are presented in Figure 10 in terms of the ratio of the local heat transfer rates to the heat transfer rates for the equivalent completely-attached flow, q^* (i.e., the ratio of the solid to the dashed line in Figure 9). These results indicate the relative increase or decrease of the local heat transfer rates in comparison to a completely-attached flow. The form of the results over each of regions 1, 2, 3, and 4 in terms of q^* are remarkably similar. To investigate this similarity in the values of q^* for each region the local heat transfer rates for regions 1, 2, 3, and 4 were computed for L^* equal to 0.1, 0.25, 0.5, 1, and 2 using an initial attached-flow length $L_s = L_a$. These local heat transfer rates are presented in Figures 11 through 15 in terms of the parameter \tilde{S} , which is the dis-

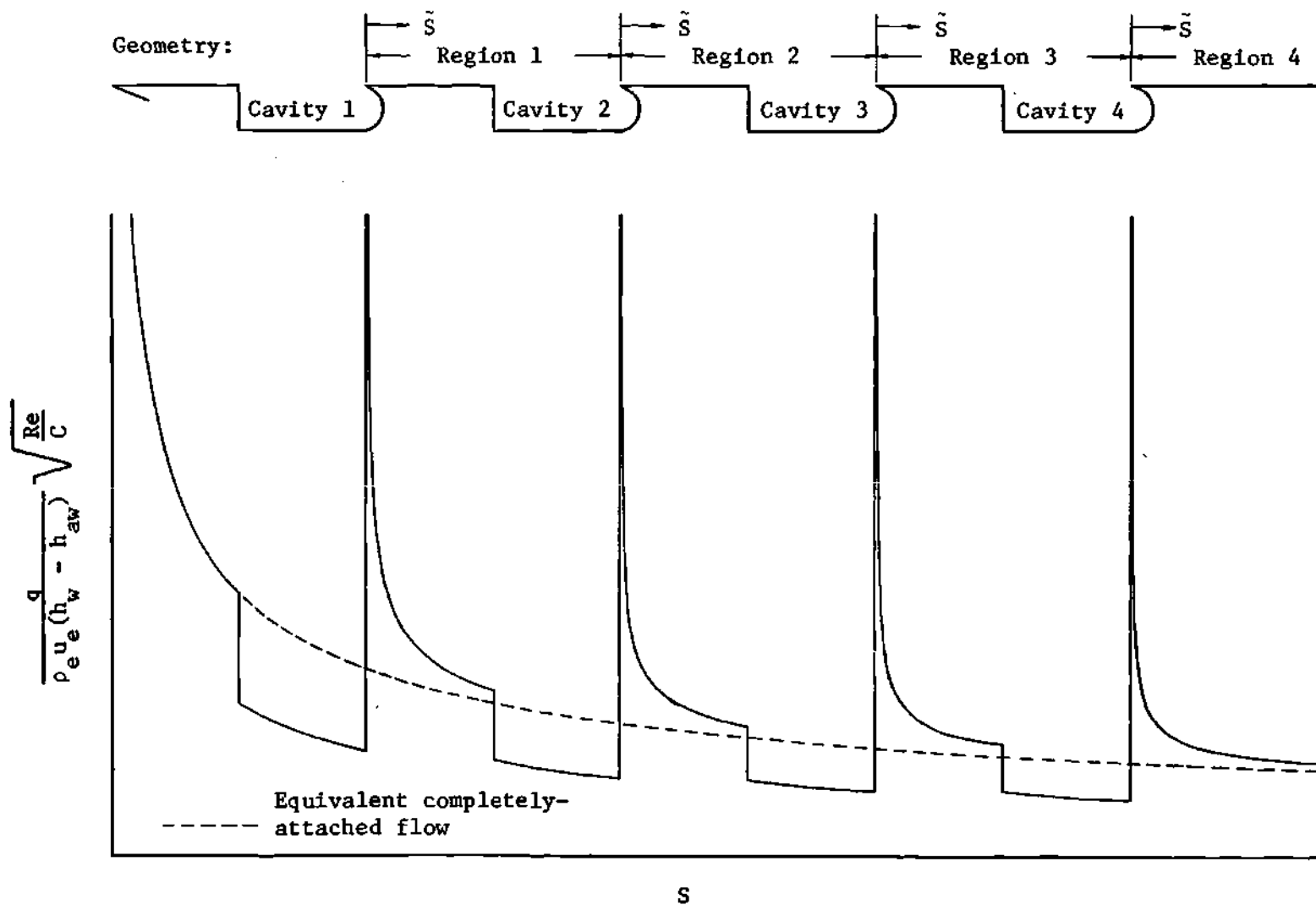


Figure 9. Typical Local Heat Transfer Results from the Numerical Solution and Comparison with Equivalent Completely-Attached Flow ($L^* = 1$, $Pr = 0.72$).

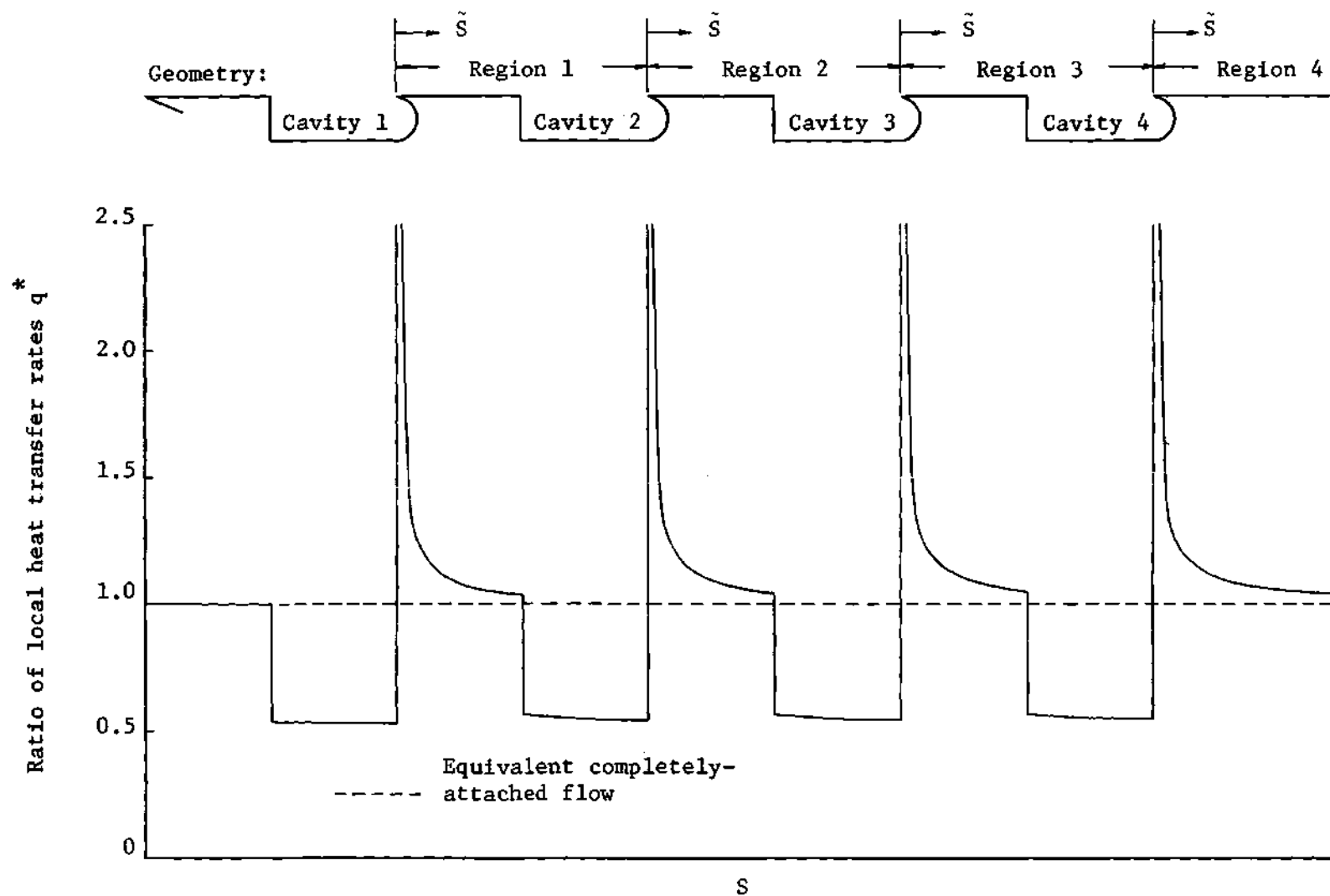


Figure 10. Typical Local Heat Transfer Ratio Results from the Numerical Solution ($Pr = 0.72$).

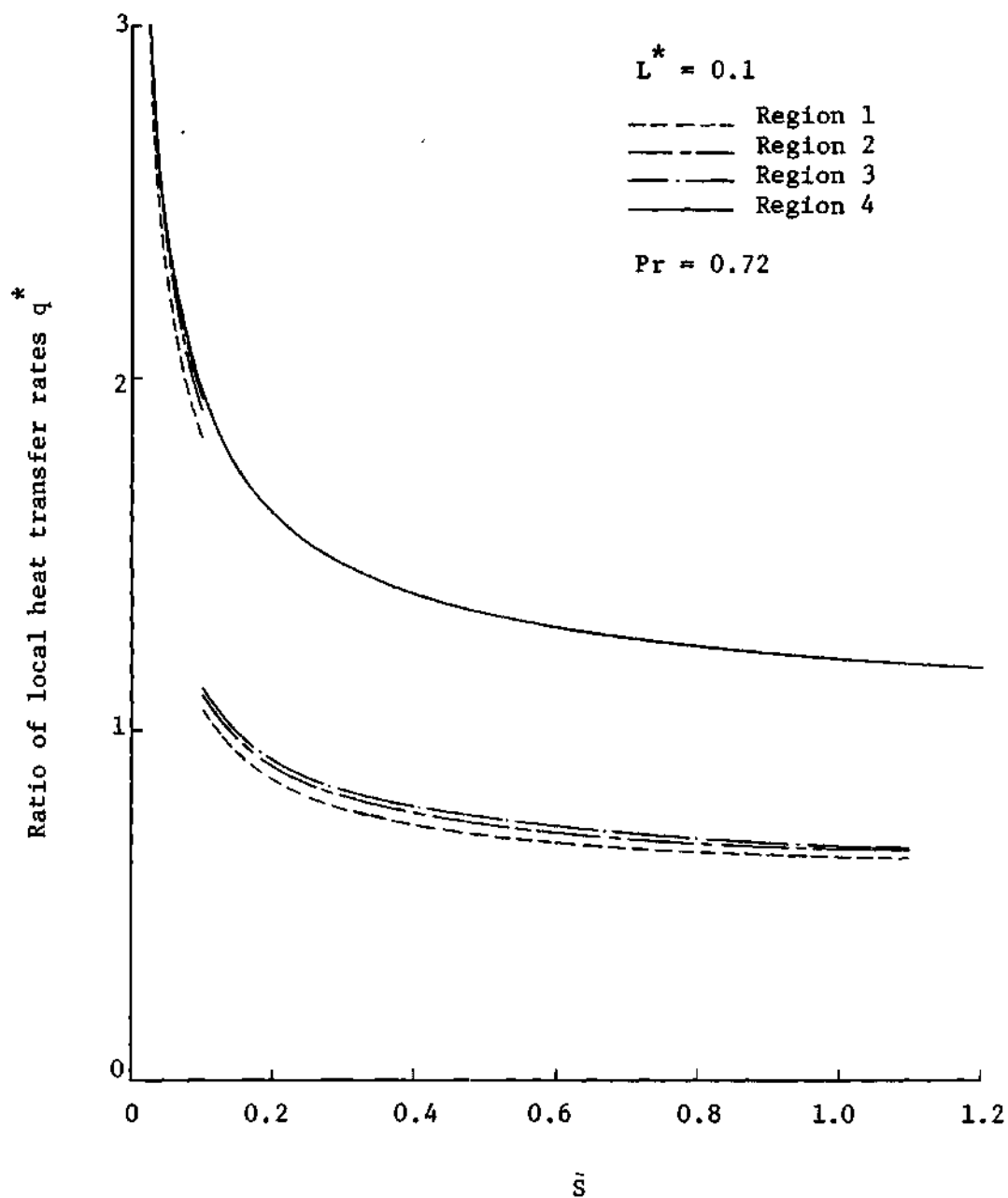


Figure 11. Ratio of Local Heat Transfer Rates Downstream of Reattachment for $L^* = 0.1$.

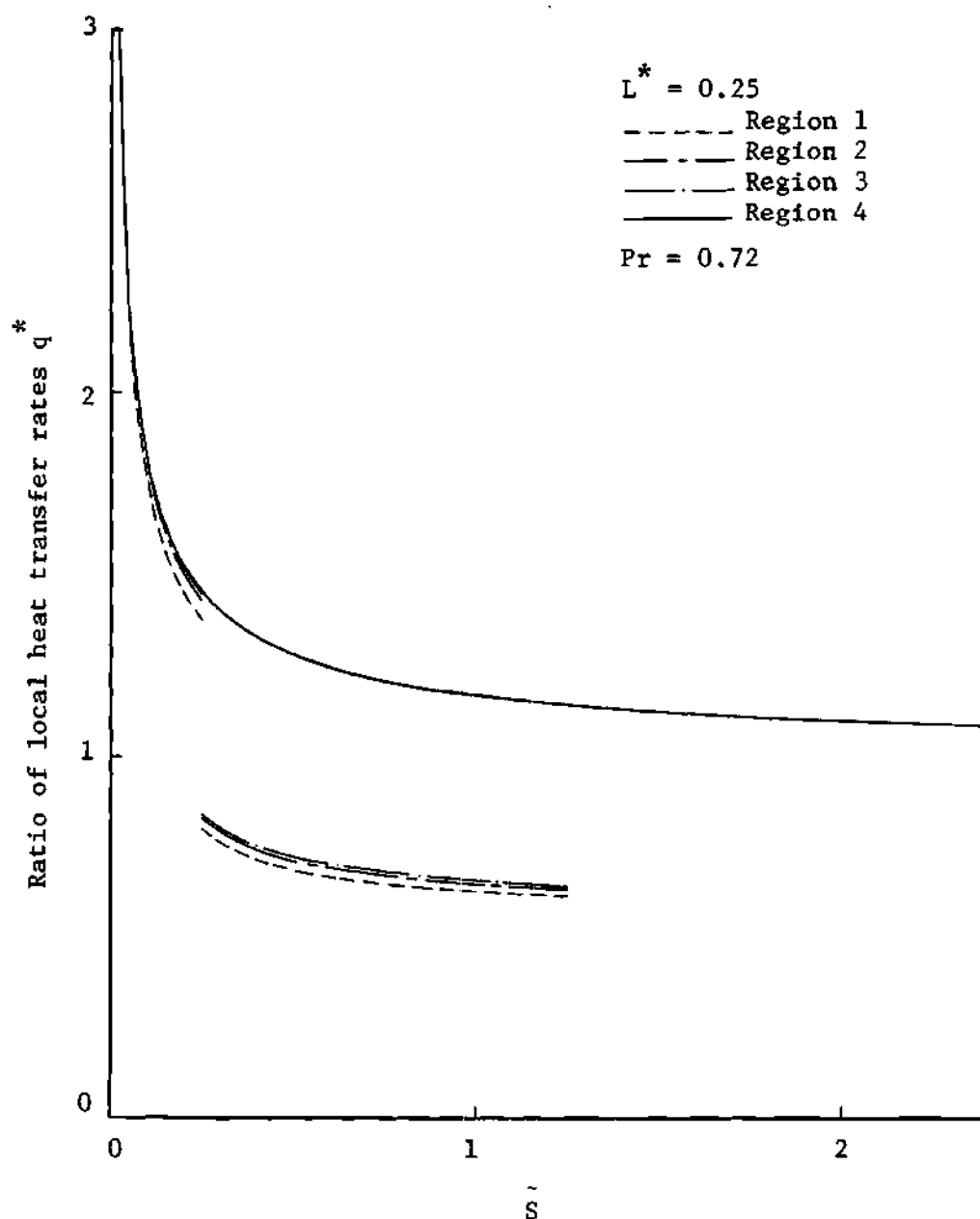


Figure 12. Ratio of Local Heat Transfer Rates Downstream of Reattachment for $L^* = 0.25$.

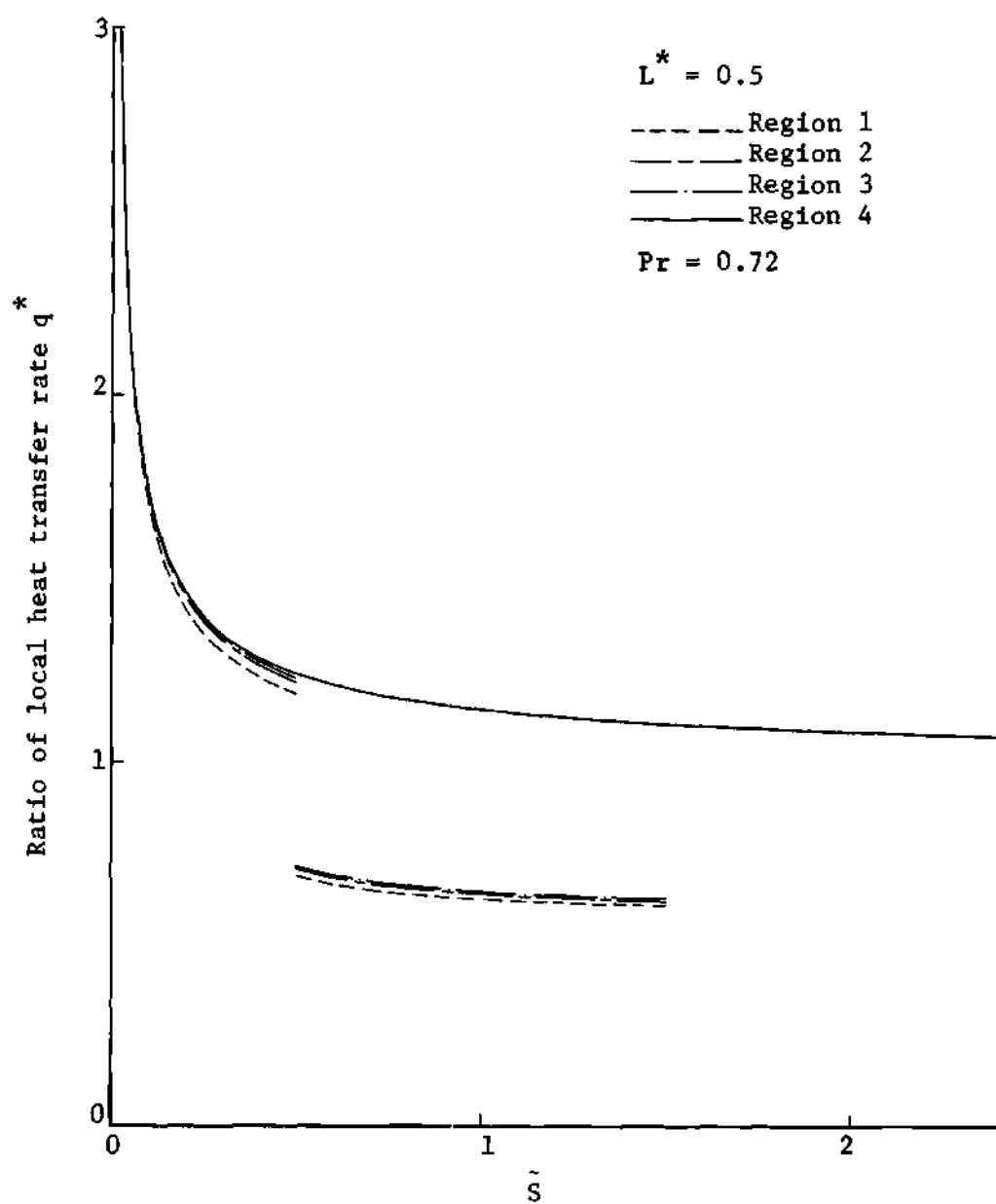


Figure 13. Ratio of Local Heat Transfer Rates Downstream of Reattachment for $L^* = 0.5$.

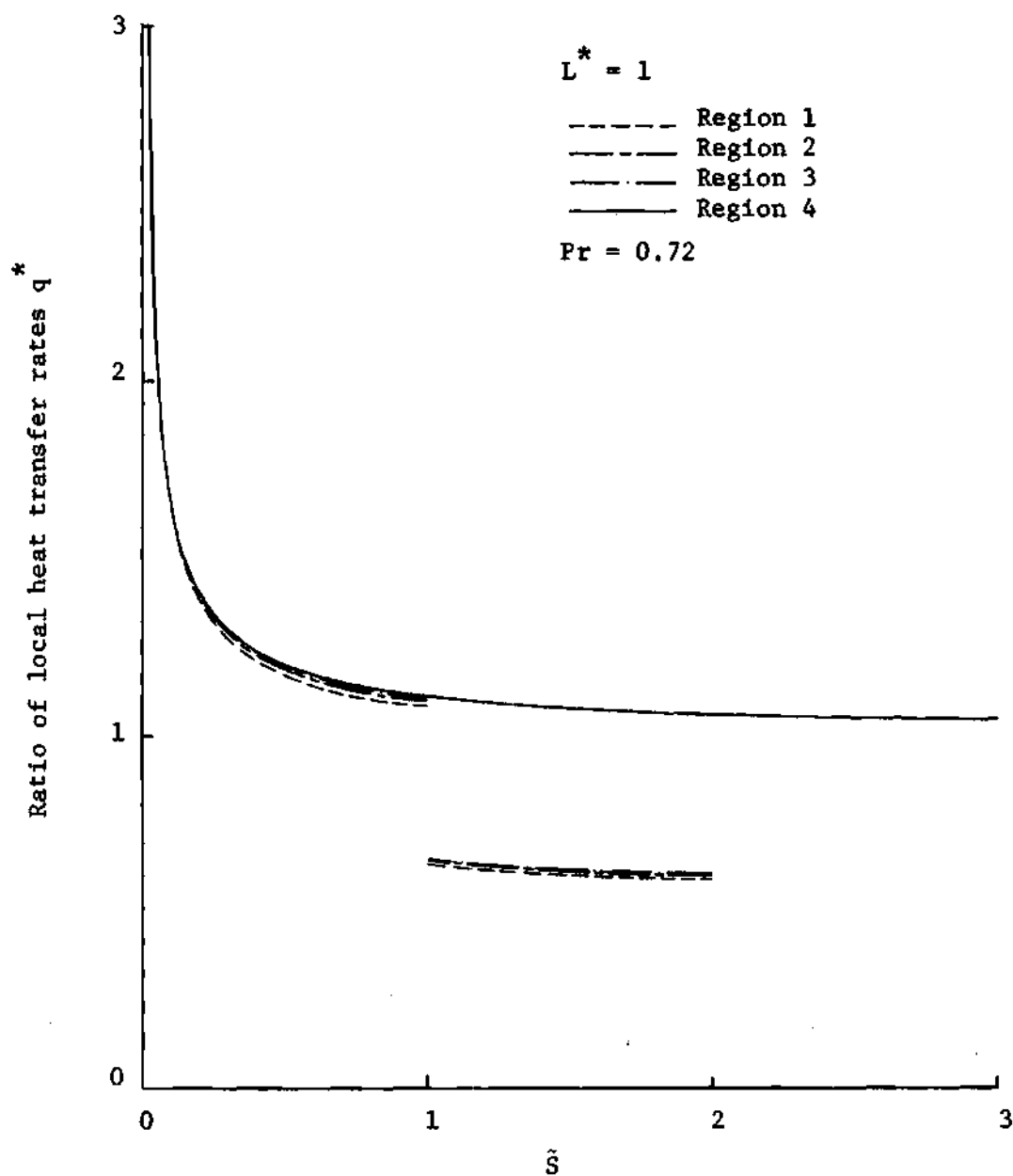


Figure 14. Ratio of Local Heat Transfer Rates Downstream of Reattachment for $L^* = 1$.

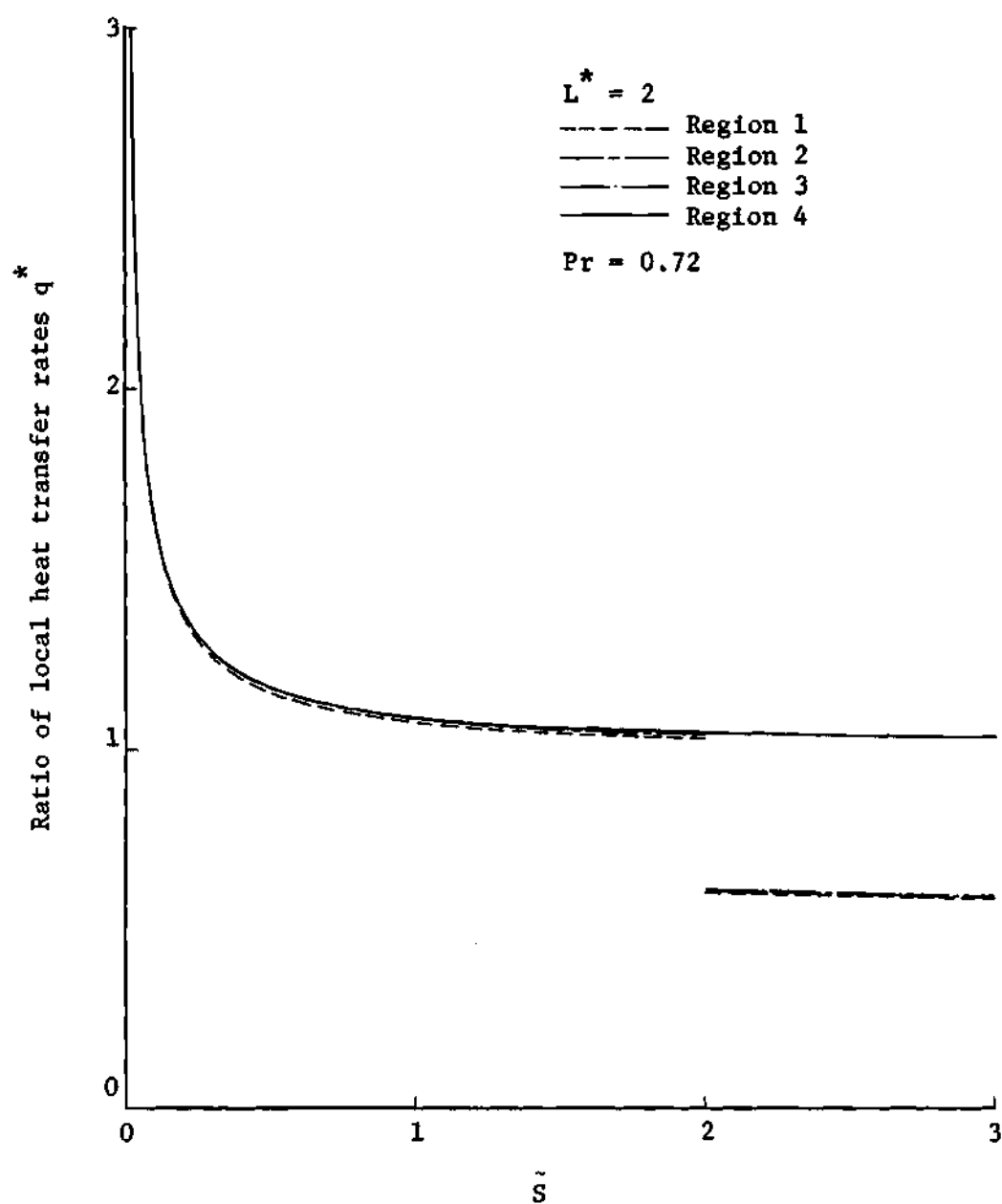


Figure 15. Ratio of Local Heat Transfer Rates Downstream of Reattachment for $L^* = 2$.

tance downstream of each reattachment point divided by the cavity length, as shown in Figure 10. In each case the solution was carried out to large values of \tilde{S} following the fourth cavity.

For each of the geometries considered, the values of q^* for the attached-flow surfaces downstream of reattachment converge to a single curve for the successive regions. The difference between curves is greatest for the region following the first cavity (region 1), while the curves for the subsequent regions converge rapidly with less than one per cent difference for regions 3 and 4. These results show that, for a given value of L^* , a single "correlation" curve of q^* versus \tilde{S} may be used to approximate accurately the local heat transfer rates to the surface downstream of a cavity without necessitating the solution of the boundary layer equations for the entire surface. This approximation is used in the following section to compute the heat transfer rate to the attached-flow regions. In view of the rapid convergence of the results for the succeeding regions, the curves of q^* versus \tilde{S} for region 4 are taken as the correlation curves for each value of L^* . The value of q^* for these correlation curves is denoted by q_{cor}^* . These correlation curves for the various values of L^* are presented in Figure 16. These results show that the local heating rates following reattachment are higher for the smaller values of L^* . This result is attributed to the fact that the free shear layer velocities at reattachment for the smaller cavity spacings are higher and so the gradients at and following reattachment are greater. This is illustrated in Figure 17 where the dividing streamline velocity ratio u_d^* is presented for $L^* = 1, 0.5$, and 0.1 . The values of u_d^* at reattachment are seen to

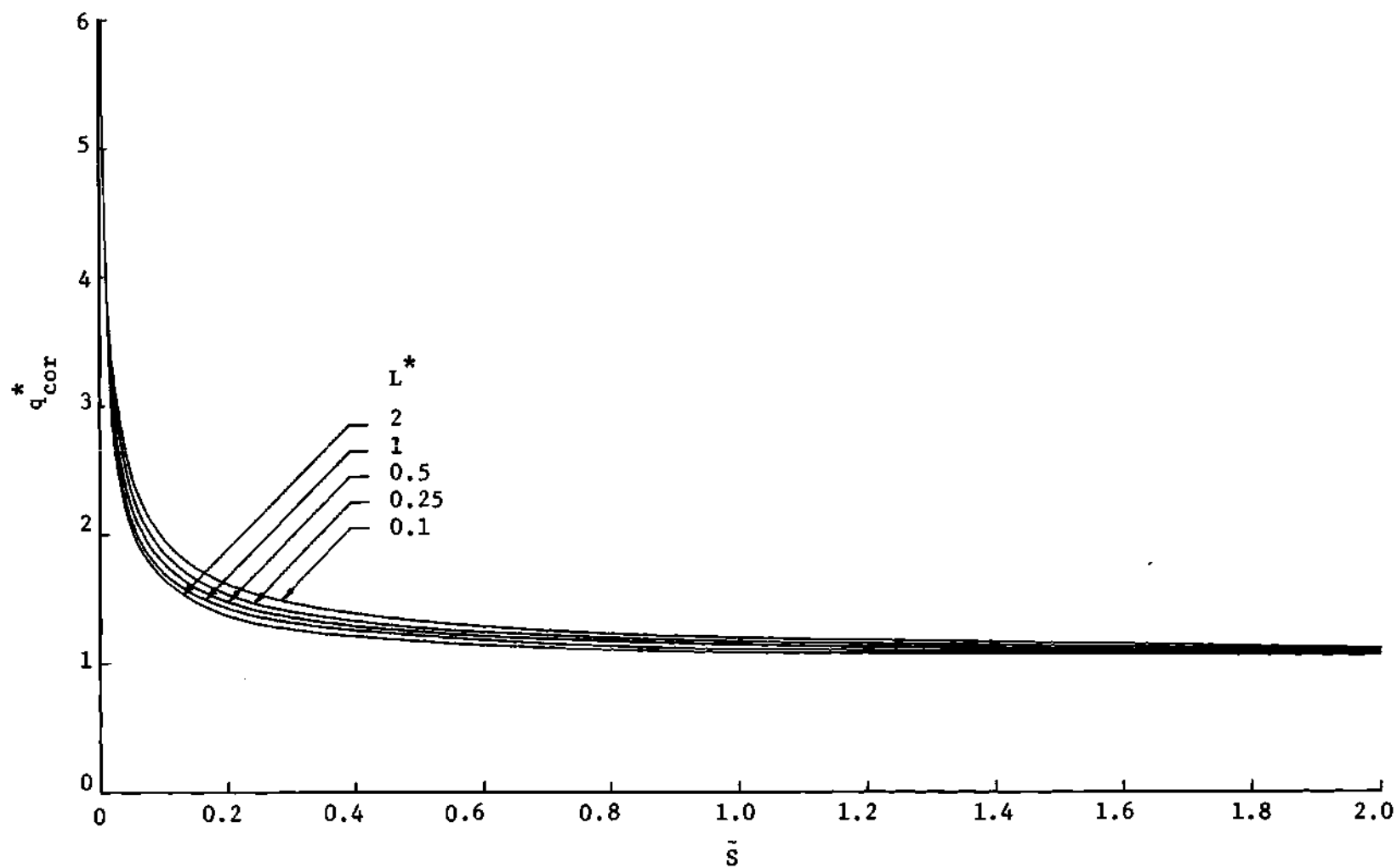


Figure 16. Comparison of the Correlation Curves for Different Values of L^* .

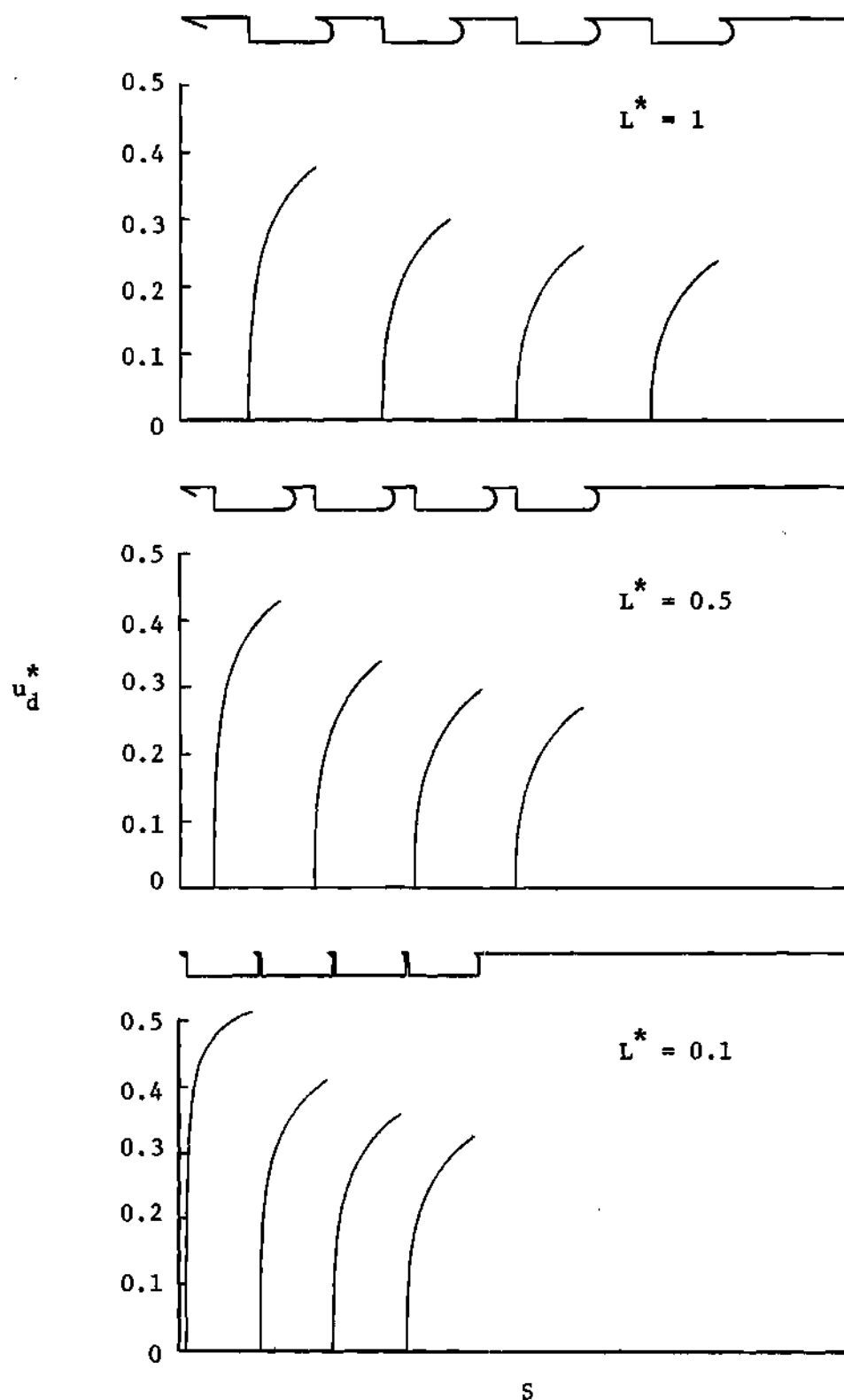


Figure 17. Dividing Streamline Velocity Distribution for Three Multiple-Cavity Configurations.

be greater for decreasing L^* . However, even for small L^* the velocity ratio u_d^* is considerably below 0.587 corresponding to the fully-developed free shear layer profiles. The value of u_d^* at reattachment decreases significantly at successive reattachment points.

The "local" heat transfer rates from the free shear layer solutions for cavities 2, 3, and 4 presented in Figures 11 through 15 also converge to a single curve. In addition, these curves are similar to the corresponding portion of the correlation curve. The similarity between the local heat transfer rates for the free shear layer and the corresponding local heat transfer rates for attached boundary layers was investigated in detail for $L^* = 1$. Solutions for one, two, three, and four cavity configurations were carried out using the finite-difference method. The computed results are presented in Figure 18. The solid lines represent the local heat transfer rates for the four-cavity configuration. The dashed lines over each cavity represent the corresponding heat transfer rates which would exist if the flow were to remain attached. The ratios of these local heat transfer rates in the separated regions to the local heat transfer rates for the corresponding attached flows (i.e., the ratio of the values of the local heat transfer rates for the solid and dashed curves of Figure 18) are presented in Figure 19. This ratio of local heat transfer rates is essentially constant over each cavity and only varies by about one per cent for the various cavities. These results show that, for $Pr = 0.72$, the local heat transfer rate across a free shear layer is between 56 and 57 per cent of that for an attached boundary layer with the same initial profile. Chapman's analysis (2) predicted that the heat transfer rate to

Geometry:

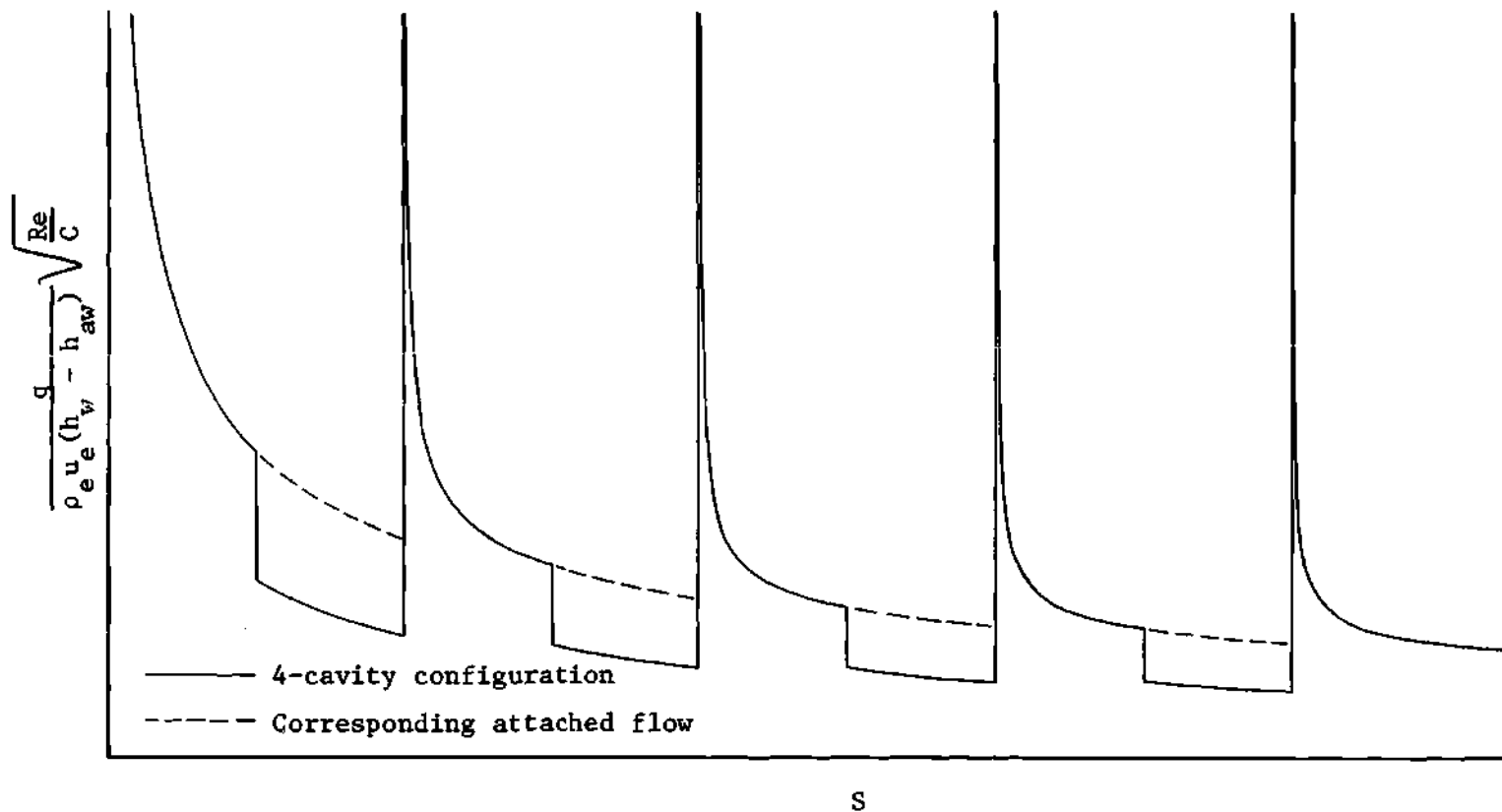
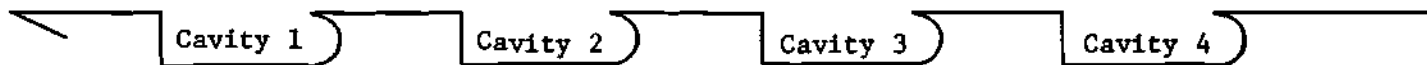


Figure 18. Illustration of Comparison of Local Heat Transfer Rates for Free Shear Layers and Attached Boundary Layers ($L^* = 1$).

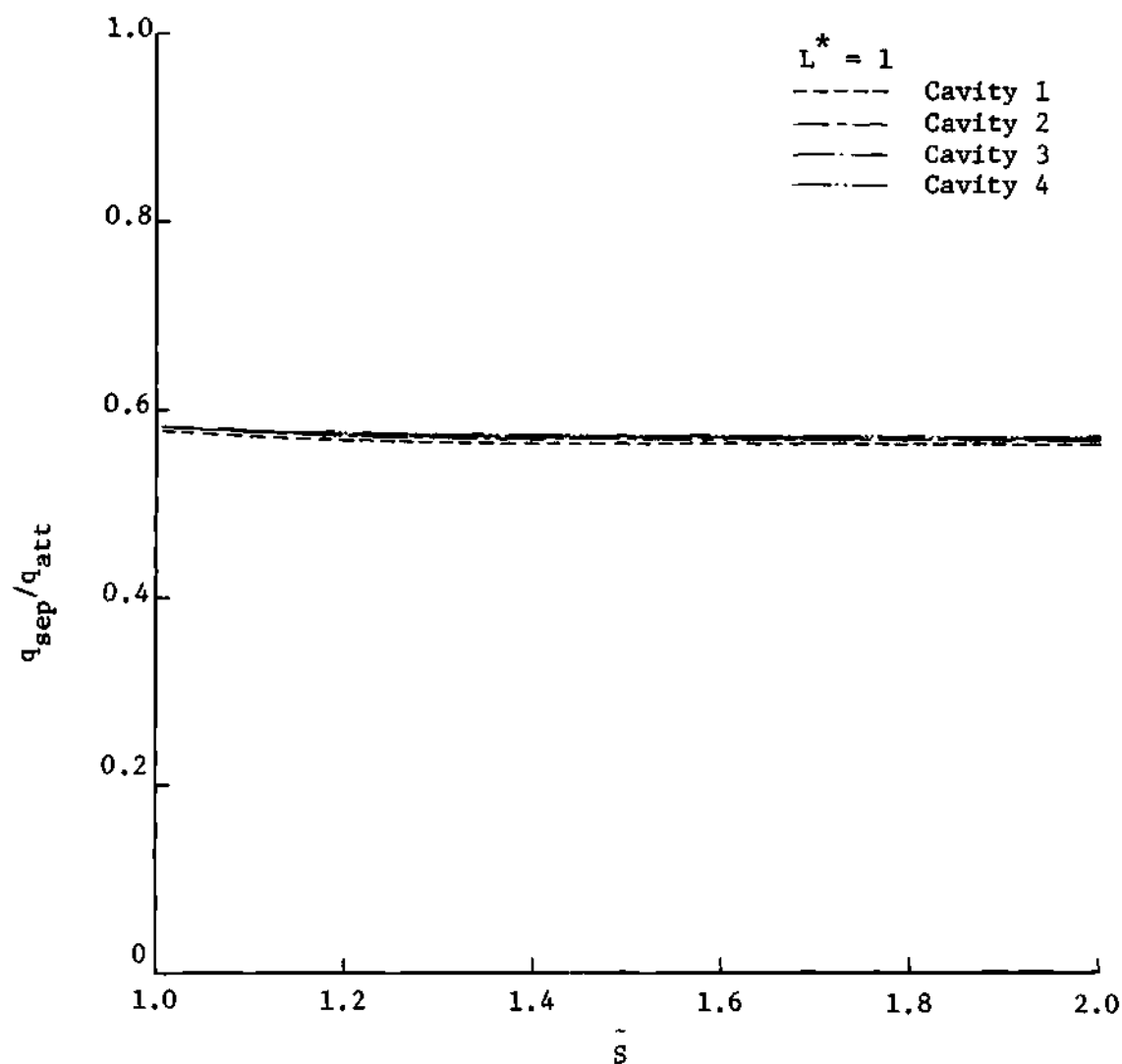


Figure 19. Comparison of Local Heat Transfer Rates for Free Shear Layers and Attached Boundary Layers with the Same Initial Conditions from the Numerical Solution ($Pr = 0.72$).

a separated-flow region for similar profiles was approximately 56 per cent of that to an equivalent attached-flow region for $Pr = 0.72$. These results demonstrate that this ratio is approximately valid for free shear layers with finite initial thicknesses. This probably explains the fact that experiments, which necessarily had finite boundary-layer thicknesses at separation, found good agreement with the heat transfer rates predicted by Chapman.

The local heat transfer rates for the separated-flow regions presented in Figures 11, 12, 13, and 15 for $L^* = 0.1, 0.25, 0.5$, and 2 exhibit the same characteristics as the results for $L^* = 1$. Thus the local heat transfer rate for a free shear layer is equal to approximately 56 per cent of the value for a corresponding attached boundary layer for all values of L^* .

In summary, the results from the numerical solution exhibit the following two characteristics:

1. The local heat transfer rates downstream of reattachment for a given cavity spacing may be correlated with the local heat transfer rates to a completely-attached flow.
2. The local heat transfer rates across a free shear layer with an arbitrary initial profile may be computed to a good approximation by taking 56 per cent of the local heat transfer rates to an attached boundary layer with the same initial profile.

These two characteristics may be utilized to compute rapidly the overall heat transfer rate to a multiple-cavity configuration. The local heat transfer rates for an attached boundary layer may be calculated using

the correlation curves presented in Figure 16. The local heat transfer rates for the free shear layers may be approximated by taking 56 per cent of the corresponding value from these correlation curves. This method, hereafter termed the "correlation technique," is developed and used in the next section.

Heat Transfer Results Using the Correlation Technique

The correlation technique developed in this section is used to compare the heat transfer rate to that portion of the surface downstream of the initial attached-flow region (i.e., downstream of $S = L_s$) to the heat transfer rate to the corresponding portion of a flat plate with completely-attached flow. Using $q = q^* q_{b1}$ and substituting for q_{b1} from equation (51), the average heat transfer rate \bar{q} to this portion of the surface may be written

$$\frac{\bar{q}}{\rho_e u_e (h_w - h_{aw})} \sqrt{\frac{Re}{C}} = \frac{0.29575}{Pr} \int_{L_s}^S \frac{q^*}{\sqrt{S}} dS \quad (60)$$

Using this relation and substituting for \bar{q}_{b1} from equation (52), equation (58) becomes

$$\bar{q}^* = \frac{1}{2(\sqrt{S} - \sqrt{L_s})} \int_{L_s}^S \frac{q^*}{\sqrt{S}} dS \quad (61)$$

Let \bar{S} be the distance downstream of the initial attached-flow region divided by the cavity length as illustrated in Figure 8, i.e.,

$$\bar{S} = \frac{S - L_s}{L}$$

Then, substituting this expression into equation (61) and using an initial attached-flow length $L_s = L_a$ yields

$$\bar{q}^* = \frac{1}{2 \left(\sqrt{\bar{S} + L^*} - \sqrt{L^*} \right)} \int_0^{\bar{S}} \frac{q^*}{\sqrt{\bar{S} + L^*}} d\bar{S} \quad (62)$$

For the first cavity (i.e., $0 \leq \bar{S} \leq 1$), the value of q^* as given by the correlation is 0.56, so that for $\bar{S} \geq 1$, equation (62) becomes

$$\bar{q}^* = \frac{2(0.56) \left[\sqrt{1 + L^*} - \sqrt{L^*} \right] + \int_1^{\bar{S}} \frac{q^*}{\sqrt{\bar{S} + L^*}} d\bar{S}}{2 \left(\sqrt{\bar{S} + L^*} - \sqrt{L^*} \right)} \quad (63)$$

Define β by

$$\beta = \frac{q^*}{q_{cor}^*}$$

where the values of β used in the correlation technique are

$$\beta = \begin{cases} 1 & \text{for attached boundary layers} \\ 0.56 & \text{for free shear layers} \end{cases}$$

Equation (63) then becomes

$$\bar{q}^* = \frac{2(0.56) \left[\sqrt{1 + L^*} - \sqrt{L^*} \right] + \int_1^{\bar{S}} \frac{\beta q_{\text{cor}}^*}{\sqrt{\bar{S} + L^*}} d\bar{S}}{2 \left(\sqrt{\bar{S} + L^*} - \sqrt{L^*} \right)} \quad (64)$$

where q_{cor}^* is given for each value of L^* by Figure 16.

To investigate the accuracy of the correlation technique, equation (64) was used to compute the overall heat transfer rates for one, two, three, and four-cavity configurations for a value of $L^* = 1$. These results are presented in Figure 20. Results from the finite-difference solution method for the same configurations are presented for comparison. The correlation technique over-estimates the heat transfer. This conservative feature of the correlation technique may be explained by reviewing the local heat transfer rates in Figure 14. The correlation technique uses the curve for region 4 as the correlation curve. Since this curve lies above the curves for regions 1, 2, and 3, the overall heat transfer rate computed from the correlation curve for these regions is high. Since the difference between the correlation curve and the actual curve is greatest for region 1 (i.e., following the first cavity), the results for the overall heat transfer rate for the one-cavity configuration in Figure 20 shows the greatest difference for the two methods. The agreement between the results for the two methods improves as the number of cavities increases. The results for the four-cavity configuration are only about one per cent higher than the results from the numerical solution. Thus, for multiple-cavity configurations, the correlation technique furnishes overall heat transfer rates in good agreement with the numerical results with much less

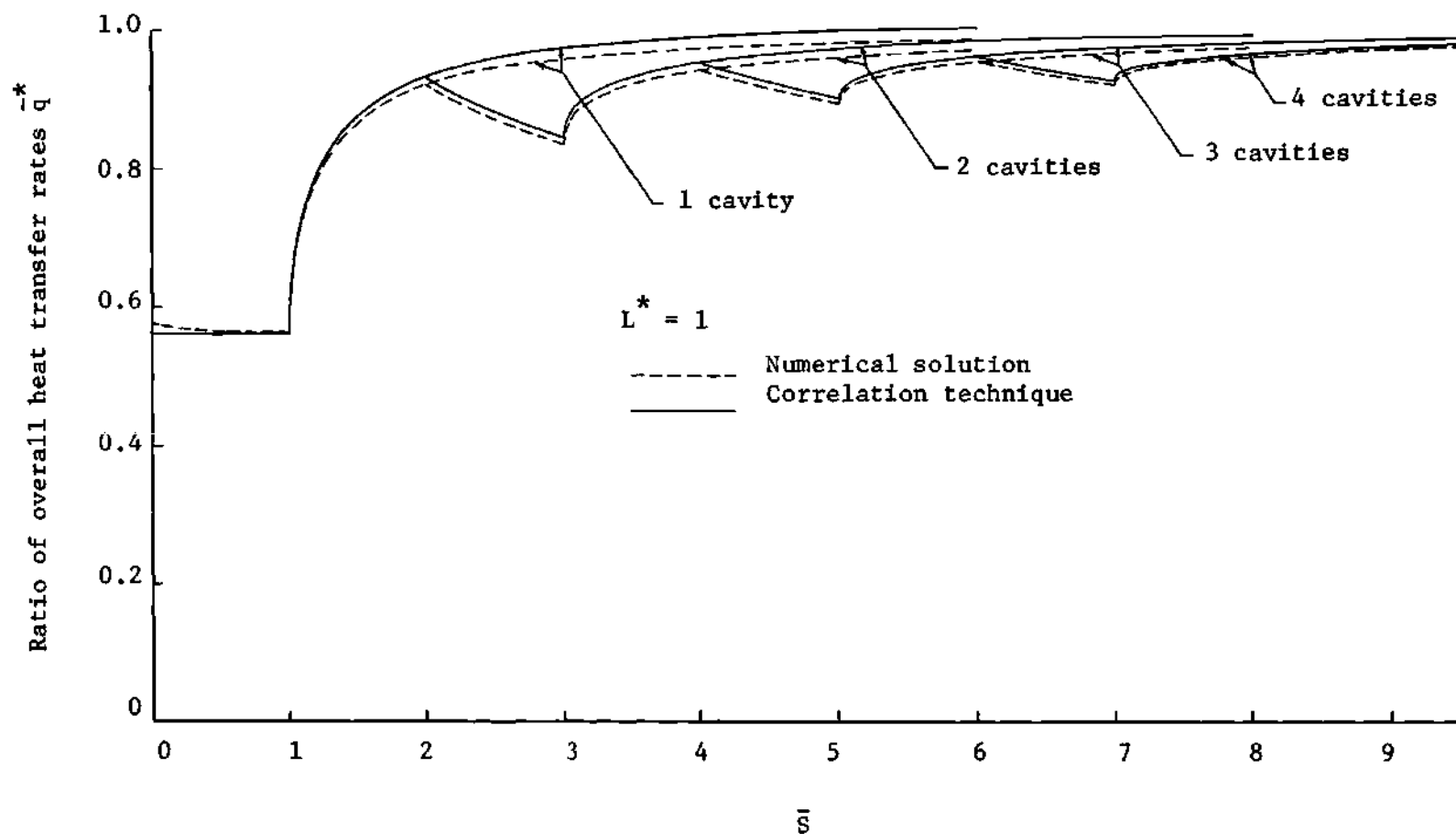


Figure 20. Comparison of Overall Heat Transfer Results from the Correlation Technique with Results from the Numerical Solution for $L^* = 1$ ($Pr = 0.72$).

computational effort.

The correlation technique was employed to compute the overall heat transfer rate to a surface with four cavities for various cavity spacings. The results of these computations for $L^* = 0.1, 0.25, 0.5,$ and 1 are shown in Figures 21 through 24. The results show the effects of both multiple cavities and cavity spacing on the overall heat transfer rates.

The results in Figures 21 through 24 show that the overall heat transfer rate downstream of the first cavity is reduced by subsequent cavities. For example, from Figure 24 ($L^* = 1$) the ratio of overall heat transfer rate \bar{q}^* for the two-cavity configuration at the end of the second cavity (i.e., $\bar{S} = 3$) is 0.845. The value of \bar{q}^* for the one-cavity configuration at the same point ($\bar{S} = 3$) is 0.972. Hence, the reduction in overall heat transfer rate (i.e., $1 - \bar{q}^*$) at $\bar{S} = 3$ is 15.5 per cent for the two-cavity configuration as compared to 2.8 per cent for the one-cavity geometry. The effect of the successive cavities is smaller but still results in a reduction in overall heat transfer rate when compared to a geometry with fewer cavities. Similar results are obtained for the other values of L^* , with the reduction due to multiple cavities increasing as L^* decreases.

The advantage of multiple-cavity configurations diminishes when the attached-flow region downstream of the last cavity is extensive. Thus, in a practical application, extensive attached-flow regions downstream of the last cavity are to be avoided, and the end of the surface should be just downstream of the final cavity. With this in mind, the values of \bar{q}^* of significance are the values at the end of each of the

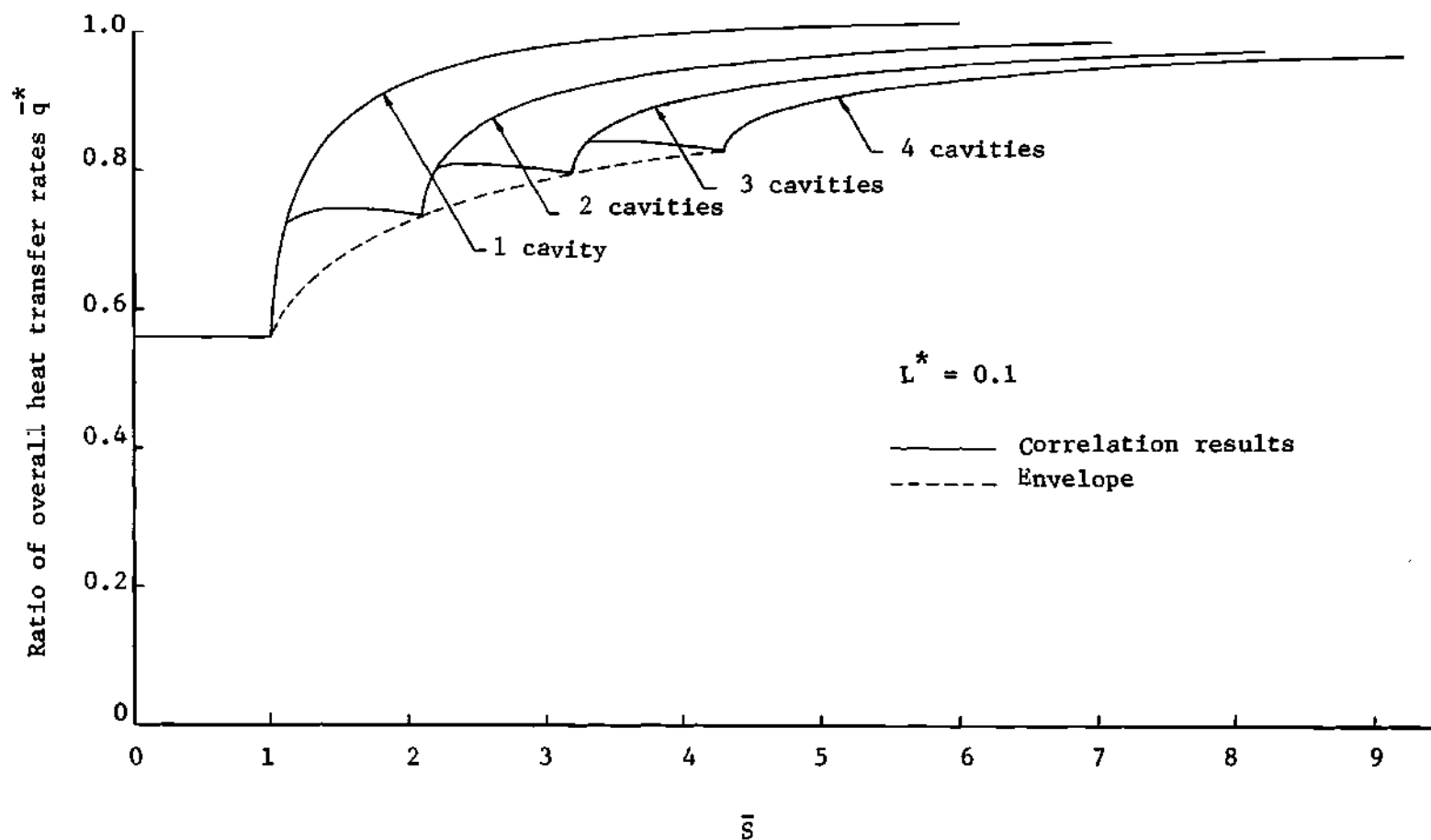


Figure 21. Ratio of Overall Heat Transfer Rates from the Correlation Technique for $L^* = 0.1$ ($Pr = 0.72$).

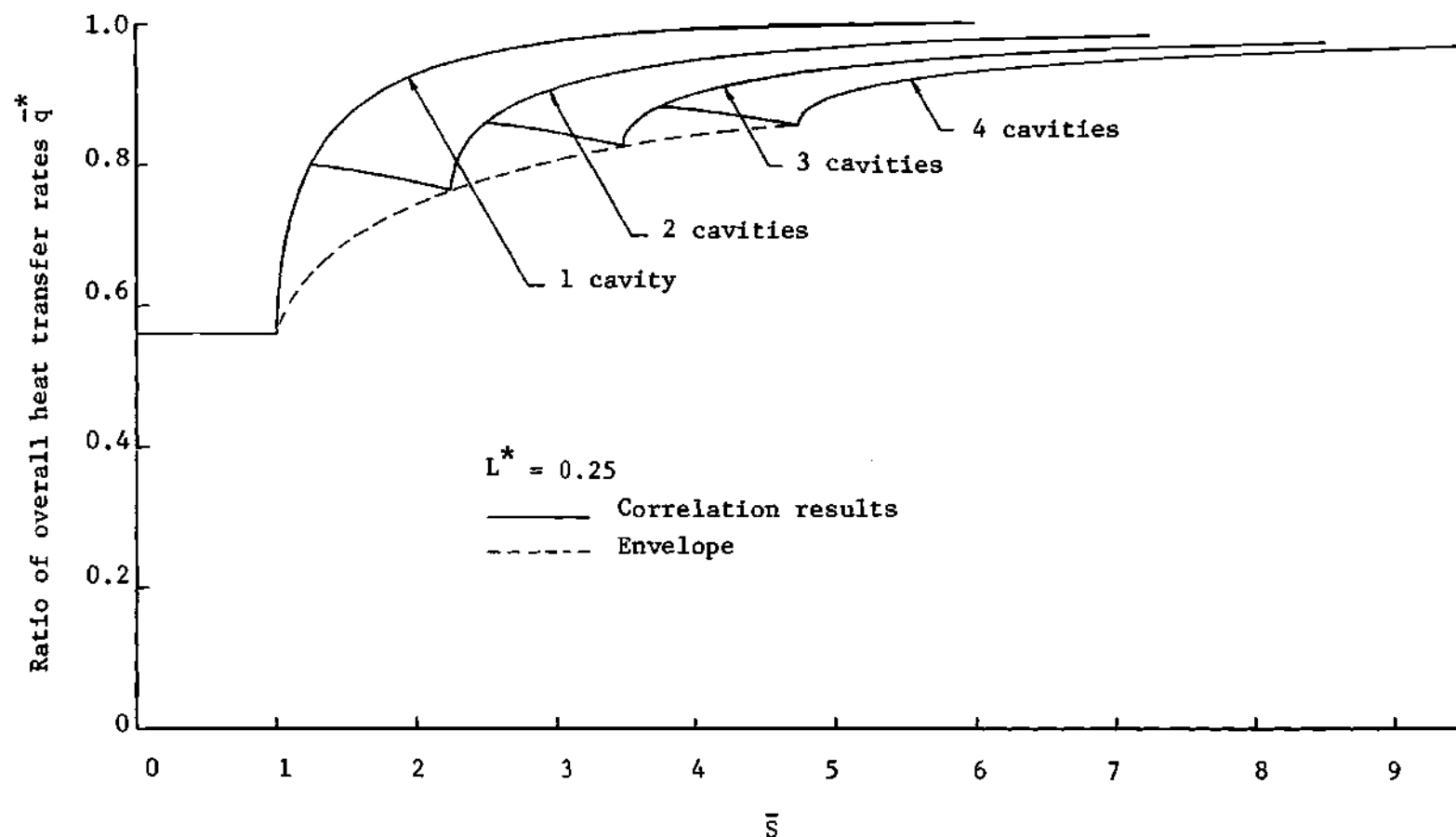


Figure 22. Ratio of Overall Heat Transfer Rates from the Correlation Technique for $L^* = 0.25$ ($Pr = 0.72$).

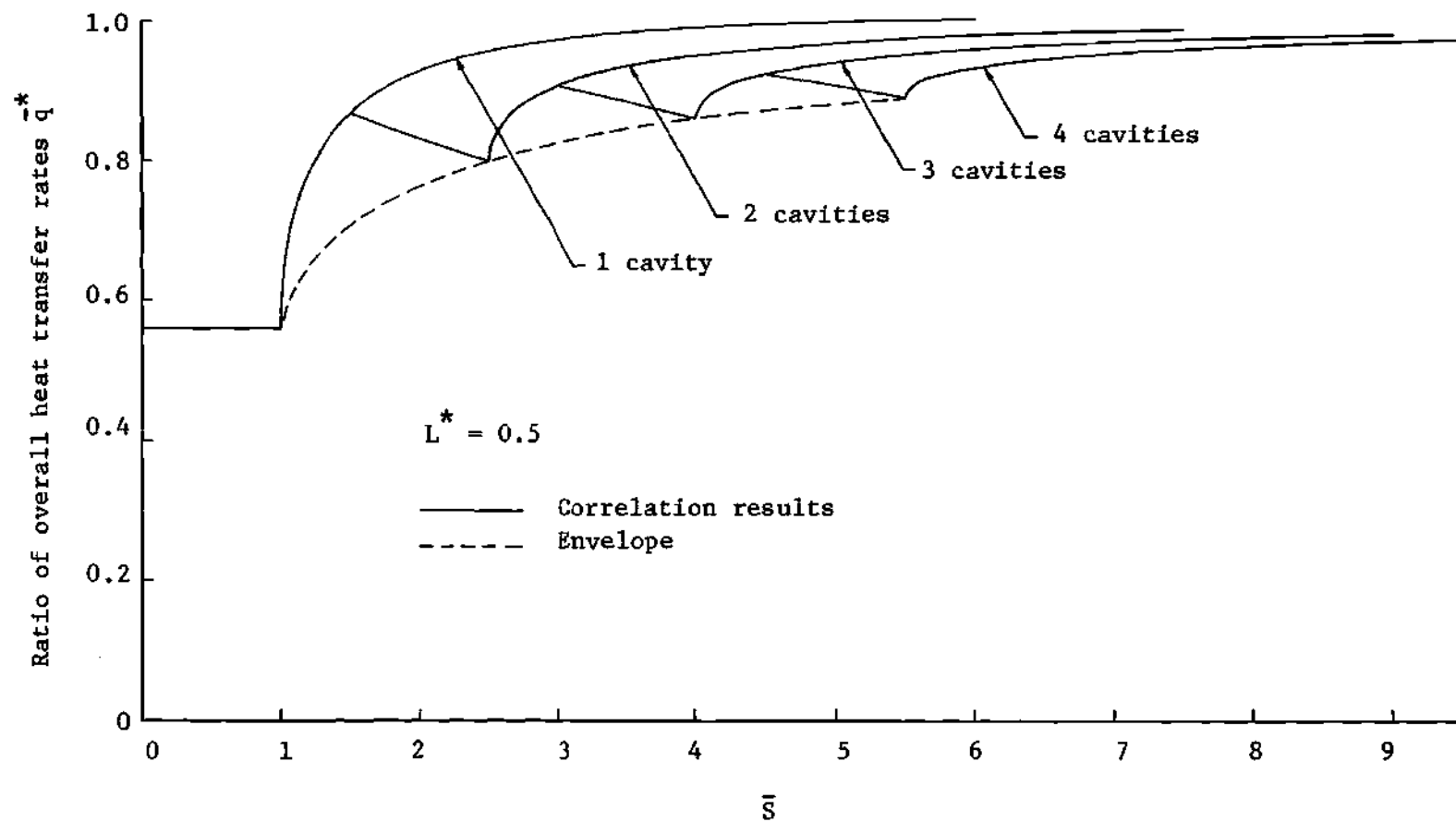


Figure 23. Ratio of Overall Heat Transfer Rates from the Correlation Technique for $L^* = 0.5$ ($Pr = 0.72$).

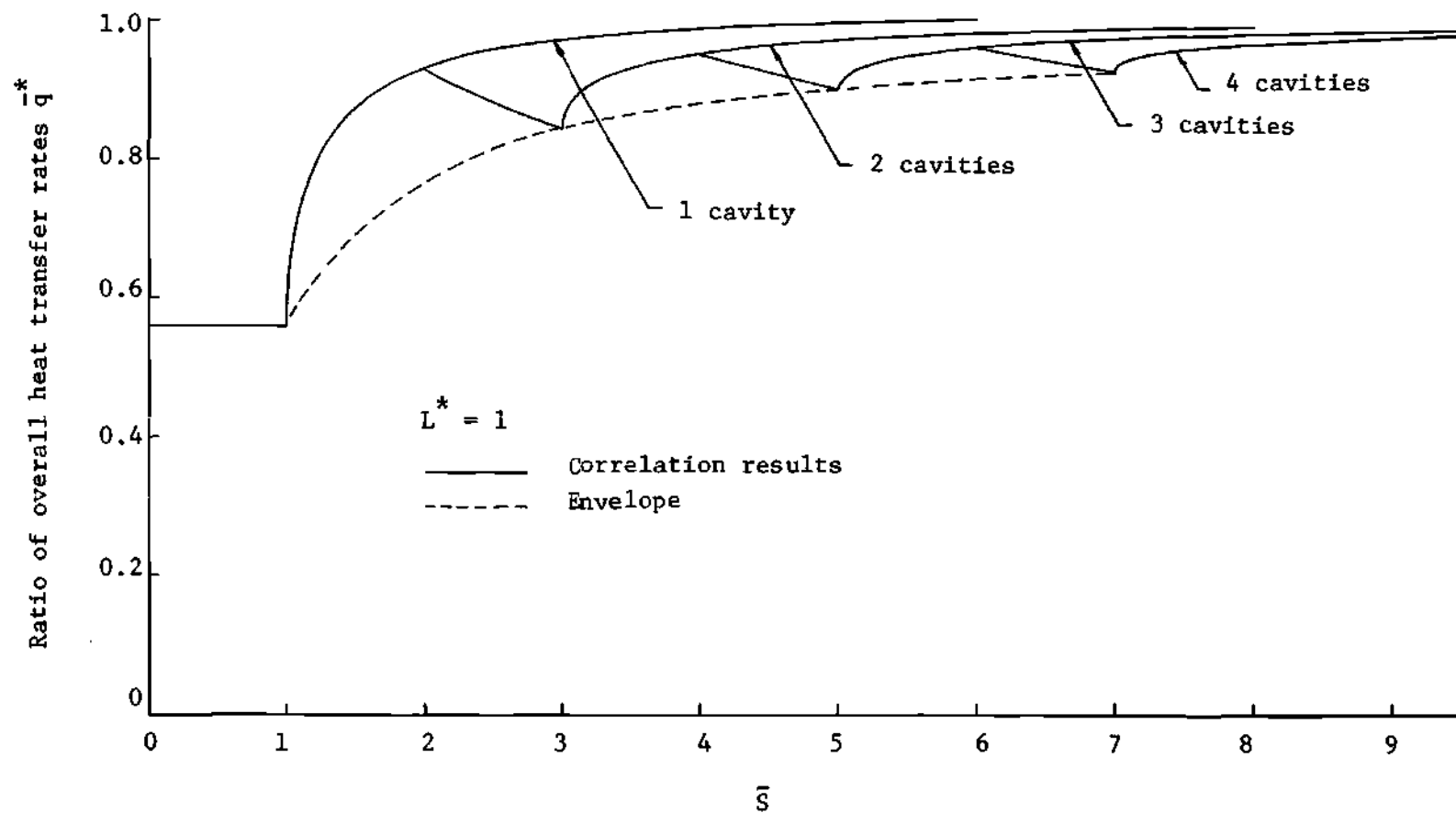


Figure 24. Ratio of Overall Heat Transfer Rates from the Correlation Technique for $L^* = 1$ ($Pr = 0.72$).

cavities. These values represent the maximum reduction in the heat transfer rate attainable employing the present geometry. The dashed lines in Figures 21 through 24 represent the envelope of these values of \bar{q}^* .

To illustrate the effects of cavity spacing for multiple-cavity geometries, the correlation technique was employed to compute the value of \bar{q}^* at the end of each cavity for a multiple-cavity configuration for $L^* = 0.1, 0.25, 0.5, 1$, and 2 . The results of these computations are presented in Figure 25. Each solid line represents the results for a given number of cavities. The dashed lines represent the envelope of the values of \bar{q}^* for a given value of L^* , as shown in Figures 21 through 24. These results demonstrate the effect of both cavity spacing and the number of cavities. The smaller values of L^* , corresponding to larger ratios of separated to attached-flow areas, result in larger reductions in \bar{q}^* . The reduction in \bar{q}^* is not directly proportional to the area ratio, however, due to the higher local heat transfer rates to the attached-flow regions for smaller L^* . The smaller values of \bar{q}^* occur for small \bar{S} . Thus, if cavity-induced separated-flow regions are used to reduce the overall heat transfer rate to a given surface, the corresponding value of \bar{S} should be made as small as practicable. Since \bar{S} depends upon the cavity length, this requires that the cavities be as long as possible, keeping in mind that the cavity flows must be of the deep, open type.

For a specified cavity length (i.e., given \bar{S}), the results in Figure 25 show that the minimum value of \bar{q}^* occurs for the larger number of cavities (i.e., smaller L^*). For example, for a value of $\bar{S} = 8$,

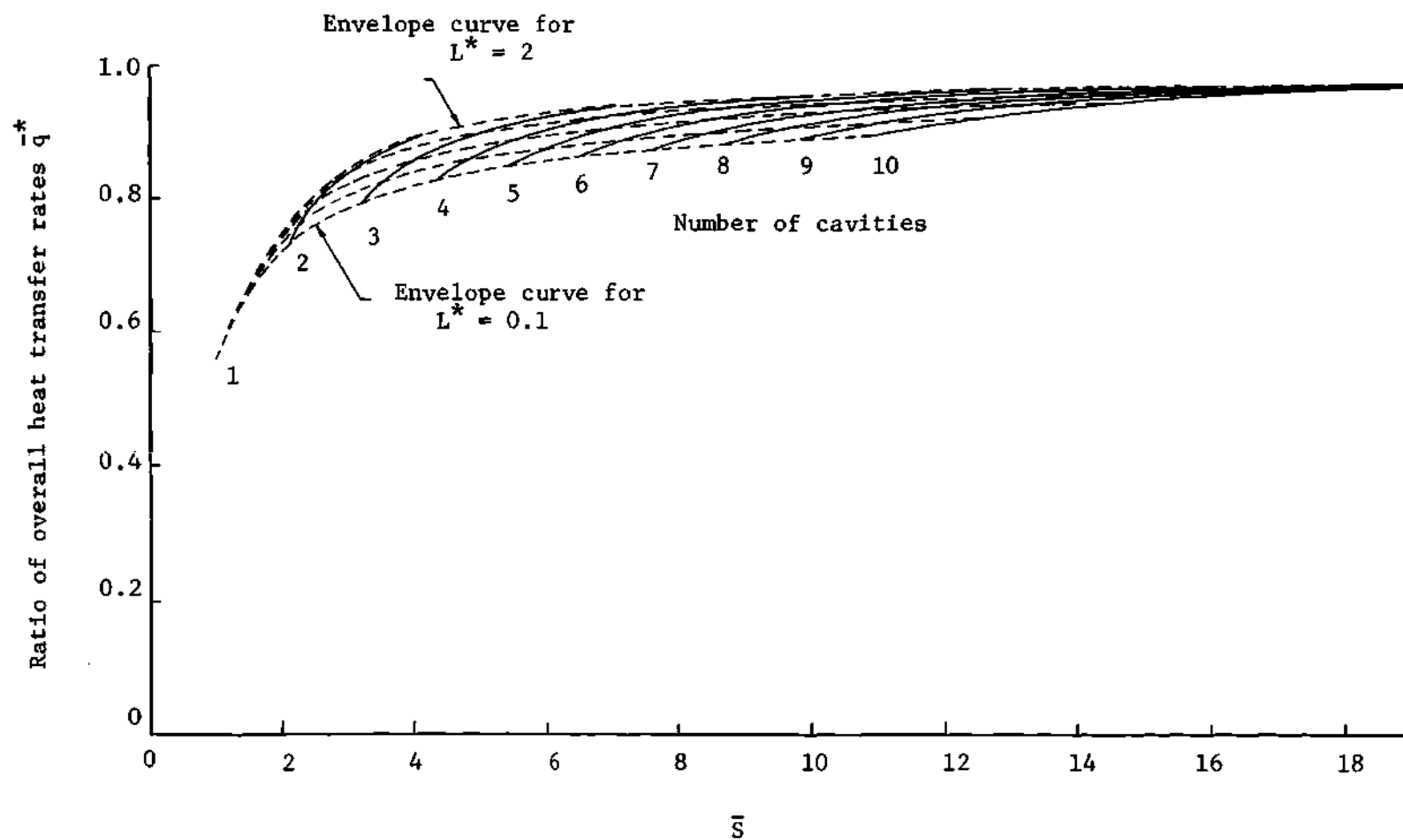


Figure 25. The Effect of Number of Cavities and Cavity Spacing on the Overall Heat Transfer Using the Correlation Technique ($Pr = 0.72$).

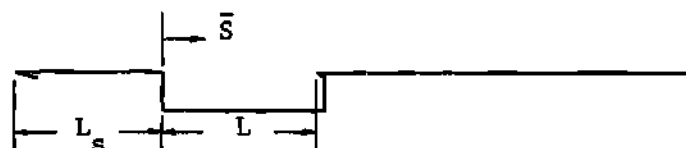
these results predict the smallest value of \bar{q}^* to be approximately 0.87 for a seven-cavity configuration. The corresponding cavity spacing L^* is between 0.1 and 0.25.

In summary, the results from the correlation technique demonstrate that, with the present sharp-cusp reattachment geometry, surfaces with multiple cavity-induced separated-flow regions experience a substantial reduction in overall heat transfer rate. However, this reduction is perhaps disappointing in comparison with the reduction potential available in a completely-separated flow. Comparison with results from the numerical solution show that the correlation technique provides overall heat transfer rates that are slightly conservative. For a given surface length, the maximum reduction in heat transfer rate occurs when the cavities are as long as possible and the cavity spacing is chosen so that the largest number of cavities are used while keeping the length of the attached-flow region following the last cavity as short as possible.

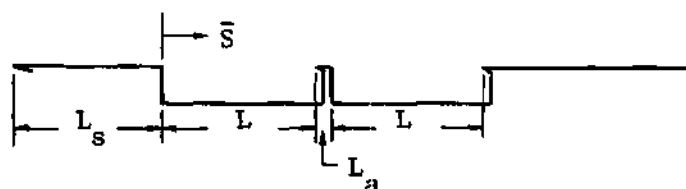
Effects of Initial Attached-Flow Length

All of the results presented thus far have used an initial attached-flow length L_s which is equal to the length of the attached-flow regions between the cavities L_a . To investigate the effect of a different initial length L_s , the numerical solution procedure was applied to the geometries depicted in Figure 26. Two cases were considered, namely, $L_s = L_a$ and $L_s = L$, and for each case a value $L^* = 0.1$ was used. Both one- and two-cavity configurations were employed. The overall heat transfer rates to the portion of the surface downstream of $\bar{S} = 0$ are

One-cavity configuration:



Two-cavity configuration:

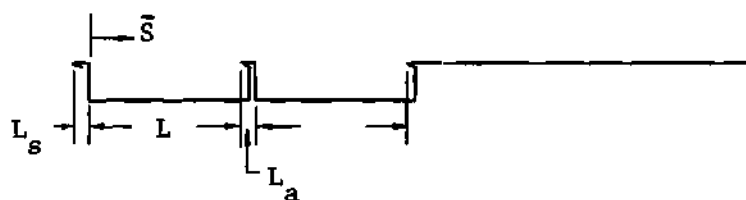


(a) Case 1: $L_s = L$, $L^* = 0.1$.

One-cavity configuration:



Two-cavity configuration:



(b) Case 2: $L_s = L_a$, $L^* = 0.1$.

Figure 26. Illustration of the Two Cases Considered for the Initial Attached-Flow Length.

presented in Figure 27.

The lower values for \bar{q}^* downstream of the cavities for Case 2 ($L_s = L_a$) are attributed to the fact that the cavities are located nearer the leading edge and thus in a region where the attached-flow local heat transfer rates are higher. Since the local heat transfer rates for the free shear layer are 56 per cent of the equivalent attached boundary layer values, the cavities located nearer the leading edge reduce the local attached-flow heat transfer rates where they are higher, resulting in a greater reduction in the overall heat transfer rate. However, the results in Figure 27 show that the values of \bar{q}^* at the end of each of the cavities varies only slightly for different initial attached-flow lengths. The effect of the initial length will continue to diminish with additional cavities.

Effect of Blunted-Cusp Reattachment Geometry

Since a sharp-cusp reattachment geometry would generally be impractical, an analysis was made to explore the effect that cusp leading-edge bluntness would have on the heat transfer results of the present analysis. This effect was explored by comparing the heat transfer rate to a blunted flat plate with that to a sharp-edge flat plate. The details of this study are presented in Appendix D, and the results are summarized here. The analysis of Appendix D assumes that the leading-edge thickness is small compared with the free shear layer thickness at reattachment (i.e., the flow is essentially uniform over a height equal to the leading-edge thickness), and that the leading-edge effects downstream of the nose are equivalent to those for the flat plate. This

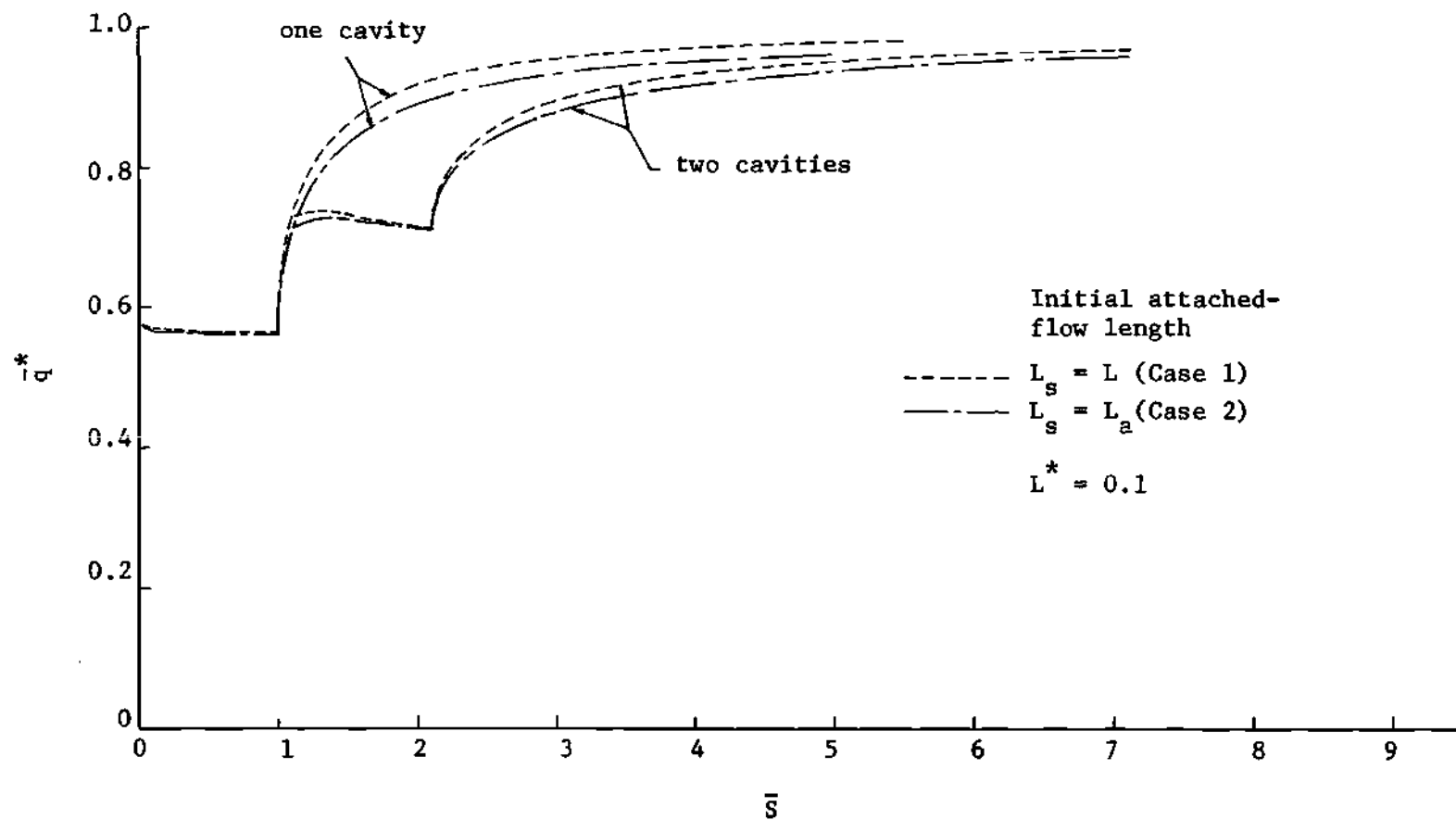


Figure 27. Comparison of Overall Heat Transfer Rates for Two Initial Attached-Flow Lengths ($Pr = 0.72$).

blunted-cusp reattachment geometry is illustrated in Figure 2(d).

The calculations for a perfect gas with $Pr = 1$ and cold-wall conditions demonstrate that the Mach number of the flow approaching reattachment (i.e., the Mach number at the dividing streamline) ranges from zero to about three for freestream Mach numbers ranging from zero to infinity. For the values of the dividing streamline velocities encountered in the present results, a representative Mach number for the flow approaching reattachment is approximately 1.8.

Employing the blunt body theory of reference (24) for a reattachment Mach number of approximately 1.8, the overall heat transfer rate to the nose of a blunted flat plate is approximately 25 per cent greater than that to a sharp-edged flat plate with the same surface length. This increases to only about 50 per cent in the limiting case of a fully-developed free shear layer at reattachment (i.e., $u_d^* = 0.587$) and a freestream Mach number approaching infinity.

The effect of the degree of bluntness (i.e., the ratio of leading-edge diameter to the length of the plate) on the overall heat transfer rate is estimated using the heat transfer rates for the blunt nose as obtained from the blunt body theory. The heat transfer rates for that portion of the blunt plate downstream of the nose are determined using an equivalent flat plate downstream of the blunt nose. The results of this analysis demonstrate that, for the typical reattachment Mach number of 1.8, a blunt plate with a ratio of nose thickness to plate length of 0.1 would have an overall heat transfer rate only about three per cent greater than a sharp-edged flat plate of the same length. Approximately a six per cent increase would occur for the limiting case of a

fully-developed free shear layer with $M_e \rightarrow \infty$.

Another indication of the small effect of bluntness is illustrated by the experimental values of the ratio of local heat transfer rates q^* downstream of reattachment measured by Nicoll (9). These results are presented in Figure 28. The geometries employed in the experiment were single-cavity configurations with initial attached-flow regions twice the cavity length (i.e., $\frac{L_s}{L} = 2$). The cavities employed shoulder reattachment geometries like those depicted in Figure 2(a). The correlation curve for $L^* = 2$ from the present results for a sharp-cusp reattachment geometry is presented for comparison. In view of the difference in the reattachment geometries, the agreement is surprising.

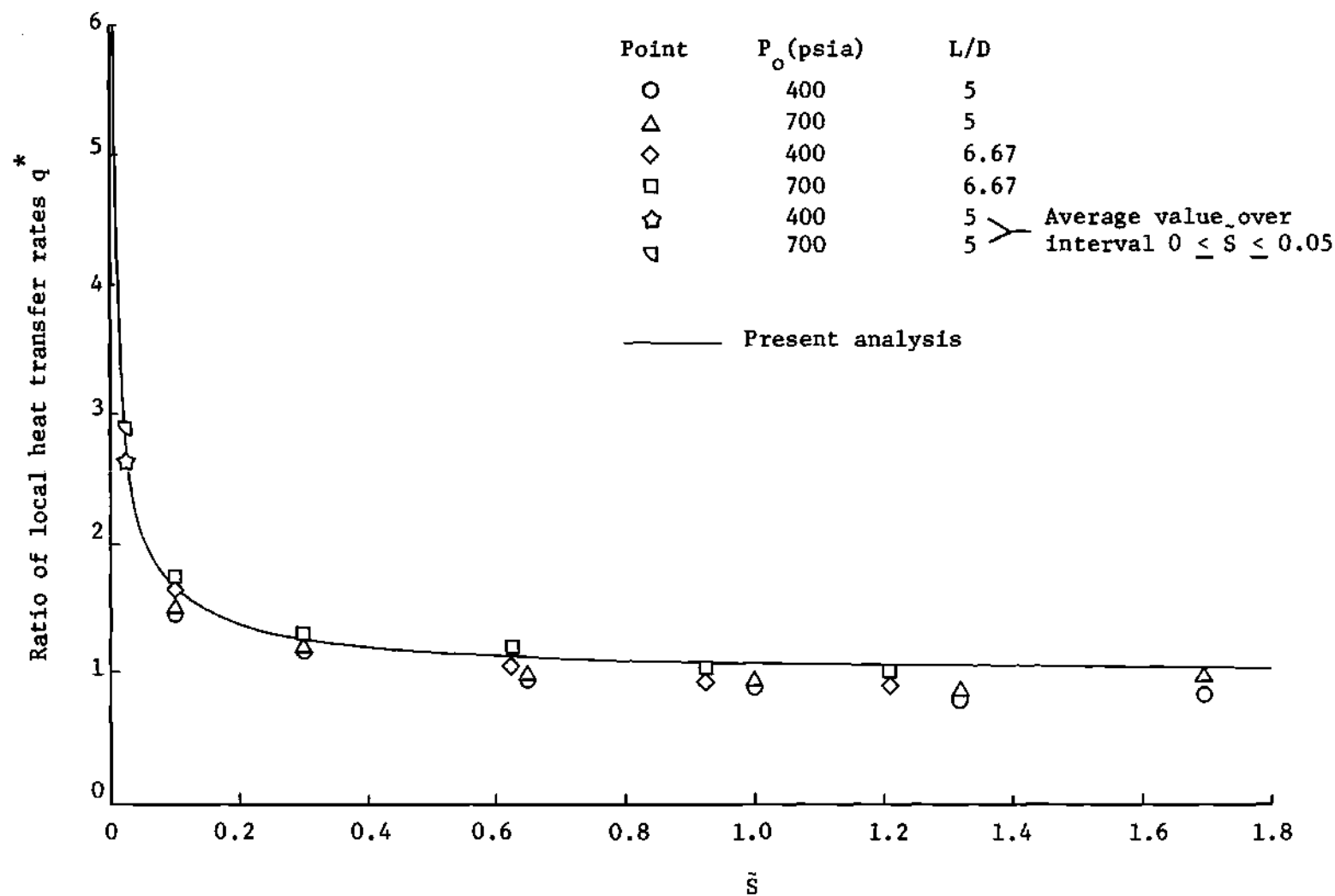


Figure 28. Comparison of Experimental Local Heat Transfer Rates from Reference (9) with the Correlation Curve of the Present Analysis ($L^* = 2$).

CHAPTER V

CONCLUSIONS AND RECOMMENDATIONS

The possibility of reducing the overall heat transfer rate to a surface by exploiting the reduction in heat transfer rates in regions of cavity-induced separated flows for laminar flow has been studied. An implicit finite-difference solution method has been developed for solving the constant-pressure laminar boundary-layer equations for compressible flow to obtain velocity and enthalpy profiles for both attached boundary layers and free shear layers with arbitrary initial profiles. This solution method has been employed to calculate the heat transfer rate to a flat plate with a series of cavities located in the surface. The effects of the number of cavities, the cavity spacing, the length of the initial attached-flow region, and the reattachment geometry have been studied.

The results of this investigation may be summarized in the following conclusions:

1. The finite-difference solution procedure employed in the present analysis has been shown to provide a stable, accurate solution of the constant-pressure laminar boundary-layer equations for both attached boundary layers and free shear layers. The solution for the non-similar growth of the free shear layer with finite initial thickness offers an advantage over previous methods because the necessity of a separate solution for the dividing streamline location is eliminated.

In addition, the transformation of the normal coordinate to a finite interval employed here provides an explicit inverse relation in contrast to the Crocco coordinate transformation which requires an integration to invert.

2. For a multiple-cavity configuration utilizing a sharp-cusp reattachment geometry with a given ratio of cavity length to attached-flow length between cavities the distributions of local heat transfer rates for the attached-flow regions downstream of each cavity converge to a single curve when compared to an attached flow at the corresponding streamwise distance. These limiting curves are useful as approximate correlation curves which may be employed to estimate rapidly the heat transfer rates to surfaces containing cavities.

3. The local energy transfer rate across the dividing streamline for a free shear layer is essentially 56 per cent of that for an attached boundary layer at the corresponding location. This result indicates that the average heat transfer rate across a free shear layer is essentially 56 per cent of that to an equivalent attached flow not only for the case of zero initial thickness (as determined by Chapman) but for the case of a finite initial thickness as well.

4. The correlation technique developed in this study provides overall heat transfer rates for multiple-cavity configurations in good agreement with the results from the finite-difference solution with much less computational effort. The results from the correlation are conservative, and the agreement improves as the number of cavities increases.

5. The additional cavities downstream of the first cavity can significantly reduce the overall heat transfer when compared to a con-

figuration with fewer cavities, with the reduction due to multiple cavities increasing as the cavity spacing decreases.

6. Where multiple cavity-separated regions are employed to reduce the overall heat transfer rate to a given surface, the maximum reduction occurs when the cavities are as long as practicable and the cavity spacing is chosen so that the largest number of cavities is used consistent with the condition that the length of the attached-flow region following the last cavity be as short as possible.

7. Investigation of the effects of bluntness at reattachment using blunt body theory indicates that, for the typical reattachment Mach number of 1.8, a blunt plate with a ratio of nose thickness to plate length of 0.1 would have an overall heat transfer rate only about three per cent greater than a sharp-edged flat plate of the same length.

In summary, the results of this investigation demonstrate that multiple cavity-separated regions can reduce the overall heat transfer rate in comparison to an equivalent completely-attached flow. This reduction for the multiple-cavity configurations is perhaps disappointing in comparison to the potential heat transfer reduction for a completely-separated flow. A study of the effects of bluntness indicate that blunting increases the heat transfer rate in comparison to a sharp-edged geometry. However, this increase is small for moderate bluntness ratios.

The present analysis has assumed that each of the cavities are sufficiently deep to be of the deep, open type. The type of cavity flow is dependent upon the flow detail in the cavity. Determination of the possible restrictions on the geometry necessary to guarantee the deep,

open type cavity flow must await the analysis of the recirculating flow in the cavity. One approach which merits study is the solution of the Navier-Stokes equations for the recirculating flow in the cavity coupled with a boundary-layer approach for the viscous-flow region outside the cavity.

Further studies of the reattachment region are recommended since this region may be important from the standpoint of reducing the heat transfer rate. Both experimental and analytical investigations are of interest for various reattachment geometries.

APPENDIX A

STABILITY ANALYSIS OF THE MOMENTUM EQUATION

The stability of the finite-difference form of the momentum equation in (S, ζ) coordinates is investigated in this appendix.

From equation (26) the momentum equation in (S, ζ) coordinates is given by

$$u^* \frac{\partial u^*}{\partial S} = -\alpha(1 - \zeta^2)(v^* + 2\alpha\zeta) \frac{\partial u^*}{\partial \zeta} + \alpha^2(1 - \zeta^2)^2 \frac{\partial^2 u^*}{\partial \zeta^2} \quad (A-1)$$

Using the finite-difference approximations for equally-spaced grid points presented in Chapter III, the momentum equation may be replaced by the difference equation

$$\begin{aligned} u_{i+1,j}^* - u_{i,j}^* = & A(u_{i+1,j+1}^* - u_{i+1,j-1}^* + u_{i,j+1}^* - u_{i,j-1}^*) \\ & + B(u_{i+1,j+1}^* - 2u_{i+1,j}^* + u_{i+1,j-1}^* + u_{i,j+1}^* \\ & - 2u_{i,j}^* + u_{i,j-1}^*) \end{aligned} \quad (A-2)$$

where

$$A = - \frac{\alpha(1 - \zeta^2)}{4u_{av}^*} \frac{\Delta S}{\Delta \zeta} (v_{av}^* + 2\alpha\zeta)$$

$$B = \frac{\alpha^2(1 - \zeta^2)^2}{2u_{av}^*} \frac{\Delta S}{(\Delta \zeta)^2}$$

and u_{av}^* and v_{av}^* are given by equation (43). Equation (A-2) is simply equation (42) expressed in a slightly different form.

Assuming that u_{av}^* and v_{av}^* in the coefficients A and B are constants which are prescribed from the previous iteration, equation (A-2) is linear in the $u_{i,j}^*$. It may be shown that the truncation error $\epsilon_{i,j}$ between the exact solution of (A-2) and the numerical solution (which includes roundoff errors) satisfies the same difference equation, thus

$$\begin{aligned} \epsilon_{i+1,j} - \epsilon_{i,j} = & A(\epsilon_{i+1,j+1} - \epsilon_{i+1,j-1} + \epsilon_{i,j+1} - \epsilon_{i,j-1}) \\ & + B(\epsilon_{i+1,j+1} - 2\epsilon_{i+1,j} + \epsilon_{i+1,j-1} + \epsilon_{i,j+1} \\ & - 2\epsilon_{i,j} + \epsilon_{i,j-1}) \end{aligned} \quad (A-3)$$

To investigate the behavior of the truncation error for successive steps in the S-direction, the method used by von Neumann and described in detail by O'Brien, et al. (24) is employed. In this method an arbitrary error distribution is assumed at some station S_1 , and the growth or decay of this error is investigated. The Fourier decomposition of error is introduced by assuming an error distribution of the form

$$\epsilon_{i,j} = e^{\hat{i}\xi j} e^{\beta i} \quad (A-4)$$

where

$$(\hat{i})^2 = -1$$

Substitution of equation (A-4) into equation (A-3) yields an expression for the error growth $\phi = e^{\beta}$ as follows

$$\frac{\phi - 1}{\phi + 1} = (A + B) e^{\hat{i}\xi} + (B - A) e^{-\hat{i}\xi} - 2B$$

Using the relations

$$e^{\hat{i}\xi} = \cos \xi + \hat{i} \sin \xi$$

$$e^{-\hat{i}\xi} = \cos \xi - \hat{i} \sin \xi$$

results in the following expression

$$\frac{\phi - 1}{\phi + 1} = -2B(1 - \cos \xi) + 2A\hat{i} \sin \xi$$

Now employ the trigonometric identities

$$1 - \cos \xi = 2 \sin^2 \frac{\xi}{2}$$

$$\sin \xi = 2 \sin \frac{\xi}{2} \cos \frac{\xi}{2}$$

to obtain

$$\frac{\phi - 1}{\phi + 1} = -4B \sin^2 \frac{\xi}{2} + 4A\hat{i} \sin \frac{\xi}{2} \cos \frac{\xi}{2}$$

Solving for ϕ yields

$$\phi = \frac{1 - 4B \sin^2 \frac{\xi}{2} + 4Ai \sin \frac{\xi}{2} \cos \frac{\xi}{2}}{1 + 4B \sin^2 \frac{\xi}{2} - 4Ai \sin \frac{\xi}{2} \cos \frac{\xi}{2}}$$

Noting that for a complex number $a + ib$

$$|a + ib|^2 = a^2 + b^2$$

the expression for ϕ may be written

$$|\phi|^2 = \frac{\left(1 - 4B \sin^2 \frac{\xi}{2}\right)^2 + 16 A^2 \left(\sin \frac{\xi}{2} \cos \frac{\xi}{2}\right)^2}{\left(1 + 4B \sin^2 \frac{\xi}{2}\right)^2 + 16 A^2 \left(\sin \frac{\xi}{2} \cos \frac{\xi}{2}\right)^2} \quad (\text{A-5})$$

As stated by O'Brien, et al. a necessary and sufficient condition to insure that the error introduced at each step does not grow as S increases is

$$|\phi| \leq 1$$

An examination of equation (A-5) reveals that $|\phi| \leq 1$ for all $B \geq 0$ and all A . Since B is given by

$$B = \frac{\alpha^2 (1 - \zeta^2)^2}{2u_{av}^*} \frac{\Delta S}{(\Delta \zeta)^2}$$

this implies that

$$|\phi| \leq 1 \quad \text{for} \quad u_{av}^* \geq 0$$

In summary, assuming that the coefficients u^* and v^* in equation (A-1) are replaced by constants u_{av}^* and v_{av}^* , it may be concluded that the truncation error introduced at each step does not grow with subsequent steps in the S-direction if $u_{av}^* \geq 0$. With this assumption, the momentum difference equation is stable for any positive step size ΔS , and the step size is governed merely by the desired accuracy at each step.

APPENDIX B

THE FINITE-DIFFERENCE SOLUTION OF THE LAMINAR, FLAT-PLATE BOUNDARY LAYER

In this appendix the finite-difference solution procedure presented in Chapter III is applied to the laminar, flat-plate boundary layer. The velocity and enthalpy profiles from the finite-difference solution are compared with solutions appearing in the literature. In addition, the wall shear stresses and the heat transfer rates computed by the difference solution are compared with solutions derived from similarity analyses.

As noted in Chapter II, the equations in (S,Y) coordinates are in incompressible form. Thus the velocity profile u^* in (S,Y) coordinates may be compared directly with the familiar Blasius asymptotic profile. The Blasius solution is given in terms of a similarity parameter η , which in the present case is simply

$$\eta = \frac{Y}{\sqrt{S}}$$

The Blasius solution also provides an expression for the wall shear which, when expressed in the system used here, becomes

$$\left(\frac{\partial u^*}{\partial Y} \right)_{Y=0} = \frac{0.332}{\sqrt{S}}$$

The finite-difference solution was carried out in the following manner. The velocity field was assumed uniform at $S = 0$ with a discontinuity at $Y = 0$, that is

$$u^* = 1, \quad v^* = 0 \quad \text{for } S = 0, \quad Y > 0$$

$$u^* = 0, \quad v^* = 0 \quad \text{for } S = 0, \quad Y = 0$$

A finite-difference mesh with $N + 1$ grid points ($j = 0, 1, 2, \dots, N$) equally spaced over the interval $0 \leq \zeta \leq 1$ was employed. The streamwise step interval ΔS was varied as the square root of the distance from the leading edge S . This choice is based on the fact that the laminar boundary-layer parameters vary as a function of the variable $\eta = Y/\sqrt{S}$. Hence, a streamwise step interval ΔS which varies as \sqrt{S} maintains an accuracy in the finite-difference formulation which is consistent with that obtained with a constant step interval in the direction normal to the streamwise direction. This variation permits small values of ΔS for small S , where streamwise gradients are large, while allowing relatively large values of ΔS for large S , where streamwise gradients are smaller. This is an advantage over the selection of a constant value for ΔS since a value ΔS small enough to yield an accurate solution for small S requires an excessive amount of calculation for large values of S .

In the transformed coordinate system, the grid point $j = N$ is at $\zeta = 1$ which corresponds to $Y = \infty$. Thus the grid point $j = N - 1$ located at $\zeta = 1 - \Delta\zeta$ corresponds to the last finite value of Y in the mesh as

depicted in Figure 29. Ultimately, as the solution progresses downstream the boundary layer will grow until it reaches the last finite value of Y at $j = N - 1$. When this condition occurs, the transformation constant α is changed (from α to α' in Figure 29) such that the new value of Y corresponding to the point $j = N - 1$ (i.e., $Y(j = N - 1, \alpha')$) is outside the boundary layer. Thus at least two grid points always lie outside the boundary layer, insuring uniform velocity and enthalpy profiles outside the boundary layer. In order to maintain the numerical accuracy without excessively reducing the computing efficiency, the number of grid points is increased such that the spacing for the first grid point (in terms of Y) is unchanged. Correspondingly, all other grid spacings decrease slightly. For this study, each time this situation occurred, the value of N was increased by 20 per cent. The values of the dependent variables at each of the new grid points is determined by linear interpolation.

The velocity profile u^* from the numerical solution is compared to the Blasius similar profile in Figure 30. The numerical solution was carried out in 100 streamwise steps from $S = 0$ to $S = 1$, with the step size varying from about 6×10^{-4} at the beginning to approximately 2×10^{-2} at the end. The initial difference mesh employed $N = 25$ (i.e., 26 grid points), and, with one interpolation being required in the interval, the value of N at $S = 1$ was 30.

The evaluation of the wall shear was accomplished by fitting an interpolating polynomial to the values of u^* at the grid points near $Y = 0$ and evaluating the derivative of the polynomial at $Y = 0$. The numerical results for a linear and a parabolic curve fit are compared to

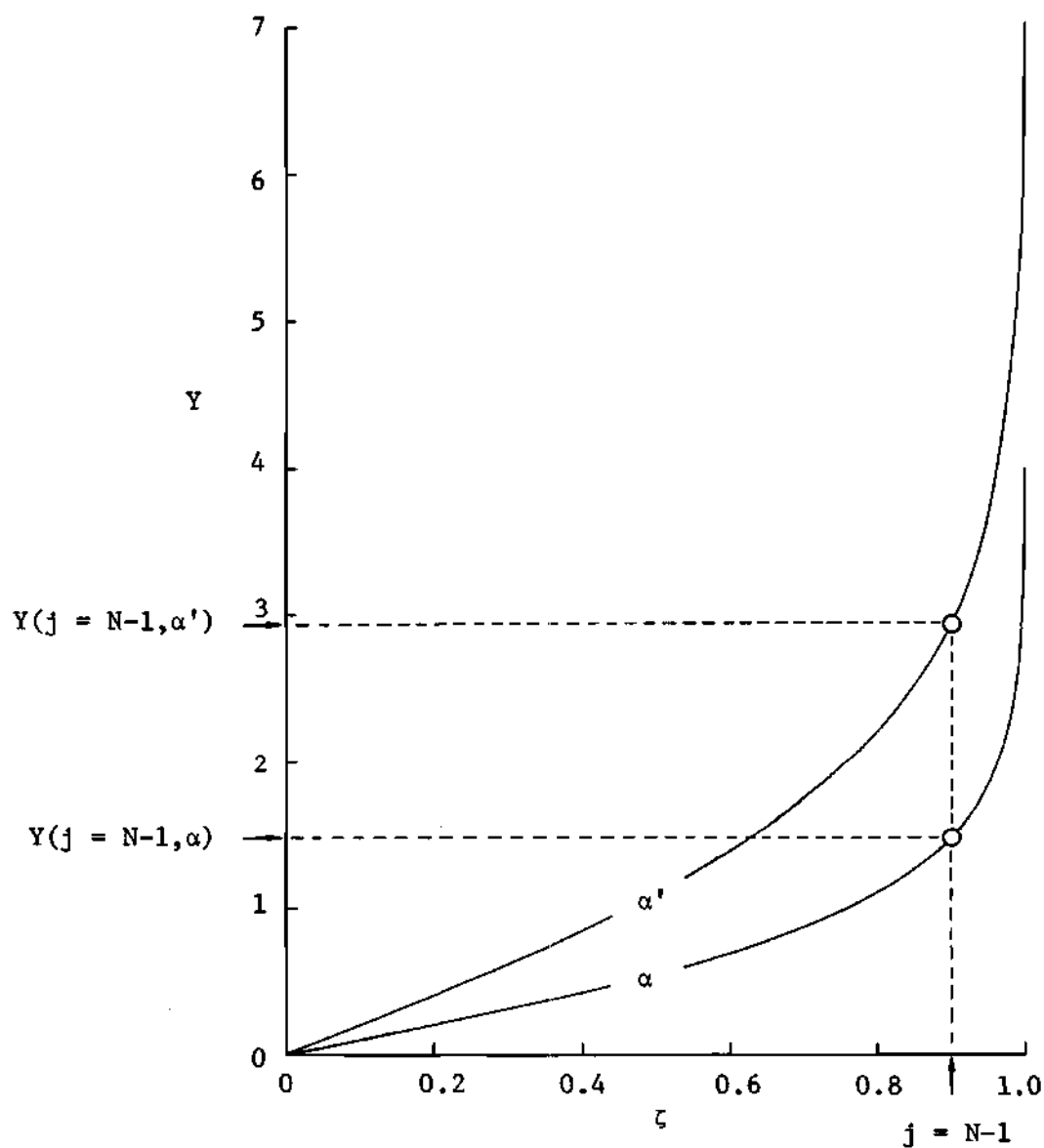


Figure 29. Illustration of the Effect of the Transformation Constant α on the Values of Y corresponding to the Grid Points in the Finite-Difference Mesh.

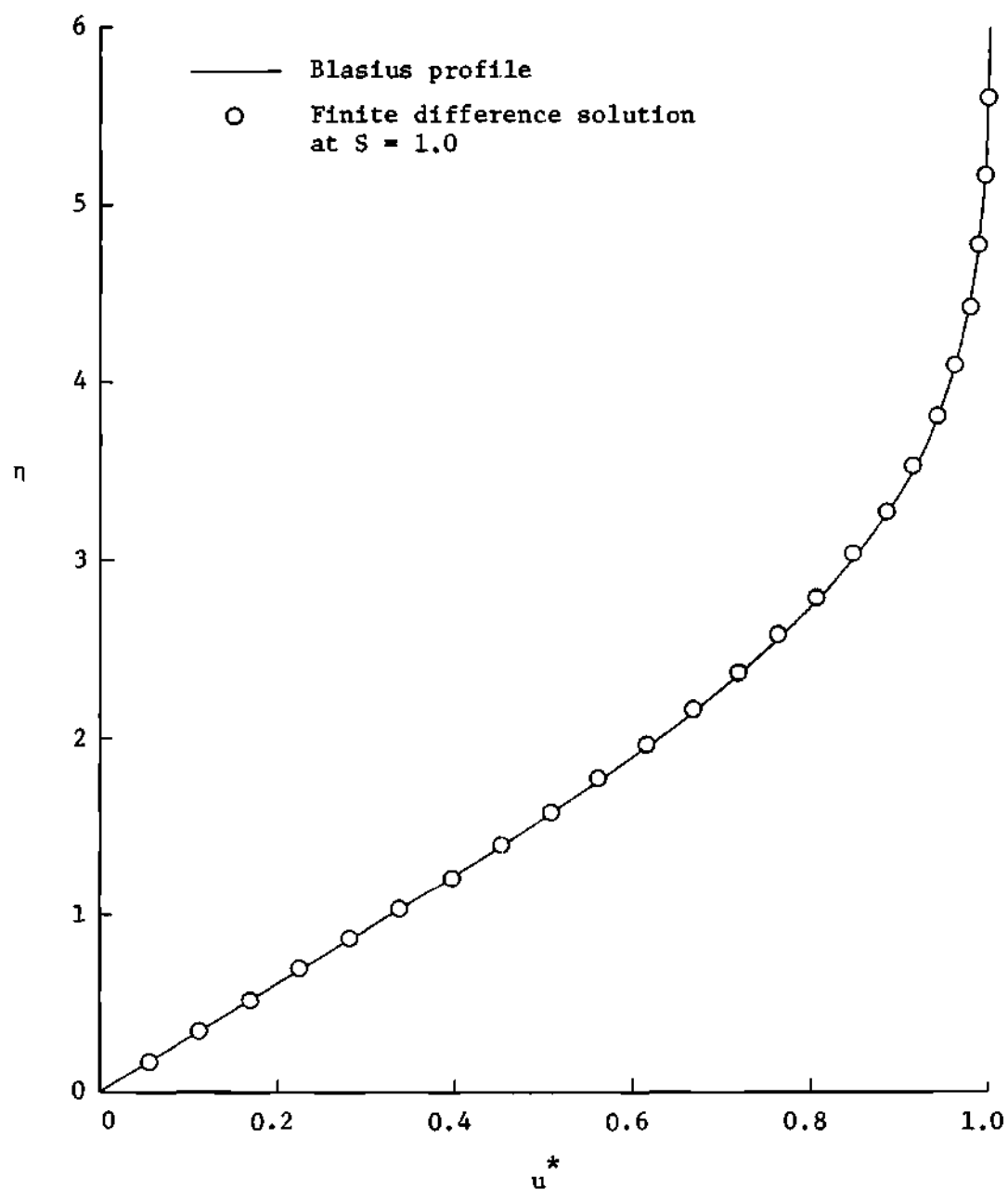


Figure 30. Comparison of the Flat-Plate Velocity Profile from the Numerical Solution with the Blasius Similar Profile.

the Blasius solution in Figure 31. The fairly constant values of wall shear for small values of S from the numerical results are a consequence of the finite distance between the grid points. The maximum value of $\left(\frac{\partial u^*}{\partial Y}\right)_{Y=0}$ which can be predicted from the finite-difference solution corresponds to the situation $u^* = 1$ for all grid points for which $Y > 0$. The results for both curve fits converge to the Blasius solution, with both curves differing less than one per cent from the Blasius solution for $S \geq 2 \times 10^{-1}$. This point of convergence may be moved to a smaller value of S by decreasing the grid spacing.

While the wall shear computed using the linear curve fit seems to approach the Blasius value more rapidly than that using the parabolic curve fit, the parabolic curve fit is employed in the present analysis for the following reason. The objective of this analysis is the integrated heat transfer to the surface. As will be shown later, the integrated values computed using the parabolic fit are more accurate than those computed using the linear fit. This is attributed to the more pronounced "overshoot" of the Blasius curve for the parabolic fit. The higher values of the derivative for this case tend to offset the low values of the derivative for small S when integrated over S .

The enthalpy function profiles from the numerical solution using $Pr = 0.72$ at $S = 1$ are plotted versus u^* in Figure 32. Presented for comparison are the profiles given by Van Driest (25) for $Pr = 0.725$. The comparison is seen to be good. The differences are greatest for H_1 , which varies most with Prandtl number.

The local heat transfer rates calculated from the numerical solution are presented in Figure 33. The solid line is from Chapman (5), and the

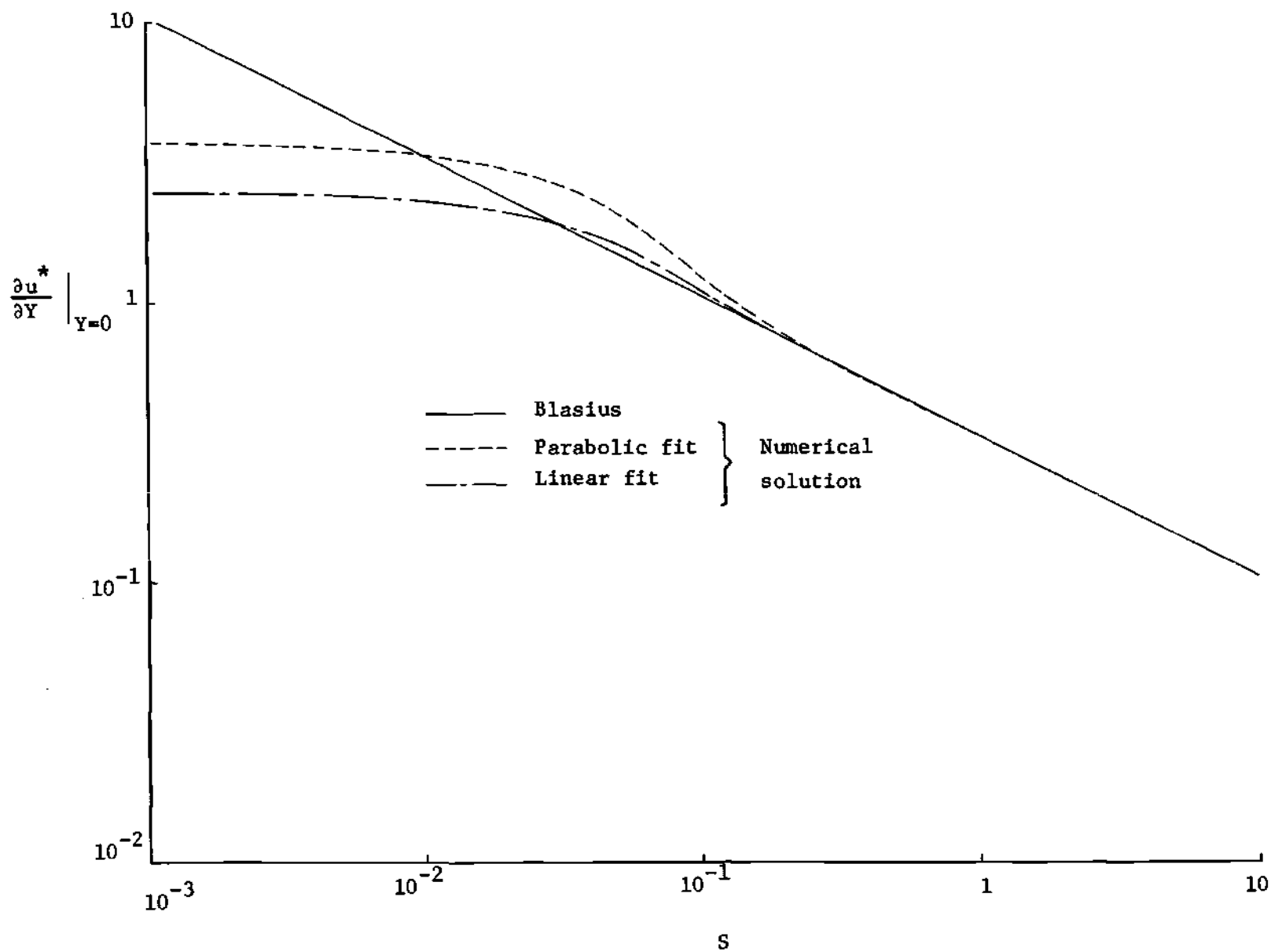


Figure 31. Comparison of the Wall Shear Computed Using Linear and Parabolic Curve Fits with Blasius Value.

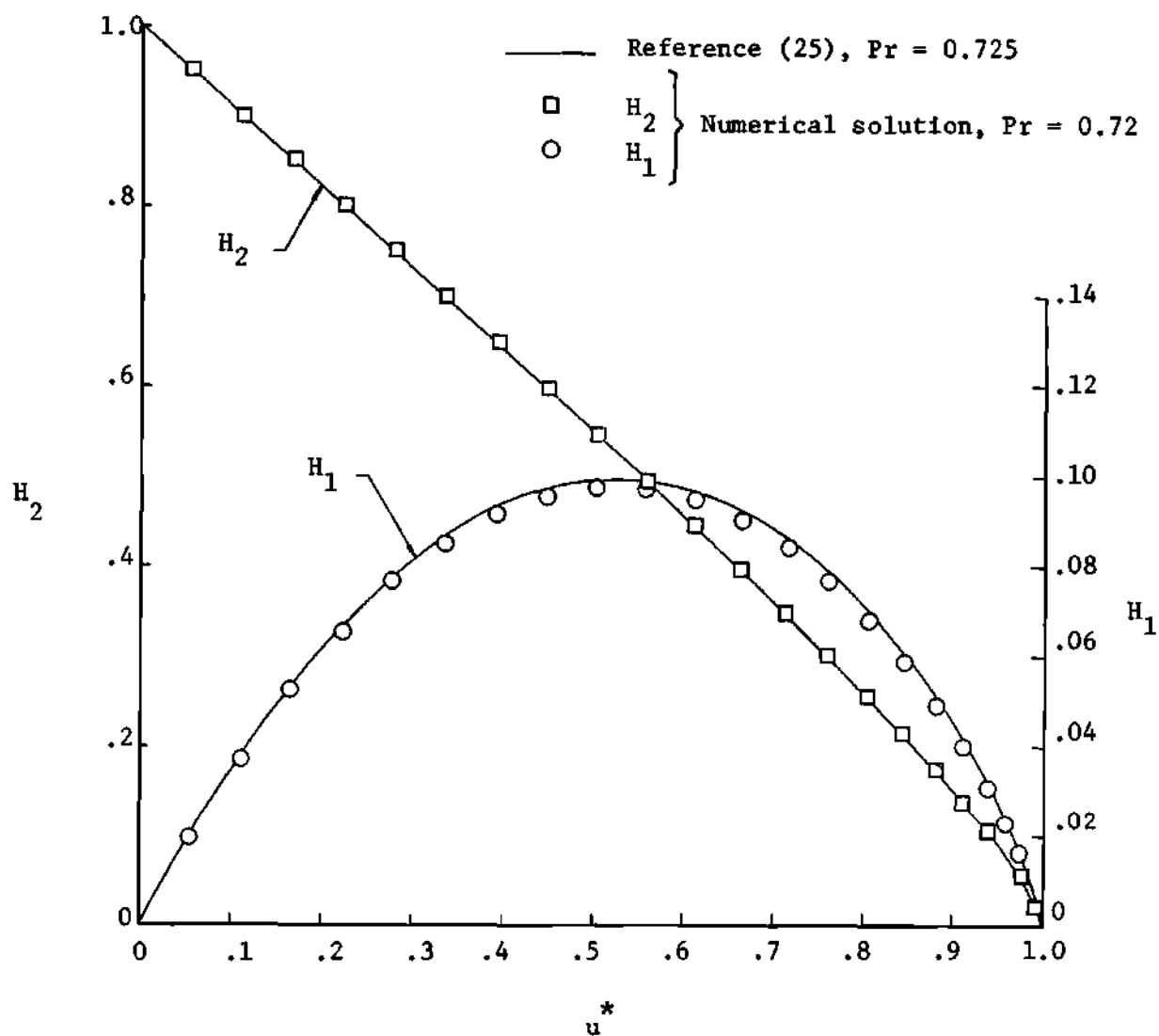


Figure 32. Comparison of the Enthalpy Function Profiles for the Flat Plate from the Finite-Difference Solution with the Similar Profiles of Reference (25).

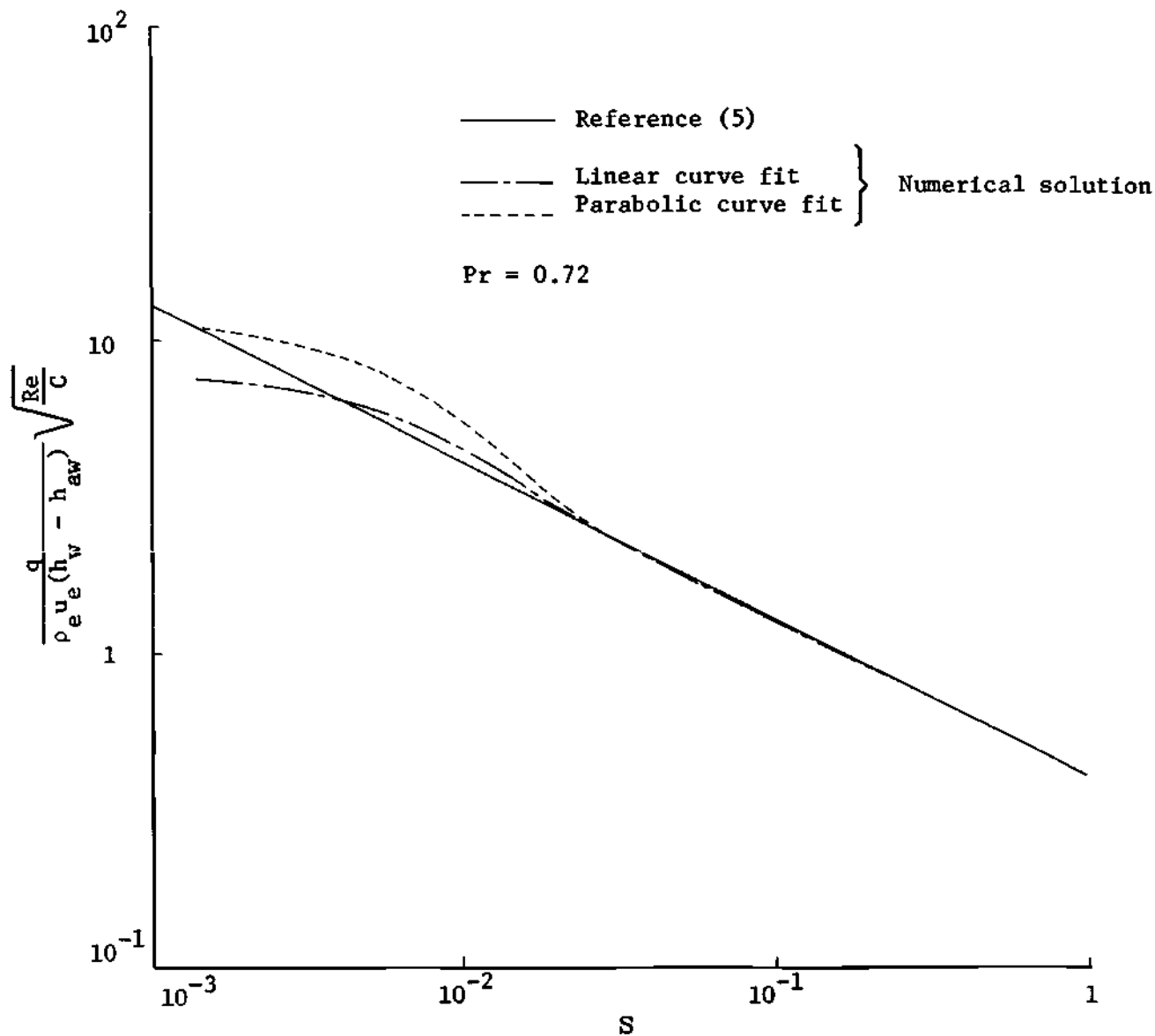


Figure 33. Comparison of Local Heat Transfer Rates Computed Using Linear and Parabolic Curve Fits with Similarity Solution.

two curves for the numerical results differ in the type of curve fit employed to compute $\left(\frac{\partial H_2}{\partial Y}\right)_{Y=0}$. As in the case for the wall shear, both of the curves from the numerical solution converge to the solution from the similarity analysis. These results converge to the solid line for $S = 3 \times 10^{-2}$. This point of convergence may be moved to smaller values of S by decreasing the grid spacing.

The overall heat transfer rate to the flat plate was computed by integrating the local heat transfer rates from Figure 33. The integration was performed using the trapezoidal rule, and the results for both the linear and parabolic curve fit are presented in Figure 34. The solid line is from Chapman (5). Here, the advantage of employing the parabolic curve fit is apparent. These results indicate that, with the number of grid points and the step size used here, the parabolic curve fit yields values of the overall heat transfer rate accurate within one per cent for $S \geq 10^{-1}$. For the present study, which is concerned with geometries for which $S \geq 10^{-1}$, the number of grid points and step size used in this analysis yields sufficient accuracy. Accurate values for the overall heat transfer rate for smaller values of S may be obtained by employing a smaller grid spacing.

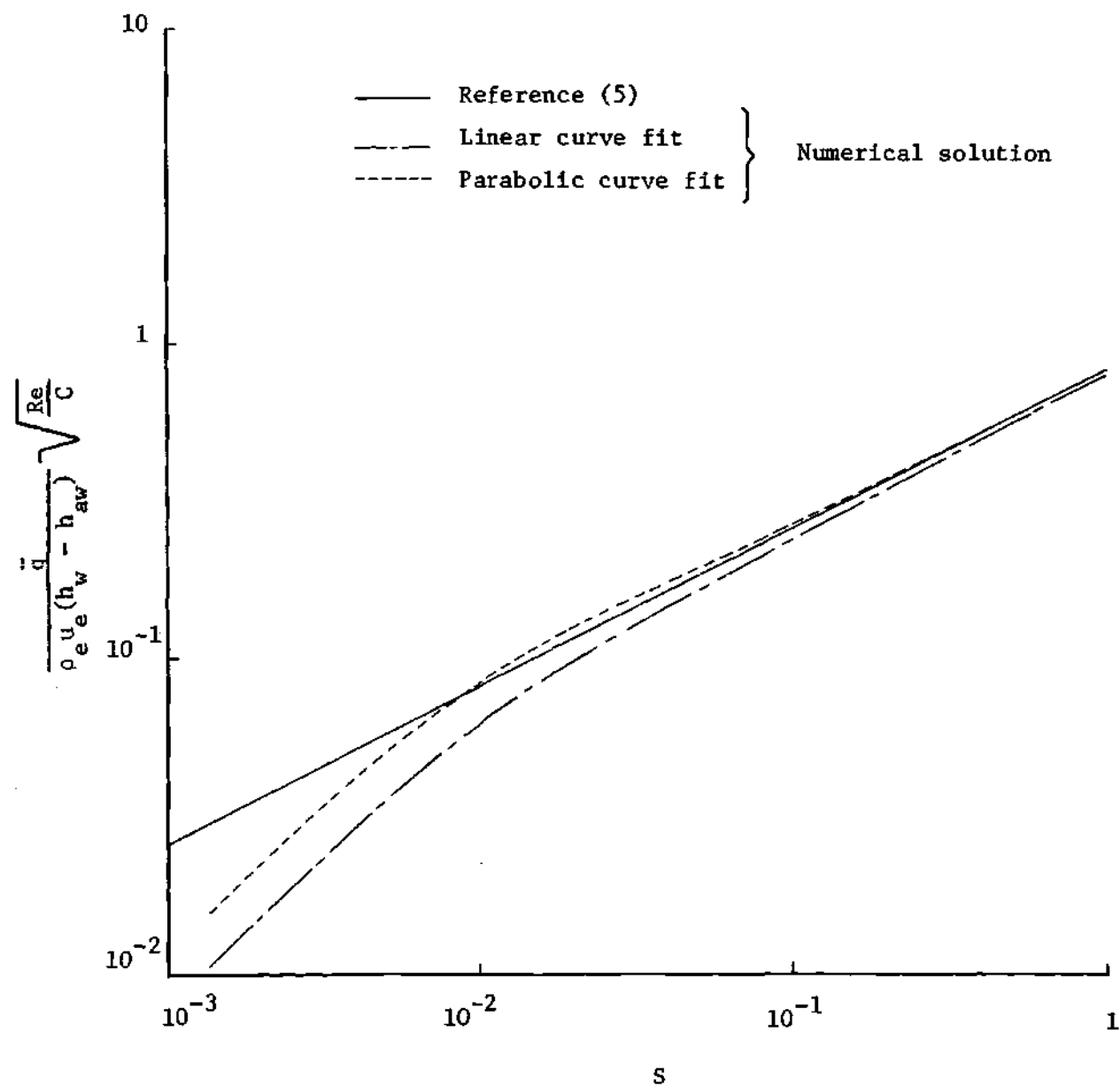


Figure 34. Overall Heat Transfer Rate to a Flat Plate from the Finite-Difference Solution and Comparison with the Asymptotic Solution (Pr = 0.72).

APPENDIX C

THE FINITE-DIFFERENCE SOLUTION OF THE LAMINAR FREE

SHEAR LAYER

In this appendix the finite-difference solution procedure presented in Chapter III is applied to the laminar free shear layer. Two situations are considered. First, the non-similar growth of the free shear layer with finite initial thickness is studied. Second, the similar profiles of Chapman (5) are used as initial profiles and the solution carried out for a number of streamwise steps to investigate whether or not the finite-difference solution preserves the similar solution.

The Laminar Free Shear Layer with Finite Initial Thickness

For this study, a Blasius profile is used as an initial profile for a laminar free shear layer. A mesh of equally-spaced grid points in the interval $-1 \leq \zeta \leq 1$ was used with an equal number of grid points (N) above and below the dividing streamline ($\zeta = 0$). The dependent variables for the grid points above the dividing streamline were taken from the flat-plate solution at $S = 1$, while the values at each of the grid points below $\zeta = 0$ were set equal to the boundary values at $\zeta = -1$. The solution was then carried out using a step size ΔS which varied as the square root of S , where S is measured from the beginning of the free shear layer. The initial value of N was 30 (corresponding to the value at the end of the flat-plate solution) and was increased by 20 per cent whenever the edge of

the free shear layer reached the next-to-last grid point as in the flat-plate solution.

The results of this investigation appear in Figures 35, 36, 37, and 38. In Figure 35, the dividing streamline velocity distribution is compared with the results obtained by Denison and Baum (6) in terms of the distance parameter S^* which in the present study becomes

$$S^* = \left(\frac{\partial u}{\partial Y} \right)_{Y=0, S=0}^2 S$$

The dividing streamline velocity u_d^* is the velocity at the grid point located at $\zeta = 0$. The present solution converges to the results of Denison and Baum (6) at $S^* = 5 \times 10^{-2}$. This point of convergence may be moved to a smaller value of S^* by decreasing the grid spacing. The excellent agreement demonstrates the utility of the present solution method, which does not require a separate starting solution as encountered in the Crocco coordinate system. (See reference (6).)

The conversion of the flat-plate boundary-layer profiles into the asymptotic, similar shear layer profiles of Chapman is depicted in Figures 36, 37, and 38. The profiles at successive stations downstream of separation are shown to approach the Chapman profiles as S^* increases.

Numerical Study of the Similar Profiles of the Free Shear Layer

Still another check on the solution method was performed by using the similar profiles given by Chapman as initial profiles for the finite-difference solution procedure used in the present analysis. The tabulated profiles in reference 5 were input at $S = 1$ so that $Y = \eta$. Then

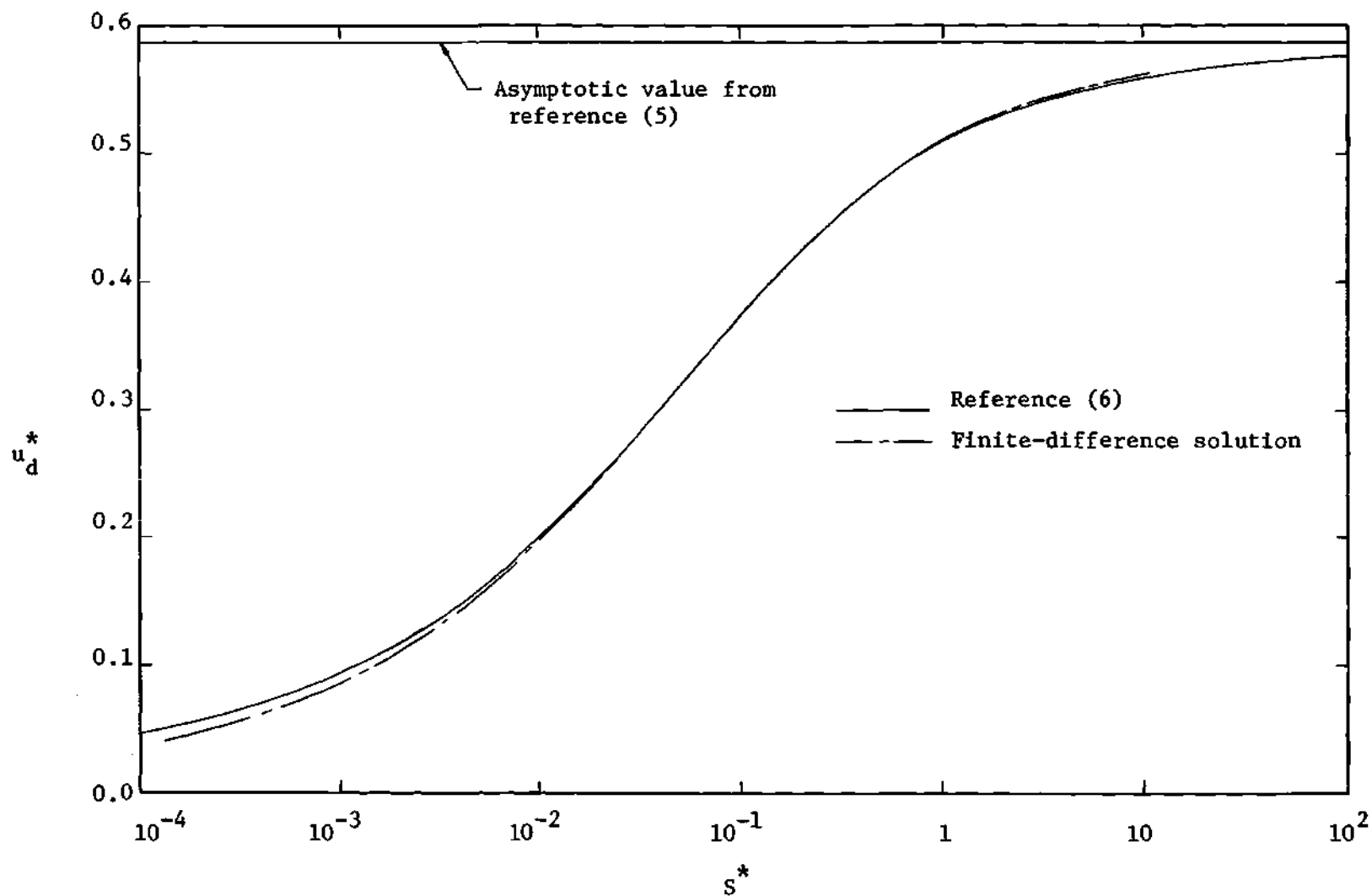


Figure 35. Dividing Streamline Velocity Distribution from the Finite-Difference Solution with Initial Blasius Profile and Comparison with Reference (6).

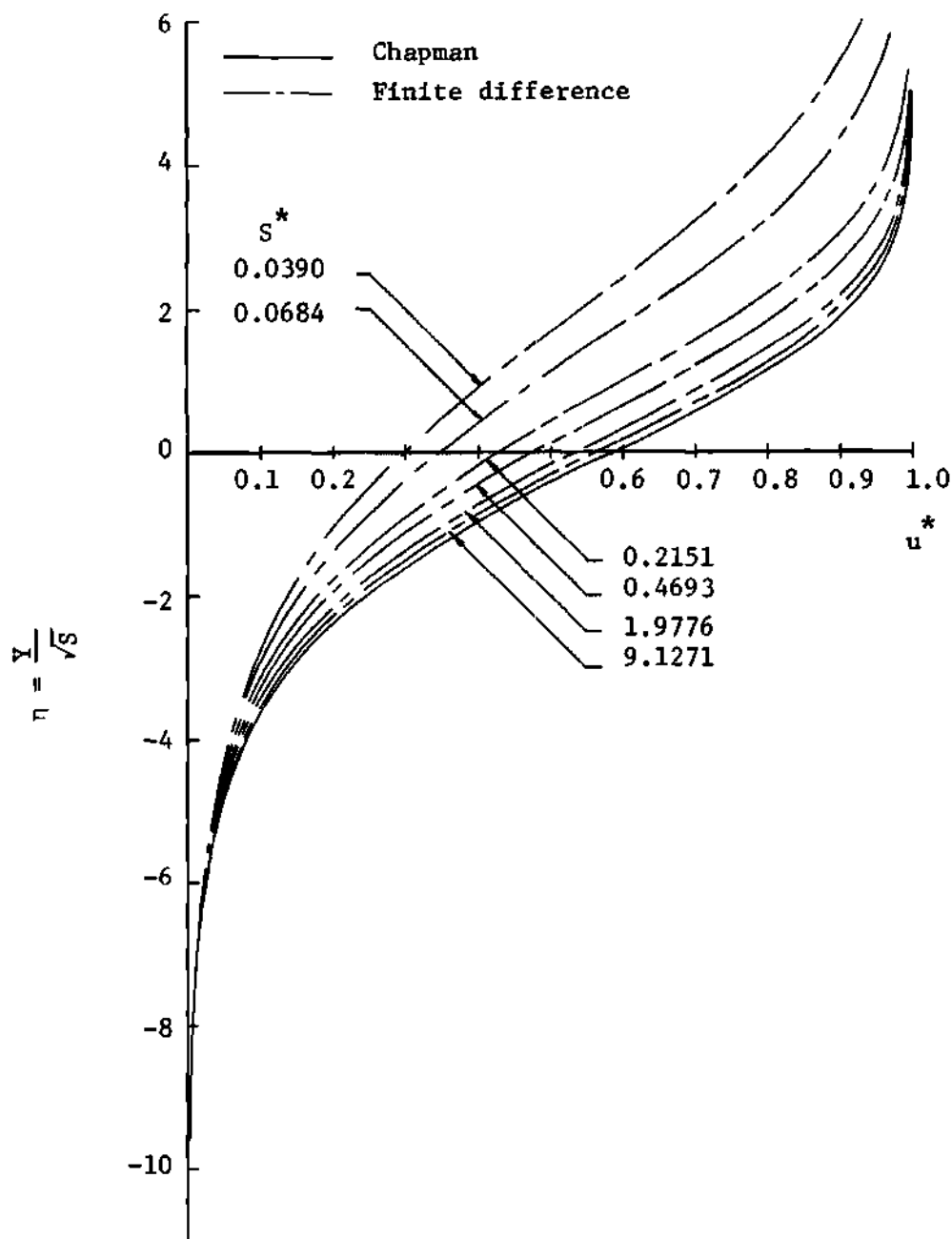


Figure 36. Development of Velocity Profile for the Free Shear Layer from the Finite-Difference Solution with Flat-Plate Profile at Separation.

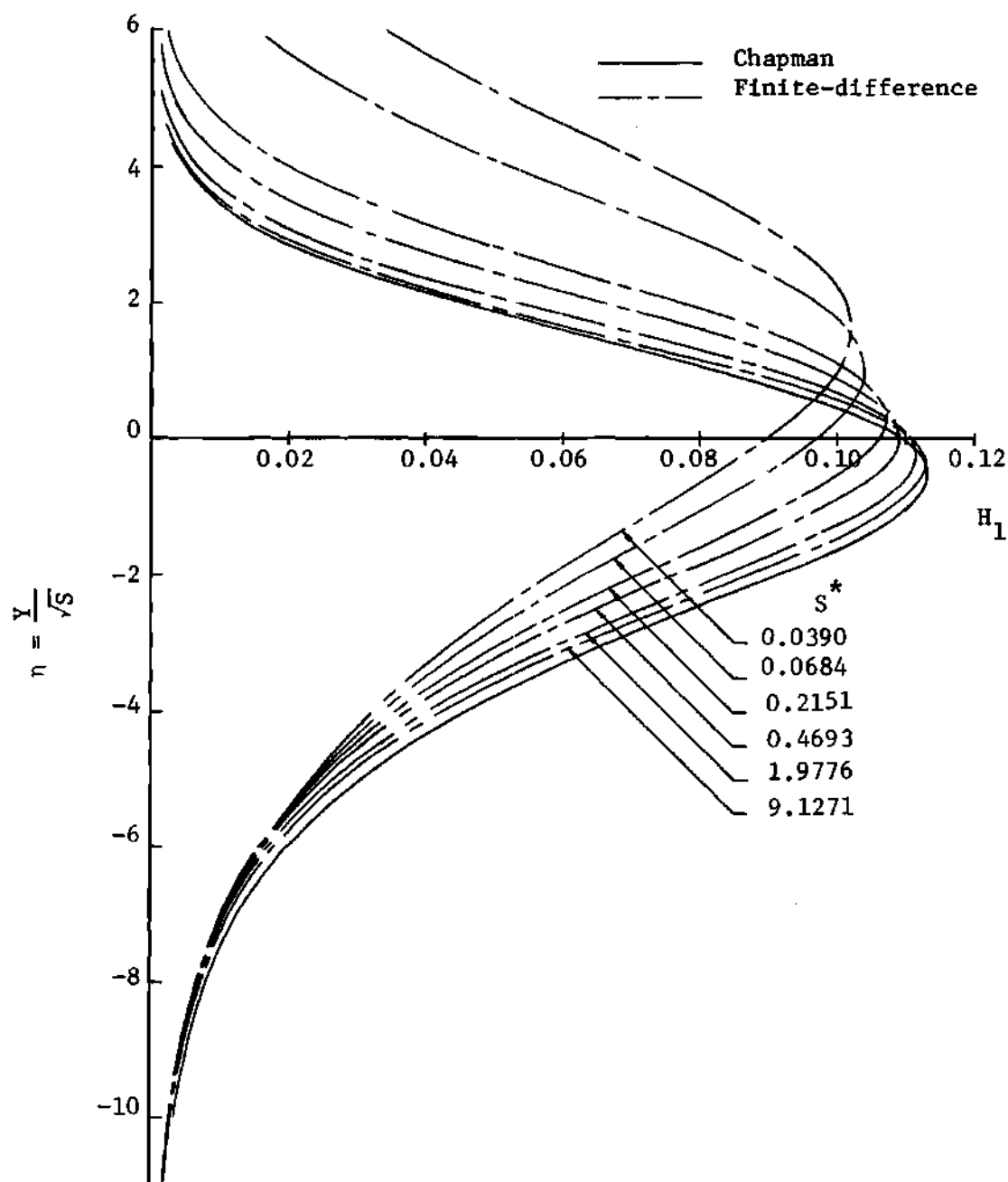


Figure 37. Development of Enthalpy Function Profile H_1 for the Free Shear Layer from the Finite-Difference Solution with Flat-Plate Profile at Separation, $Pr = 0.72$.

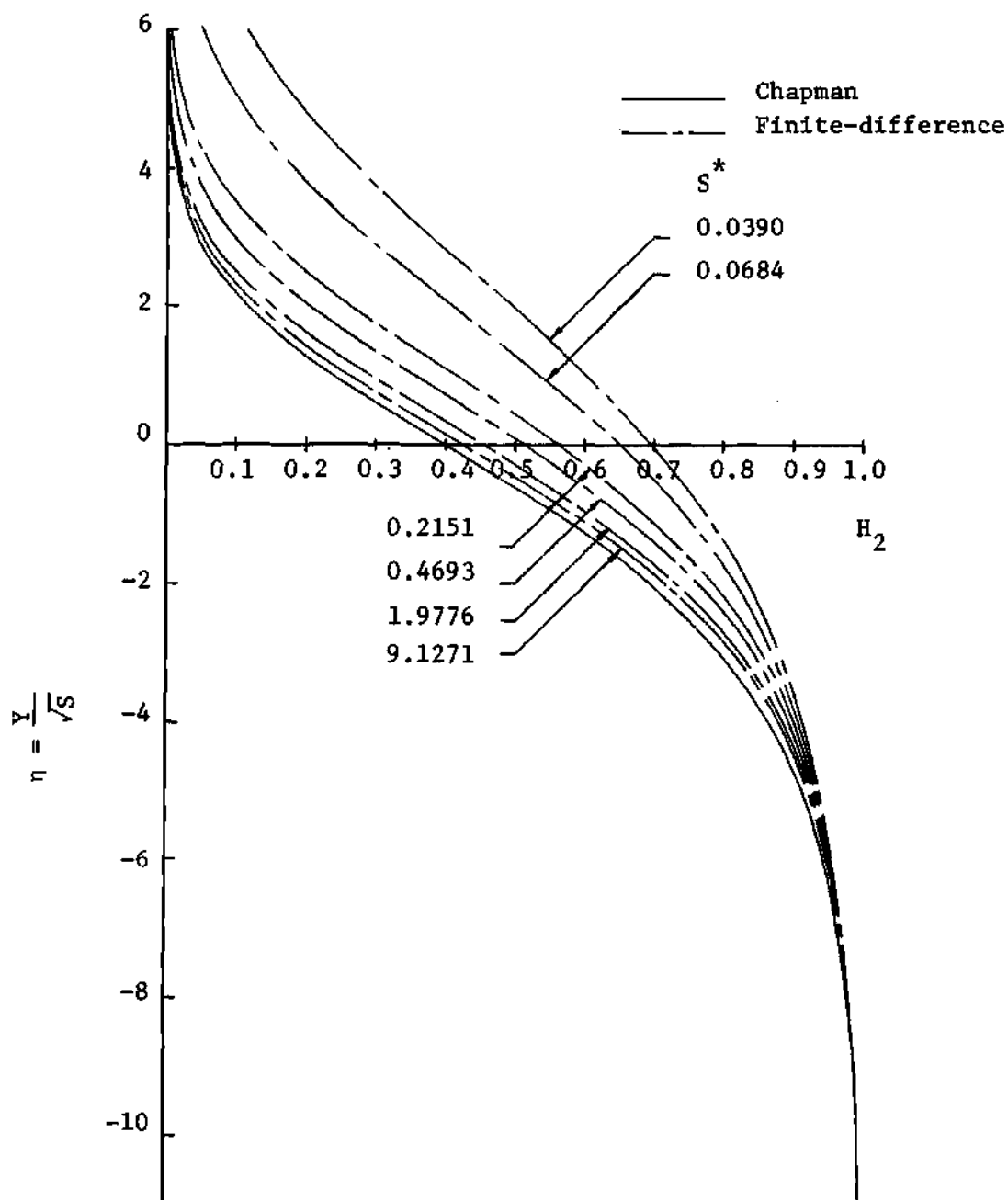


Figure 38. Development of Enthalpy Function Profile H_2 for the Free Shear Layer from the Finite-Difference Solution with Flat-Plate Profile at Separation, $Pr = 0.72$.

the solution was carried out for a number of streamwise steps and the resulting profiles were plotted versus the similarity parameter η . The profiles of u^* , H_1 , and H_2 after over 500 streamwise steps are presented in Figures 39, 40, and 41.

The excellent agreement indicates that the finite-difference solution preserves the similar profiles of Chapman.

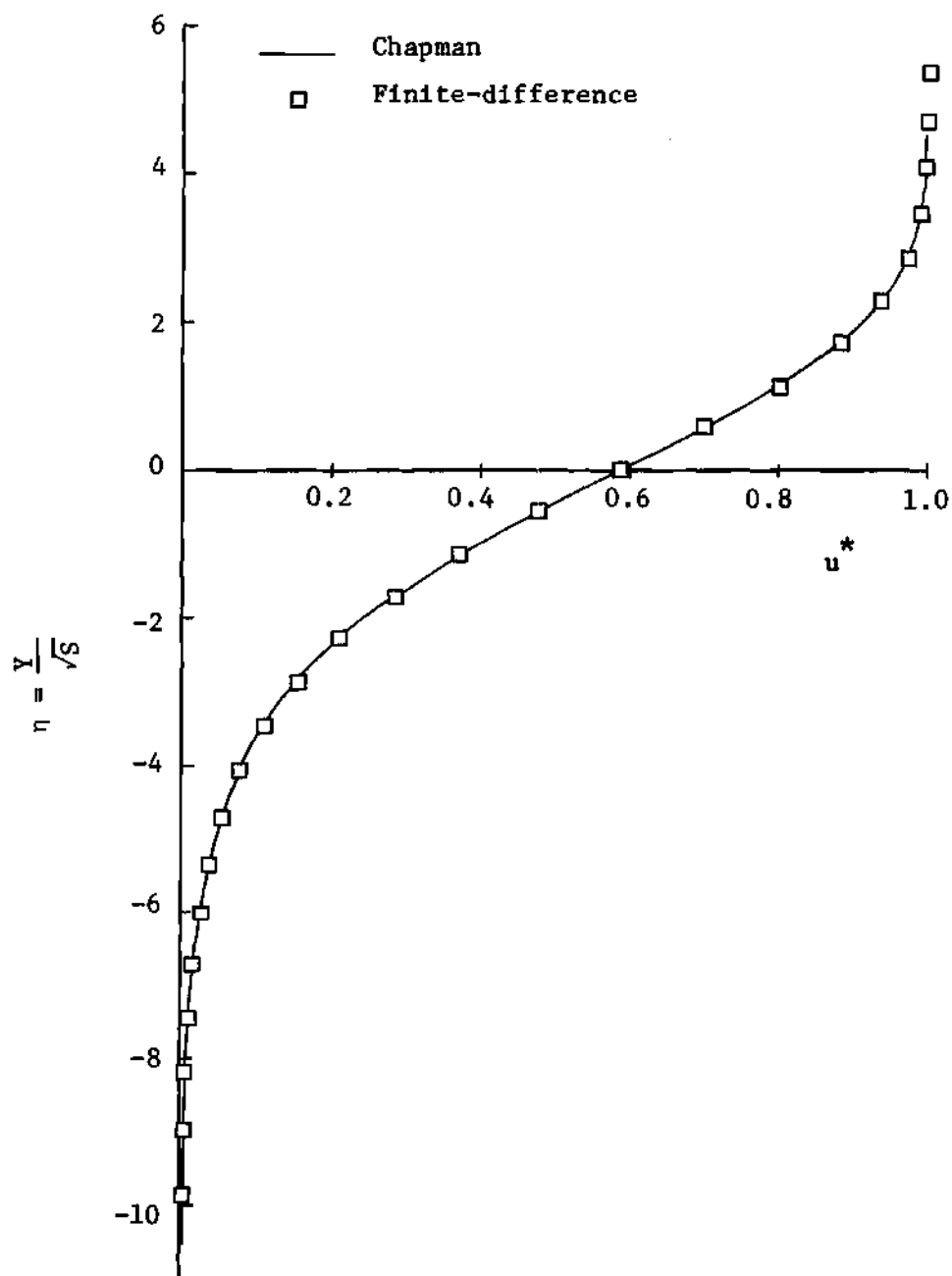


Figure 39. Velocity Profile from the Finite-Difference Solution with Chapman Profile Used as Initial Profile, $Pr = 0.72$.

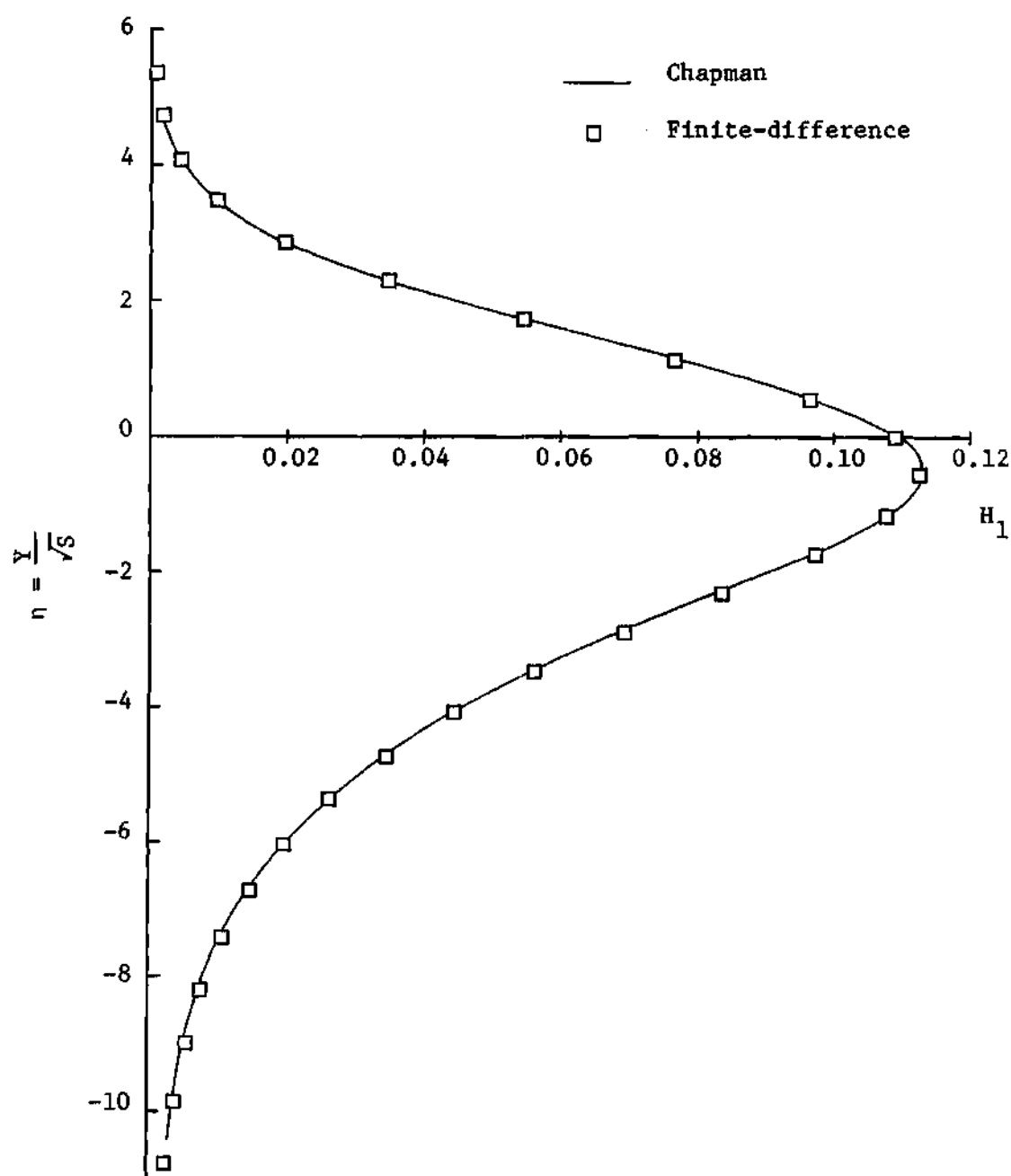


Figure 40. Enthalpy Function Profile H_1 from the Finite-Difference Solution with Chapman Profile Used as Initial Profile, $Pr = 0.72$.

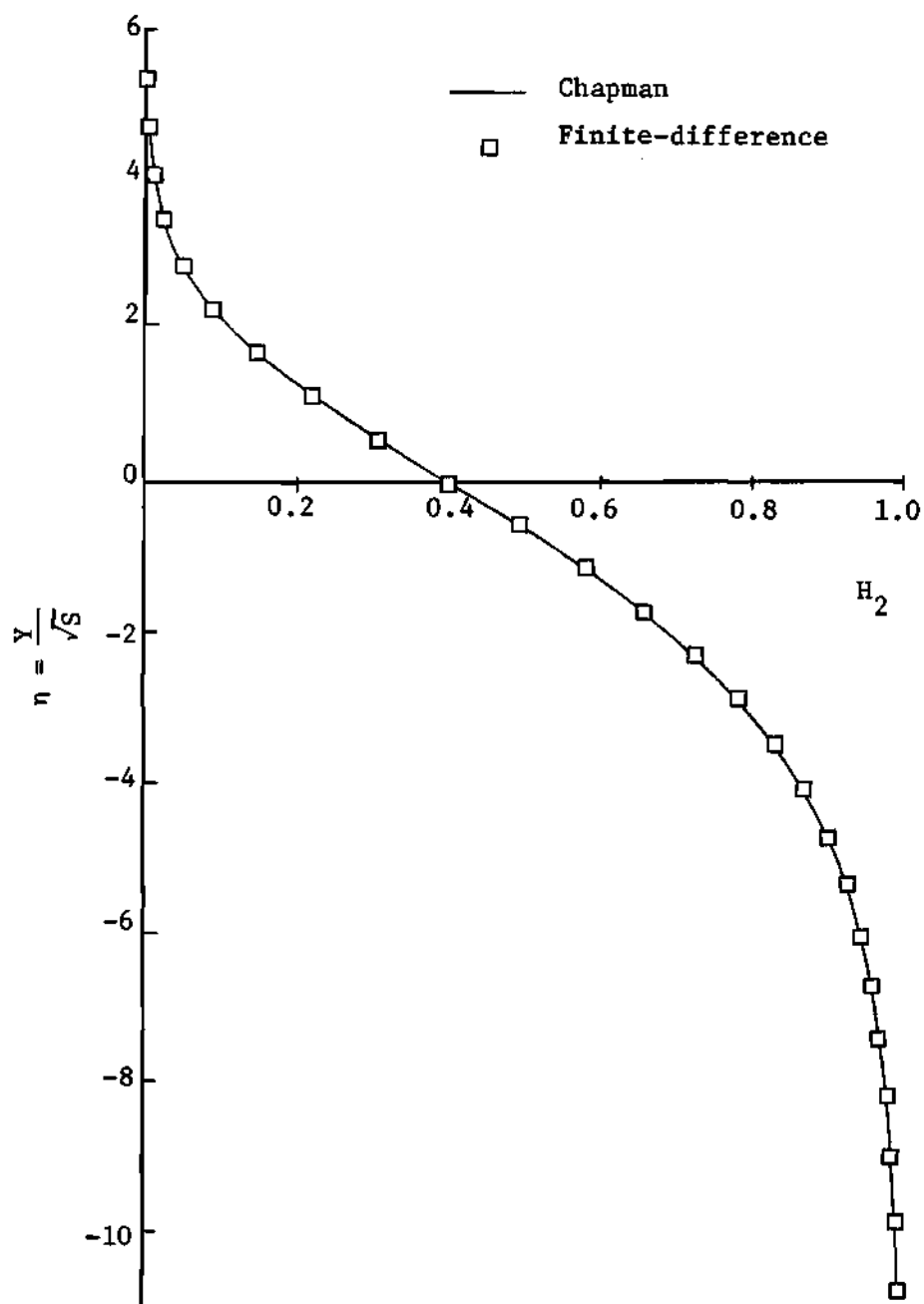


Figure 41. Enthalpy Function Profile H_2 from the Finite-Difference Solution with Chapman Profile Used as Initial Profile, $Pr = 0.72$.

APPENDIX D

INVESTIGATION OF THE EFFECTS OF BLUNTNES ON THE
HEAT TRANSFER RATE

In this appendix the effects of a blunted-cusp reattachment geometry on the heat transfer rate are explored using the blunt body theory of Lees (24). The analysis is based upon the assumption that the portion of the free shear layer profile affected by the blunt leading edge is small enough to allow the use of a uniform flow approaching the reattachment point and that the leading-edge effects downstream of the nose are equivalent to those of a blunt flat plate. The range over which the dividing streamline Mach number may vary is first studied. Then Lees' theory is employed to calculate the heat transfer rate over the cylindrical leading edge of a blunted flat plate for representative values of the dividing streamline Mach number. Finally, the effects of the degree of bluntness is explored.

The Range of Values for the Dividing Streamline Mach Number

Since the Mach number of the approaching flow is required in the blunt body theory, it is necessary to determine the range of Mach numbers of interest for the reattaching free shear layers considered here. For simplicity, a perfect gas with $Pr = 1$ is assumed.

The Mach number ahead of the blunted-cusp geometry is approximated by the dividing streamline Mach number M_d . The range of values

of M_d may be determined in the following manner. From Reynolds analogy, the local stagnation temperature T_o for a constant-pressure free shear layer is related to the local velocity by

$$\frac{T_o - T_w}{T_{oe} - T_w} = \frac{u}{u_e} = u^*$$

The stagnation temperature at the dividing streamline is thus given by

$$\frac{T_{od}}{T_{oe}} = u_d^* \left(1 - \frac{T_w}{T_{oe}} \right) + \frac{T_w}{T_{oe}} \quad (D-1)$$

For a perfect gas, the ratio of the dividing streamline Mach number and the freestream Mach number may be expressed in terms of the velocity ratio and the stagnation temperature ratio yielding

$$\left(\frac{M_d}{M_e} \right)^2 = \frac{u_d^{*2} \frac{T_{oe}}{T_{od}}}{1 + \frac{\gamma-1}{2} M_e^2 \left(1 - u_d^{*2} \frac{T_{oe}}{T_{od}} \right)} \quad (D-2)$$

As is common in hypersonic flow problems, "cold-wall" conditions are assumed, thus

$$\frac{T_w}{T_{oe}} \approx 0$$

Substitution of this relation into equation (D-2) yields the following

expression for M_d :

$$\left(\frac{M_d}{M_e} \right)^2 = \frac{u_d^*}{1 + \frac{\gamma - 1}{2} M_e^2 (1 - u_d^*)} \quad (D-3)$$

The variation of the dividing streamline Mach number with the freestream Mach number as computed from equation (D-3) is presented in Figure 42. Results for $\gamma = 1.3$ and 1.4 are shown. Two values of u_d^* are considered. The case $u_d^* = 0.587$ corresponds to the asymptotic similar free shear layer profile and represents the maximum dividing streamline velocity ratio. The case $u_d^* = 0.3$ corresponds roughly to the lower limit encountered for the multiple-cavity geometries. The limiting values of M_d for $M_e = \infty$ are indicated.

These results demonstrate that the Mach number along the dividing streamline varies only over a restricted range. For a freestream Mach number varying from 5 to ∞ , the value of M_d falls approximately in the range from 1.5 to 3.0. With this in mind, representative values of M_d in this range may be used in the blunt body theory to investigate the effects of bluntness on the heat transfer rate.

Application of Lees' Blunt Body Theory

The blunt body theory of reference (24) is employed to compute the heat transfer rate to the cylindrical leading edge of a blunted flat plate depicted in Figure 43 and compare with the results for an equivalent sharp-edged flat plate. From reference (24), the local heat transfer rate to the surface of a blunt body q_b is given by

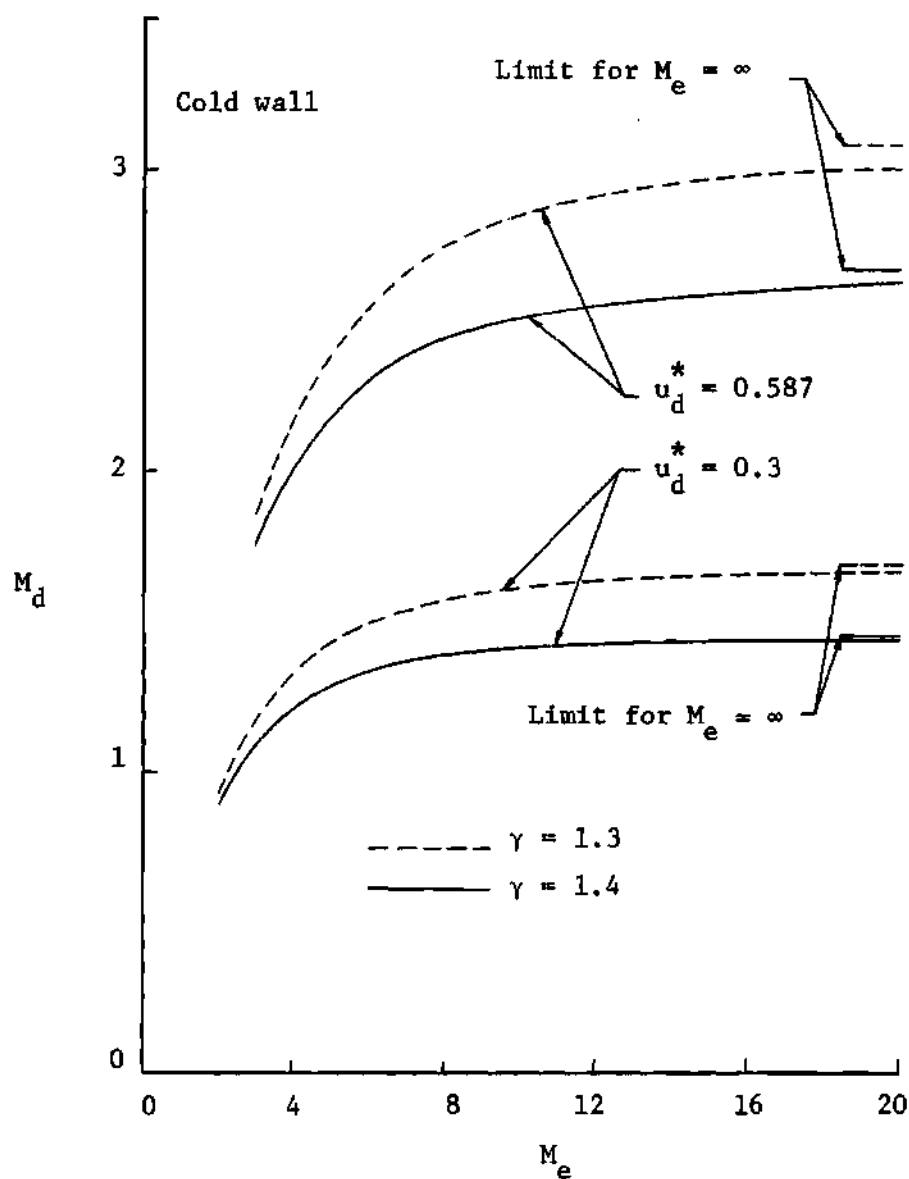


Figure 42. Variation of the Mach Number Along the Dividing Streamline with the Freestream Mach Number ($Pr = 1$).

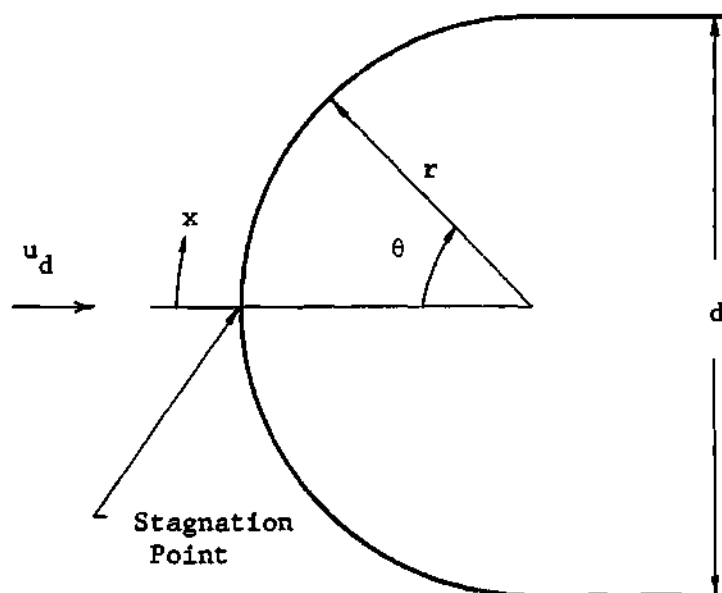


Figure 43. Geometry for the Blunted Leading Edge.

$$q_b = \frac{0.5 \text{ Pr}^{-\frac{2}{3}} \sqrt{\rho_{\delta_o} u_{\delta_o}} \sqrt{u_d} h_{s_\delta} \left(\frac{p}{p_o'} \right) \left(\frac{\omega_\delta}{\omega_{\delta_o}} \right) \left(\frac{u_\delta}{u_d} \right)}{\left[2 \int_0^x \left(\frac{p}{p_o'} \right) \left(\frac{u_\delta}{u_d} \right) \left(\frac{\omega_\delta}{\omega_{\delta_o}} \right) dx \right]^{\frac{1}{2}}} \quad (\text{D-4})$$

where δ indicates the outer edge of the boundary layer, h_s is the total enthalpy, p_o' is the stagnation pressure behind the bow shock wave at the stagnation point, and ω is defined by

$$\omega = \frac{u}{RT}$$

The velocity u_d in equation (D-4) represents the effective uniform velocity forward of the bow shock. Introduction of the Chapman-Rubesin viscosity-temperature relation along with the equation of state for a perfect gas into the definition of ω yields

$$\frac{\omega_\delta}{\omega_{\delta_o}} = C$$

and equation (D-4) becomes

$$q_b = \frac{0.5 \sqrt{\frac{C}{2}} \text{ Pr}^{-\frac{2}{3}} \sqrt{\rho_{\delta_o} u_{\delta_o}} \sqrt{u_d} h_{s_\delta} \left(\frac{p}{p_o'} \right) \left(\frac{u_\delta}{u_d} \right)}{\left[\int_0^x \left(\frac{p}{p_o'} \right) \left(\frac{u_\delta}{u_d} \right) dx \right]^{\frac{1}{2}}} \quad (\text{D-5})$$

For the sharp-edged flat plate, $\frac{u_\delta}{u_d} = 1$ and $\frac{p}{p_o'} = \frac{p_d}{p_o'}$, so that the local heat transfer to the flat plate q_{fp} is given by

$$q_{fp} = \frac{0.5 \sqrt{\frac{C}{2}} \text{Pr}^{-\frac{2}{3}} \sqrt{\rho_{\delta o} u_{\delta o}} \sqrt{u_d} h_{s\delta} \sqrt{\frac{p_d}{p_o}}}{\sqrt{x}} \quad (\text{D-6})$$

Taking the ratio of equation (D-5) and (D-6) leads to the expression

$$\frac{q_b}{q_{fp}} = \frac{\left(\frac{p}{p_o} \right) \left(\frac{u_\delta}{u_d} \right) \sqrt{x}}{\left[\left(\frac{p_d}{p_o} \right) \int_0^x \left(\frac{p}{p_o} \right) \left(\frac{u_\delta}{u_d} \right) dx \right]^{\frac{1}{2}}} \quad (\text{D-7})$$

Using modified Newtonian theory, the pressure distribution is given by

$$\frac{p}{p_o} = 1 - \left(1 - \frac{p_d}{p_o} \right) \sin^2 \theta \quad (\text{D-8})$$

where θ is the angle between the approaching flow and the radius vector from the center of curvature of the nose as shown in Figure 43. From reference (24),

$$\left(\frac{u_\delta}{u_d} \right)^2 = \left[1 + \frac{2}{(\gamma_d - 1) M_d^2} \right] \left[1 - \left(\frac{p}{p_o} \right)^{\frac{\bar{\gamma}-1}{\bar{\gamma}}} \right] \quad (\text{D-9})$$

where $\bar{\gamma}$ is a mean value behind the shock. Substitution of equation (D-9) into equation (D-7) and using $x = r\theta$ yields

$$\frac{q_b}{q_{fp}} = \frac{\sqrt{\theta} \left[1 + \frac{2}{(\gamma_d - 1) M_d^2} \right]^{\frac{1}{2}} \left[\left(\frac{p}{p_o} \right)' \left(1 - \left(\frac{p}{p_o} \right)' \right)^{\frac{\bar{\gamma}-1}{\bar{\gamma}}} \right]^{\frac{1}{2}}}{\sqrt{\frac{p_d}{p_o}}' \left[\int_0^{\theta} \left(\frac{p}{p_o} \right)' \left(1 - \left(\frac{p}{p_o} \right)' \right)^{\frac{\bar{\gamma}-1}{\bar{\gamma}}} d\theta \right]^{\frac{1}{2}}} \quad (D-10)$$

where $\frac{p}{p_o}'$ is given by equation (D-8).

Equation (D-10) was employed to calculate values of $\frac{q_b}{q_{fp}}$ over the interval $0 \leq \theta \leq \frac{\pi}{2}$. Then a mean value

$$\bar{q}_{nose} = \left(\frac{q_b}{q_{fp}} \right)$$

was found by numerical integration over this interval. These calculations were carried out for four cases which were chosen to illustrate the effects of the Mach number of the approaching flow within the range of interest here. The four cases selected and the resulting values of \bar{q}_{nose} are summarized as follows:

Case	$\gamma_d = \bar{\gamma}$	$\frac{p_d}{p_o}'$	M_d	\bar{q}_{nose}
1	1.3	0.1	2.80	1.47
2	1.3	0.2	1.92	1.26
3	1.4	0.1	2.72	1.51
4	1.4	0.2	1.87	1.27

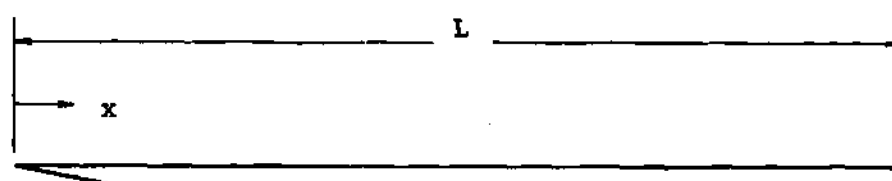
These results demonstrate the effect of blunting on the average heat

transfer rate. The higher values of M_d approximate the upper limit for which the freestream Mach number approaches infinity. The lower values of M_d represent an approximate mean condition for hypersonic free-stream flows. Lower values of M_d were not considered because of the limitations of the modified Newtonian theory. These results show that the average heat transfer rate to the cylindrical leading edge of a flat plate is approximately 50 per cent greater than the average heat transfer rate to a sharp-edge flat plate with the same surface length for high hypersonic freestream Mach numbers. The difference in heat transfer rate decreases with decreasing freestream Mach numbers. At a condition typical of the reattachments considered here, the difference is approximately 25 per cent. With typical values of \bar{q}_{nose} , the effect of the degree of bluntness (i.e., the ratio of leading edge diameter to the length of the plate) on the overall heat transfer rate may be estimated.

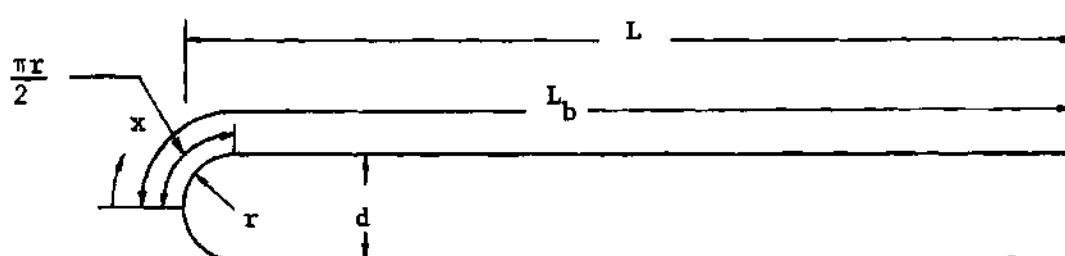
Effect of Degree of Bluntness

Consider the overall heat transfer rate to the three geometries depicted in Figure 44. Figure 44(a) illustrates a sharp-edged flat plate of length L . Figure 44(b) illustrates a flat plate of overall length L with a cylindrical blunt leading edge of radius r . Figure 44(c) illustrates an equivalent sharp-edged flat plate which has the same overall heat transfer rate as the blunted plate of Figure 44(b).

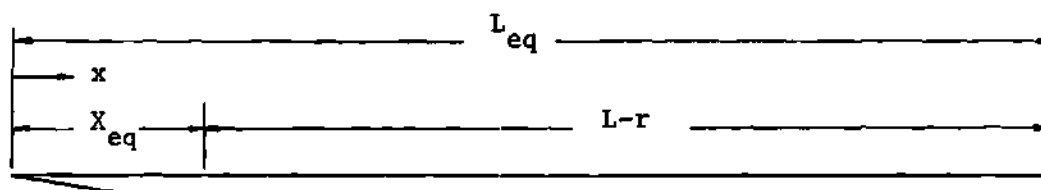
The overall heat transfer rate to the blunted plate Q_b may be expressed as the integrated heat transfer rate over the cylindrical nose (i.e., $0 \leq x \leq \frac{\pi r}{2}$) plus the integrated heat transfer rate over



(a) Sharp-Edge Flat Plate.



(b) Blunted Flat Plate.



(c) Equivalent Sharp-Edged Flat Plate.

Figure 44. Illustration of Geometries Employed to Investigate Effect of Degree of Bluntness on the Overall Heat Transfer Rate.

the remaining portion of the plate ($\frac{\pi r}{2} \leq x \leq L_b$) yielding

$$Q_b = \int_0^{L_b} q_b \, dx = \int_0^{\frac{\pi r}{2}} q_b \, dx + \int_{\frac{\pi r}{2}}^{L_b} q_b \, dx \quad (D-11)$$

For comparison, the overall heat transfer rate to the sharp-edged flat plate Q_{fp} is given by

$$Q_{fp} = \int_0^L q_{fp} \, dx \quad (D-12)$$

Equation (D-11) may be rewritten in terms of q_{fp} in the following manner. From the definition of \bar{q}_{nose} it follows that

$$\int_0^{\frac{\pi r}{2}} q_b \, dx = \bar{q}_{nose} \int_0^{\frac{\pi r}{2}} q_{fp} \, dx \quad (D-13)$$

The second term on the right hand side of equation (D-11) may be evaluated by assuming that the local heat transfer rate to the portion of the blunted plate downstream of the cylindrical nose is given by the value for an equivalent sharp-edged flat plate. As used here, equivalent signifies that the overall heat transfer rate to the portion of the sharp-edged flat plate $0 \leq x \leq X_{eq}$ is equal to the overall heat transfer to the nose of the blunted plate, i.e.,

$$\int_0^{\frac{\pi r}{2}} q_b \, dx = \int_0^{X_{eq}} q_{fp} \, dx \quad (D-14)$$

The second term in equation (D-11) thus becomes

$$\int_{\frac{\pi r}{2}}^{L_b} q_b \, dx = \int_{X_{eq}}^{L_{eq}} q_{fp} \, dx \quad (D-15)$$

Using $L_{eq} = L - r + X_{eq}$, substitution of equations (D-13) and (D-15) into equation (D-11) yields

$$Q_b = \bar{q}_{nose} \int_0^{\frac{\pi r}{2}} q_{fp} \, dx + \int_{X_{eq}}^{L-r+X_{eq}} q_{fp} \, dx$$

Comparison of Q_b and Q_{fp} leads to the expression

$$\frac{Q_b}{Q_{fp}} = \frac{\bar{q}_{nose} \int_0^{\frac{\pi r}{2}} q_{fp} \, dx + \int_{X_{eq}}^{L-r+X_{eq}} q_{fp} \, dx}{\int_0^L q_{fp} \, dx} \quad (D-16)$$

Since the flat plate local heat transfer rate q_{fp} is proportional to $\frac{1}{\sqrt{x}}$, the integrations in equation (D-16) may be carried out to yield

$$\frac{Q_b}{Q_{fp}} = \frac{\bar{q}_{nose} \sqrt{\frac{\pi r}{2}} + \sqrt{L - r + X_{eq}} - \sqrt{X_{eq}}}{\sqrt{L}} \quad (D-17)$$

Equations (D-13) and (D-14) may be combined to give an expression for x_{eq} , i.e.,

$$x_{eq} = \bar{q}_{nose}^{-2} \frac{\pi r}{2}$$

Using this relation in equation (D-17) yields

$$\frac{Q_b}{Q_{fp}} = \left[1 + \frac{1}{2} \left(\frac{\pi}{2} \bar{q}_{nose}^{-2} - 1 \right) \frac{d}{L} \right]^{\frac{1}{2}} \quad (D-18)$$

where the thickness ratio $\frac{d}{L} = \frac{2r}{L}$.

The variation of $\frac{Q_b}{Q_{fp}}$ with the thickness ratio $\frac{d}{L}$ for several values of \bar{q}_{nose} is illustrated in Figure 45. For conditions typical of the reattaching free shear layers of interest here, the blunt body theory yields a value for \bar{q}_{nose} of approximately 1.25. For this condition a blunt flat plate of ten per cent thickness (i.e., $\frac{d}{L} = 0.1$) would experience an increase in overall heat transfer rate of only three per cent. For a freestream Mach number approaching infinity and with a fully-developed free shear layer profile at reattachment, this increase in heat transfer rate would reach a maximum of about six per cent for $\frac{d}{L} = 0.1$.

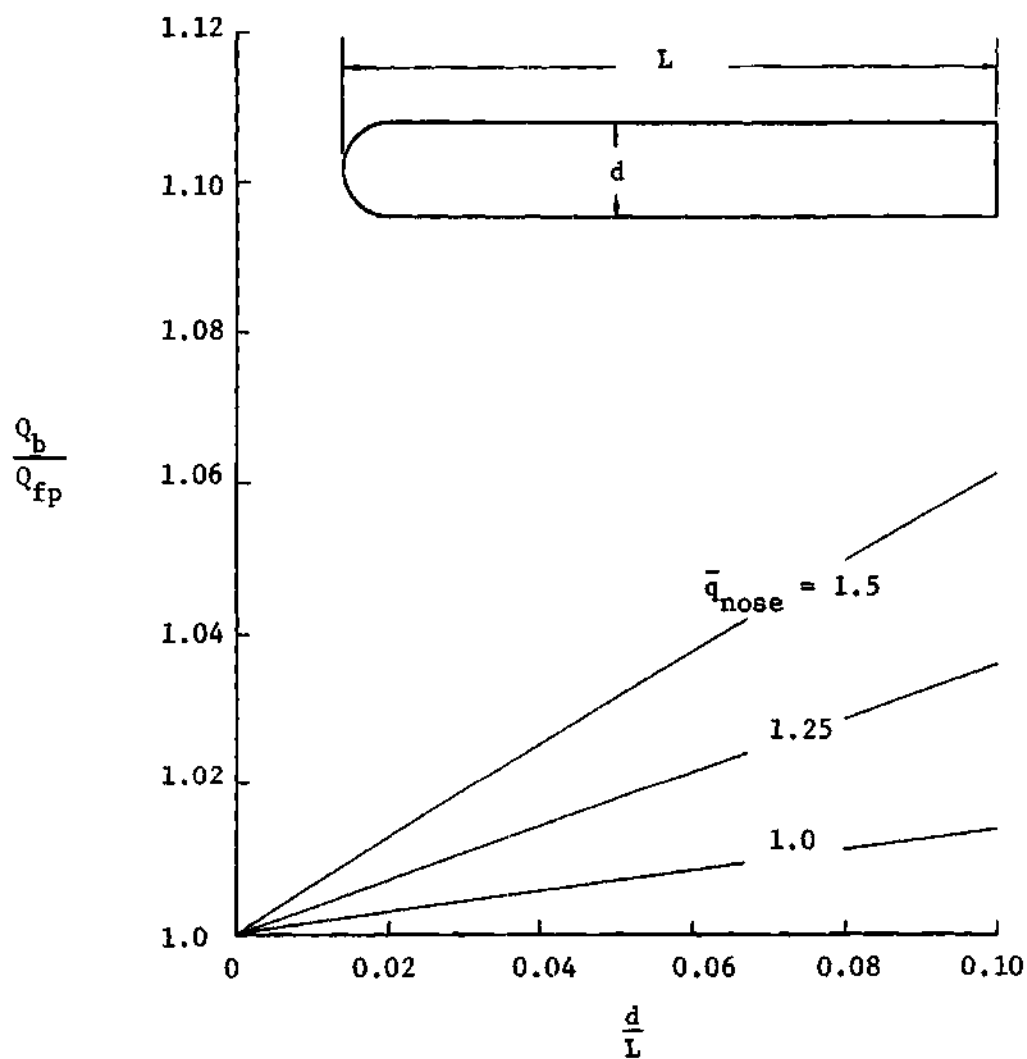


Figure 45. Effect of Thickness Ratio $\frac{d}{L}$ on the Heat Transfer Rate for Several Values of \bar{q}_{nose} .

LITERATURE CITED

1. L. G. Kaufman, S. A. Hartofilis, W. J. Evans, R. A. Oman, L. H. Meckler, and D. Weiss, "A Review of Hypersonic Flow Separation and Control Characteristics," Aeronautical Systems Division TDR 62-168, 1962.
2. J. F. Nash, "A Review of Research on Two-Dimensional Base Flow," Aeronautical Research Council R and M 3323, 1962.
3. P. S. Lykoudis, "A Review of Hypersonic Wake Studies," AIAA Journal, 4, pp. 577-590, 1966.
4. D. R. Chapman, D. M. Kuehn, and H. K. Larson, "Preliminary Report on a Study of Separated Flows in Supersonic and Subsonic Streams," NACA RM A55L14, 1956.
5. D. R. Chapman, "A Theoretical Analysis of Heat Transfer in Regions of Separated Flow," NACA TN 3792, 1956.
6. M. R. Denison and E. Baum, "Compressible Free Shear Layer with Finite Initial Thickness," AIAA Journal, 1, pp. 342-349, 1963.
7. H. K. Larson, "Heat Transfer in Separated Flows," Journal of the Aerospace Sciences, 26, pp. 731-738, 1959.
8. S. M. Bogdanoff and I. E. Vas, "Some Experiments on Hypersonic Separated Flows," ARS Journal, 32, pp. 1564-1572, 1962.
9. K. M. Nicoll, "A Study of Laminar Hypersonic Cavity Flows," AIAA Journal, 2, pp. 1535-1541, 1964.
10. P. M. Chung and J. R. Viegas, "Heat Transfer at the Reattachment Zone of Separated Laminar Boundary Layers," NASA TN D-1072, 1961.
11. M. S. Holden, "Experimental Studies of Separated Flows at Hypersonic Speeds. Part II: Two-Dimensional Wedge Separated Flow Studies," AIAA Journal, 4, pp. 790-799, 1966.
12. R. F. Kramer and H. M. Lieberstein, "Numerical Solution of Boundary Layer Equations Without Similarity Assumptions," Journal of the Aerospace Sciences, 26, pp. 508-514, 1959.
13. E. R. G. Eckert, "Engineering Relations for Friction and Heat Transfer to Surfaces in High Velocity Flow," Journal of the Aeronautical Sciences, 22, pp. 585-587, 1955.

14. G. E. Forsythe and W. R. Wasow, Finite Difference Methods for Partial Differential Equations, John Wiley and Sons, New York, 1960.
15. R. D. Richtmeyer, Difference Methods for Initial-Value Problems, Interscience Publishers, New York, 1957.
16. I. Flugge-Lotz and D. C. Baxter, "The Solution of Compressible Laminar Boundary Layer Problems by a Finite Difference Method, Part I and Part II," Stanford University Technical Report 103 and 110, 1956 and 1957.
17. J. C. Wu, "On the Finite Difference Solution of Laminar Boundary Layer Problems," Proceedings of the Heat Transfer and Fluid Mechanics Institute, pp. 55-69, 1961.
18. I. Flugge-Lotz and F. G. Blottner, "Computation of the Compressible Laminar Boundary-Layer Flow Including Displacement-Thickness Interaction Using Finite-Difference Methods," Stanford Univ., Div., Eng. Mech., TR 131, 1962.
19. A. M. O. Smith and D. W. Clutter, "Machine Calculation of Compressible Laminar Boundary Layers," AIAA Journal, 3, pp. 639-647, 1965.
20. G. Kleinstein, "A Finite Difference Solution for an Initial Value Problem in a Compressible Laminar Boundary Layer," Aerospace Research Laboratories, ARL 65-107, 1965.
21. G. G. O'Brien, M. A. Hyman, and S. Kaplan, "A Study of the Numerical Solution of Partial Differential Equations," Journal of Math. and Phys., 29, pp. 223-251, 1951.
22. C. F. Dewey, S. I. Schlesinger, and L. Sashkin, "Temperature Profiles in a Finite Solid with Moving Boundary," Journal of the Aerospace Sciences, 27, pp. 59-64, 1960.
23. F. B. Hildebrand, Methods of Applied Mathematics, Prentice-Hall, 1952.
24. L. Lees, "Laminar Heat Transfer Over Blunt-Nosed Bodies at Hypersonic Flight Speeds," Jet Propulsion, 26, pp. 259-269, 1956.
25. E. R. Van Driest, "Investigation of Laminar Boundary Layer in Compressible Fluids Using the Crocco Method," NACA TN 2597, 1952.

VITA

Jerry Allen Sills was born in Atlanta, Georgia on September 6, 1940. He attended the elementary and secondary schools of that city and was graduated from Murphy High School in June, 1958.

In September of 1958 he entered the Georgia Institute of Technology and was awarded the degree of Bachelor of Aeronautical Engineering in June of 1963. He continued his education at the Georgia Institute of Technology as a graduate student and received a NASA traineeship to study under the doctoral program. The degree of Master of Science in Aerospace Engineering was awarded in June of 1965. He is a member of the Phi Eta Sigma, Sigma Gamma Tau, and Sigma Xi honorary societies.

On December 19, 1964 he was married to the former Miss Sandra Jean Moon.